Using Core-Shell Nanocatalysts to Unravel the Impact of Surface Structure on Catalytic Activity:

Author: Benjamin Parker Williams

Persistent link: http://hdl.handle.net/2345/bc-ir:108918

This work is posted on eScholarship@BC,
Boston College University Libraries.

Using Core-Shell Nanocatalysts to Unravel the Impact of Surface Structure on Catalytic Activity

Benjamin Parker Williams

A dissertation

submitted to the Faculty

of the Department of Chemistry

in partial fulfillment

of the requirements for the degree of

Doctor of Philosophy

Boston College
Morrissey College of Arts and Sciences
Graduate School

August 2020

For Mom

USING CORE-SHELL NANOCATALYSTS TO UNRAVEL THE IMPACT OF SURFACE STRUCTURE ON CATALYTIC ACTIVITY

Benjamin P. Williams

Advisor: Prof. Chia-Kuang (Frank) Tsung, Ph.D.

ABSTRACT

The high surface area and atomic-level tunability offered by nanoparticles has defined their promise as heterogeneous catalysts. While initial studies began with nanoparticles of a single metal assuming thermodynamic shapes, modern work has focused on using nanoparticle composition and geometry to optimize nanocatalysts for a wide variety of reactions. Further optimization of these refined nanocatalysts remains difficult, however, as the factors that determine catalytic activity are intertwined and a fundamental understanding of each remains elusive. In this work, precise synthetic methods are used to tune a number of factors, including composition, strain, metal-to-metal charge transfer, atomic order, and surface faceting, and understand their impact on catalysis. The first chapter focuses on current achievements and challenges in the synthesis of intermetallic nanocatalysts, which offer long-range order that allows for total control of surface structure. A particular focus is given to the impact of the synthetic approach on the activity of the resulting nanoparticles. In the second chapter, multilayered Pd-(Ni-Pt)$_x$ nanoparticles serve as a controlled arena for the study of metallic mixing and order formation on the nanoscale. The third chapter controls the shell thickness of Au@PdPt core-alloyed shell nanoparticles on a nanometer scale to isolate strain at the nanoparticle surface. In the fourth chapter, the synthetic approaches of chapters two and three are applied to catalysis. In totality, the work presented here represents a brick in the foundation of understanding and exploiting structure-function relationships on the nanoscale, with an eye toward the rational design of tailored nanocatalysts.

ACKNOWLEDGMENTS

Thank you first to my advisor, Frank Tsung. The choice of an advisor is the most crucial of your graduate studies, and I could not have asked for a better teacher, boss, and mentor. Thank you to my committee, Matthias Waegele, Dunwei Wang, and Udayan Mohanty. The Boston College physical chemistry department is truly a joy to be a part of, and I am thankful that I was lucky enough to spend so much time learning and breaking bread with each of you. Thank you to Allison Young, my mentor for my first several years in the Tsung group, who was and remains a fountain of knowledge about life, both scientific and nonscientific. Thank you to Joe Morabito, who was a role-model for everything I aspired to be as a senior graduate student. Thank you to Wei-Shang Lo, a genuine friend and extraordinarily hardworking scientist who will be writing a dissertation sooner than he thinks. Thank you to Tom Rayder, who was with me every step of the way during our PhD studies. Thank you to Adam Bensalah, a joy to sit next to in the Tsung lab. Thank you to Ken Metz, who showed me the delightful nuance in Analytical Chemistry and provides a shining example of a dedicated professor who loves the craft of teaching. Thank you to Dave McFadden for showing me that even the most senior professor can become a mentor and friend. Thank you to the Boston College Chemistry staff, especially Lynne, Dale, and Ian, who created a welcoming, collaborative environment and work tirelessly (and with too little thanks) to maintain the well-oiled chemistry machine. Thank you to our collaborators, Jim Evans, Wenyu Huang, and their respective research groups, who provided theoretical guidance and experimental results that are fundamental to this dissertation. Thank you to Boston College and the National Science Foundation for funding my research.

Thank you to Joe DuChene, my undergraduate mentor and current friend, who convinced me that PhD studies might be a worthwhile and enjoyable pursuit and who continues to offer sage advice. Thank you to Jesse and Jacob, wonderful scientists and better friends. Thank you to Dillon,

with whom I spent the worst parts of graduate school and came through to the other side, and to Jordan, with apologies for the absence of your space jar. Thank you to Kat, Megan, Seti, John, Jenny, Kristina, and the rest of the Loretta's Line Dancing crew, who entered my life at the perfect time and are the epitome of genuine and caring friendship. Thank you to Sandro, who saved my life. To anyone, graduate student or otherwise, who finds themselves in the midst of a seemingly endless struggle: therapy is not giving up but starting again. Thank you to Dr. Coffey, who, with just a few words, can set your life on the right path and who continues to provide an example of a loving and god-fearing life. Thank you to my mom, who has sacrificed so much to raise her three boys and without whom this dissertation would not exist. Thank you to my dad, who showed a child what intellectual curiosity and academic rigor could achieve. Thank you to my brothers, who are flourishing in their niche and remain avid and loving listeners and friends.

Thank you, lastly, to Elizabeth. Though I have given it literally years of thought, I cannot put into words the way that she is woven into these pages. The love of my life, for many years to now and many years to come.

TABLE OF CONTENTS

LIST OF FIGURES

LIST OF TABLES

Chapter 1

The Synthesis of Intermetallic Nanoparticles

1.1 Abstract

Intermetallic alloy nanocrystals have emerged as a promising next generation of nanocatalyst, largely due to their promise of surface tunability. Atomic control of the geometric and electronic structure of the nanoparticle surface offers precise command of the catalytic surface, with potential for creating a homogeneous active site that extends over the entire nanoparticle. Realizing this promise, however, has been limited by synthetic difficulties, imparted by differences in parent metal crystal structure, reduction potential, and atomic size. Further, little attention has been paid to the impact of synthetic method on catalytic application. In this chapter, we seek to connect the two, highlighting the current catalytic scope of intermetallic syntheses and suggesting areas where more work is needed. Such analysis should help to guide future intermetallic nanoparticle development, with the ultimate goal of generating precisely controlled nanocatalysts tailored to any reaction. Insights presented herein will also be used to complement and extend the analysis of our own work, presented in detail in Chapters 2 and 3.

1.2 Introduction

With increased attention paid to global warming, interest in renewable energy is rapidly increasing.[1] Though platinum remains at the forefront of industry, alternatives are gaining traction, particularly through the addition of nonprecious metals that can simultaneously reduce cost and increase scope.[2-5] Work on the nanoscale began with random alloys that offered the ability to mimic (or improve upon) the overall electronic structure of platinum.[6-8] However, though altering composition allowed platinum content to be decreased and the over electronic structure to be changed, these random alloys do not allow for fine control over nanoparticle (NP) surface structure.

Intermetallic compounds (IMCs), with long-range order throughout the alloyed crystal lattice, offer a solution to this challenge, with the potential to position individual atoms for complete geometric and electronic control.[9-11] They have already found use in many fields, including shape memory,[12-14] hydrogen storage,[15-17] and superconductivity.[18-21] Their application in catalysis is growing, as they have been shown to be generally more robust and often more active than their random alloyed counterparts.[22-25]

However, even though IMCs are thermodynamically stable, their synthesis usually requires high temperature mixing that prevents easy fabrication on the nanoscale, especially with a controlled morphology.[26-28] Many of the most active nanocatalysts have far-from-equilibrium structures and controlled sizes[5, 29-31] that can be damaged by even relatively mild annealing conditions. As such, fine synthetic control initially focused on random-alloy nanoparticles.[32-43] Recently, though, a number of synthetic approaches have been identified for the successful fabrication of IMC NPs. The array of approaches has been outlined elsewhere, but, in general, discussion of the synthetic method has been decoupled from the catalytic application.[44-52] We believe that discussing the two simultaneously could be beneficial for two reasons: First, it could be more clearly identified which synthetic approaches are being applied to which reactions, allowing for the recognition of reactions lacking IMC catalysts. Second, synthesis method can have a lasting impact on catalysis. By grouping synthetic methods with catalytic applications, we seek to shed light on the current strengths and weaknesses of IMC NP catalysis. The insight generated should guide the development of new IMC catalysts, with a vision for the generation of design rules for the synthesis and application of catalysts tailorable to any given reaction.

1.3 Top-Down Methods

Top-down approaches are roughly defined as methods that either perform bulk IMC formation or focus on transferring the harsh annealing conditions associated with IMC formation to the nanoscale. When applied directly to NP synthesis, there is generally some form of protection for the nanoparticles, e.g. an oxide support, that prevents sintering and allows the nanostructures to survive under relatively high temperatures. Top-down methods benefit from their relative ease of synthesis, and it is well-known that supports can play a valuable role in catalysis.[53-55] However, fine control over the NP surface structure is somewhat lacking, which saps some of the benefits of using IMC NPs.

1.3.1 Bulk Annealing

Perhaps the most straightforward method to transfer the historical methods of IMC formation[56] to the nanoscale is to simply use the harsh annealing conditions required to mix metals in the bulk and then modify the resulting IMCs to form nanocatalysts. Schlogl, Armbruster, and coworkers prepared Pd-Ga IMCs with various stoichiometries, which they ground into powders and used for the semihydrogenation of acetylene.[57-60] They attribute its high activity to the controlled coordination of Pd in the Pd_xGa_y crystal lattice, showcasing the atomic-level control of IMCs on surface structure.[61] Armbruster showed that ordering in $Cu_{60}Pd_{40}$ powders could improve selectivity, which was attributed to the partial isolation of Pd sites in the ordered structure,[62] and Armbruster, Grin, and coworkers found that the inclusion of Sn into the ordered crystal structure could further increase its activity.[63]
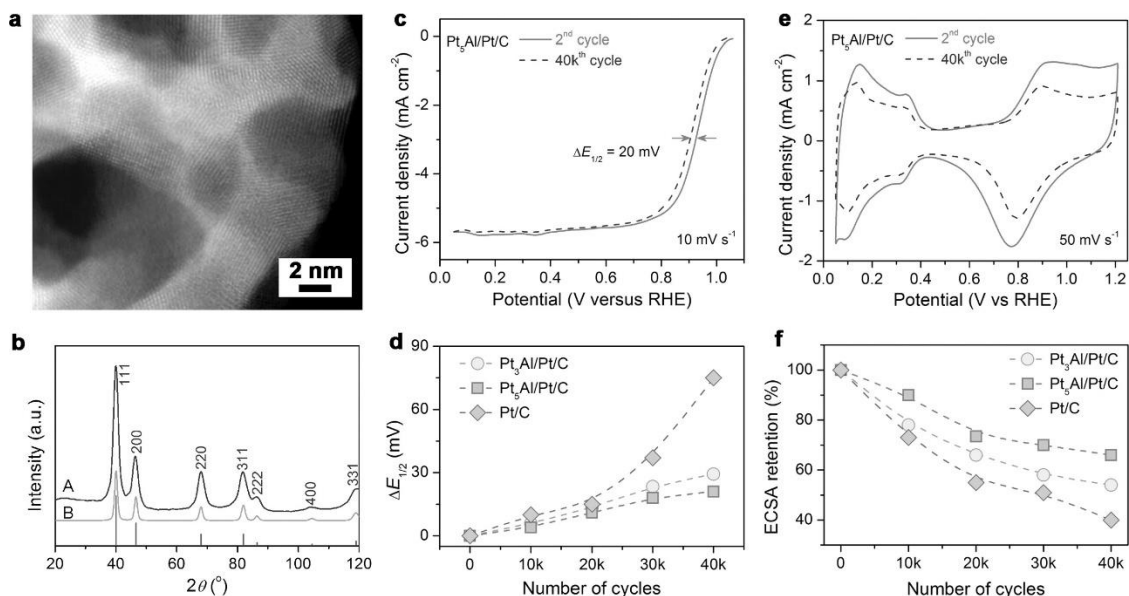
Figure 1.1 Scanning transmission electron microscopy (STEM) image and electrochemical stability of mesoporous $Pt_5Al/Pt/C$ ribbons. (a) High-angle annular dark-field-STEM (HAADF-STEM) image of Pt_5Al/Pt dealloyed intermetallic compound. (b) (A) Measured and (B) simulated x-ray diffraction patterns of MP Pt_5Al/Pt. (c) Polarization curves for the ORR of $Pt_5Al/Pt/C$ catalyst before and after 40,000 potential cycles. (d) Half-wave potentials for $Pt_3Al/Pt/C$, $Pt_5Al/Pt/C$ and Pt/C catalysts as a function of number of cycles. (e) CV curves before and after 40000 potential cycles in a range from 0.6 to 1.1 V. f) Comparison of ECSA retentions for $Pt_3Al/Pt/C$, $Pt_5Al/Pt/C$ and Pt/C catalysts during the electrochemical cycling. Reprinted with permission from Ref. 64.

Jiang and coworkers showed that synthesizing materials through bulk annealing could provide a platform for post-synthetic processing to form active IMC nanocatalysts. They used arc melting and chemical dealloying to produce Pt-Al IMC nanoribbons with Pt_5Al proving particularly active and durable for the oxygen reduction reaction (ORR) (Figure 1.1).[64] They

extended this method to yield Pt-based IMCs for ORR[65-67] and hydrogen evolution (HER)[68] and to synthesize electroactive Al_7Cu_4Ni@Cu_4Ni nanocrystals integrated into a highly conductive Cu skeleton that showed high activity for alkaline HER.[69]

Composition	Catalytic Reaction	Ref	Year
Pd_xGa_y	Selective Hydrogenation	57-61	2008-10
$Cu_{60}Pd_{40}$	Selective Hydrogenation	62	2013
$Ga_{0.72}Sn_{0.28}Pd_2$	Selective Hydrogenation	63	2018
Pt_5Al	ORR	64	2015
$(Pt_{1-x}Fe_x)_3Al$	ORR	65	2016
$(Pt_{1-x}Ni_x)_3Al$	ORR	66	2016
$(Pt_{1-x}Co_x)_3Al$	ORR	67	2018
$(Pt_{1-x}Co_x)_3Al/Pt$-$Co(OH)_2$	HER	68	2019
Al_7Cu_4Ni@Cu_4Ni	HER	69	2018

Table 1.1 IMC Nanocatalysts synthesized through bulk annealing.

Bulk annealing methods offer several advantages. First, their implementation is relatively straight forward, relying on the thermodynamic driving forces that have underpinned metallic mixing for centuries. Second, IMC NPs are somewhat suited to rough preparation methods, like bulk annealing, as the atomic order present in the IMC phase allows even such rough approaches to generate some control over surface structure. That being said, this strategy does not allow for the controlled, far-from equilibrium surface structures that have defined the most active catalysts in single metal and random alloy NPs. Bulk annealing, though, could offer an opportunity to

explore rich new compositions, which may be active without the fine synthetic control of more nuanced methods. Phases identified as active in bulk methods can serve as worthy targets for other shape- and size-controlled methods.

1.3.2 Annealing on a Support

Supports can anchor NPs and prevent sintering and degradation at high annealing temperatures. These properties allow supported NPs to serve as excellent precursors to IMC NPs. Supported NPs also serve an ideal arena to study metallic mixing and IMC phase formation, offering a foundation for the fabrication of supported IMC nanocatalysts.[70-75]

Schaak and coworkers used supported Pt NPs as a template for the reduction of a second metal salt in ethylene glycol, followed by annealing to form IMC PtM (M = Ru, Pb, Sn) NPs supported on CeO_2, Al_2O_3, carbon, and Fe_3O_4.[76] They found that PtPb NPs on Vulcan carbon were active for formic acid oxidation (FOR). Nazar and coworkers used an impregnation method to synthesize Pt-based IMC NPs supported on mesoporous carbon, with PtBi showing high activity for the FOR.[77] Sun and coworkers synthesized ternary CoPtAu NPs with an IMC PtCo core and an alloy PtAu shell that showed excellent catalytic performance for the oxidation of ethanol (EOR), methanol (MOR), and formic acid.[78]
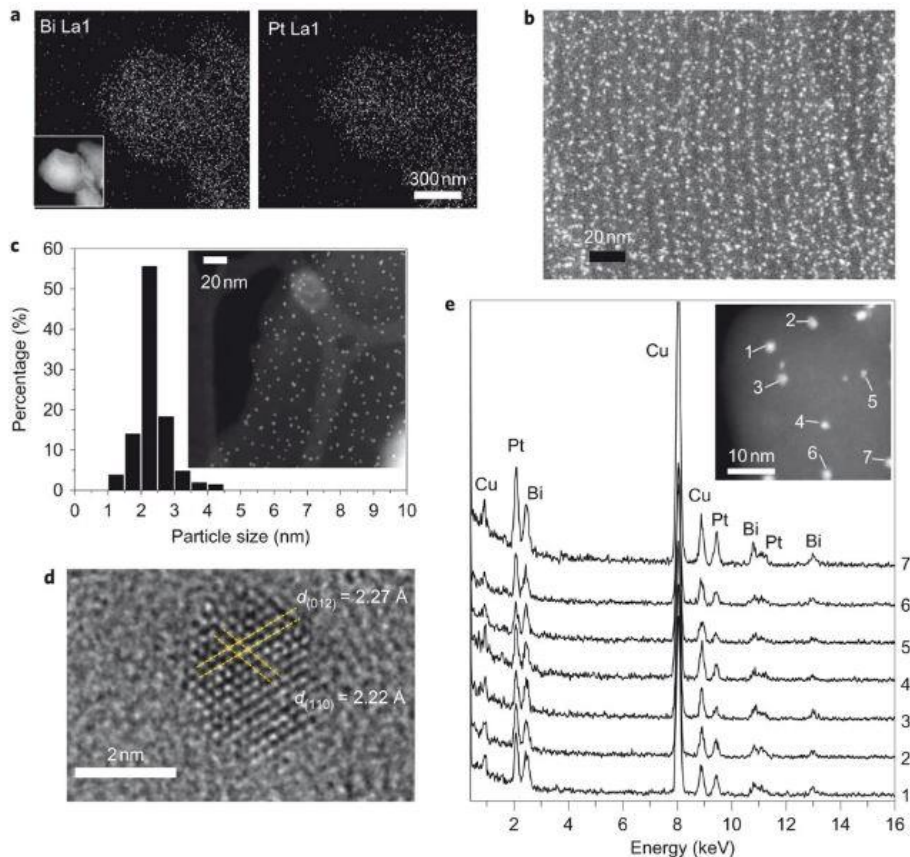
Figure 1.2 Characterization of PtBi IMC NPs. (a) Pt and Bi EDX maps corresponding to their dark-field STEM image (inset), showing sub-nanometer mixing in mesoporous carbon. (b) Dark-field STEM image of ordered mesoporous carbon (OMC)-PtBi-3 nm, illustrating the narrow crystallite size distribution in a representative section of the bulk. (c) Histogram showing nanocrystallite size distribution based on a count of 407 crystallites in two different sample areas (representative STEM image shown in the inset). (d) Bright-field HRTEM image of OMC-PtBi-3 nm, with lattice spacings marked. (e) EDX spectra for individual PtBi nanoparticles in OMC-PtBi-3 nm; the inset shows the dark-field STEM image, with the corresponding analyzed nanoparticles labelled. Reprinted with permission from Ref. 77.

Schaak and coworkers also used the aforementioned method to synthesize Pt_3Sn on graphite for CO oxidation.[76] Komatsu and coworkers synthesized several Pt-based IMC NPs through the successive impregnation and annealing of various metal precursors in mesoporous SiO_2 or Al_2O_3, with Pt_3Co/SiO_2 and $PtCu/Al_2O_3$ highly active for the preferential oxidation of CO in the presence of excess hydrogen (PROX).[24, 79] Komatsu, Furukawa, and coworkers synthesized supported Pt- and Pd-based IMC NPs through impregnation of a SiO_2 or Al_2O_3 support using H_2 or $LiBH_4$ reduction, with Pd_3Bi, Pd_3Pb, and $Pd_{13}Pb_9$ showing particularly high activity for the oxidation of dibenzylamine to *N*-benzylidenebenzylamine, which they attributed to changes in adsorption energies induced by the Pd coordination environment.[80-82]

Yu and coworkers used an anodic aluminum oxide template for electrochemical reduction of $PtCl_2$, CuBr, and $NaNO_3$ in DMSO to form alloy PtCu nanotubes.[83] Still in the support, they were annealed at various temperatures under reducing temperatures (from 300 °C to 700°C) to yield different degrees of ordering and surface Pt content that led to increased activity for the ORR. Abruña and coworkers synthesized $PtCu_3$ IMC NPs through the impregnation of a carbon support and annealing at 1000 °C under H_2.[84] Both electrochemical and chemical dealloying methods were used to activate the NPs for catalysis, with the chemically dealloyed NPs showing high activity and durability for ORR. Abruña and coworkers further synthesized $Pt_3Co@Pt/C$ NPs through an impregnation method, drying Pt and Co precursors into a powder and then annealing at 400 and 700 °C under an H_2 atmosphere.[25] They found that activity and durability for the ORR were dependent on annealing temperature, with the 700 °C showing improved activity and recyclability, which they attribute to the development of an outer Pt shell around the Pt_3Co core. Bock, Botton, and coworkers synthesized an ordered PtFe nanocatalyst by drying $Fe(NO_3)_3$ on Pt/C and annealing at 800 °C under 8% H_2 in Ar.[85] Different crystal structures and degrees of ordering were

seen depending on the initial Fe concentration, with a Pt-rich shell and IMC core contributing to high ORR activity.[86] Yang and coworkers synthesized Pt_3Cr NPs supported on carbon that underwent a disorder-to-order transition under 700 °C annealing.[87] Mass activity for ORR decreased in the order of disordered-Pt_3Cr/C > ordered-Pt_3Cr/C > Pt/C while specific activity and durability increased as Pt/C < disordered-Pt_3Cr/C < ordered-Pt_3Cr/C.

Composition	Catalytic Reaction	Ref	Year
PtPb/C	FOR	76	2008
PtBi/C	FOR	77	2010
CoPtAu/C	MOR, EOR, FOR	78	2019
Pt_3Sn/C	CO Oxidation	76	2008
Pt_3Co/SiO_2	PROX	24	2008
PtCu/Al_2O_3	PROX	79	2013
Pd_3Pb/MO_x	Amine Oxidation	80-82	2013-15
PtCu/AAO	ORR	83	2012
$PtCu_3$/C	ORR	84	2012
Pt_3Co@Pt/C	ORR	25	2013
PtFe/C	ORR	85, 86	2013
Pt_3Cr/C	ORR	87	2014
$AuCu_3$/C	ORR	88	2014
PtFe/C	ORR	89	2015
PtNi/C	ORR	90	2015
PtNi/SiO_2	ORR	91	2016

PtNi$_{0.8}$Co$_{0.2}$/C	ORR	92	2019
Pd$_2$Ga/C	Selective Hydrogenation	93	2011
Rh$_2$Sb/SiO$_2$	Selective Hydrogenation	94	2014
PdZn/SiO$_2$	Selective Hydrogenation	95	2019
Pd$_2$Ga/C	CO$_2$RR	96	2015
Cu$_3$Sn, Cu$_6$Sn$_5$/Cu	CO$_2$RR	97	2019

Table 1.2 IMC Nanocatalysts synthesized through annealing on a support.

Li and coworkers synthesized AuCu$_3$ NPs supported on carbon by reducing CuCl$_2$ and HAuCl$_4$ with NaBH$_4$ onto activated carbon and annealing under 5% H$_2$ gas.[88] The AuCu$_3$/C catalyst showed higher activity and durability for the ORR when compared to Au/C, AuCu/C, and Pt/C, which they attributed to a combination of synergistic effects at the active site that originated from the pairing of two elements with a weak (Au) and strong (Cu) affinity for oxygen binding. Hyeon, Sung, and coworkers synthesized PtFe IMC NPs supported on carbon by annealing random alloy PtFe NPs synthesized by the reduction of Pt(acac)$_2$ in oleic acid and oleyl amine followed by the injection of Fe(CO)$_5$.[89] The ordered fct-PtFe/C showed higher activity and stability for the ORR relative to disordered fcc-PtFe/C and Pt. Yang and coworkers synthesized IMC PtNi NPs through reduction on carbon and a disorder-to-order transition induced by annealing at 550 °C, with the ordered catalysts showing higher mass activity, specific activity, and durability for the ORR than their disordered counterparts.[90] Joo, Yim, and coworkers synthesized mesostructured IMC PtM (M = Ni, Fe, Co, or Cu) nanoparticles through the impregnation of spherical mesoporous silica nanoparticles and reduction by annealing under hydrogen, with PtNi, after multiple annealing steps to induce ordered phase formation, showing high ORR activity and durability over

11

50,000 cycles.[91] Li and coworkers synthesized Pt@NiCoO$_x$ core@shell nanoparticles through a glucose reduction in the presence of PVP, loaded them on carbon black, and annealed them at 600 °C to form L1$_0$-PtNi$_{0.8}$Co$_{0.2}$ IMC NPs.[92] The oxide shell helped to further shield the structure during annealing, and the particles showed high activity and stability for the ORR.
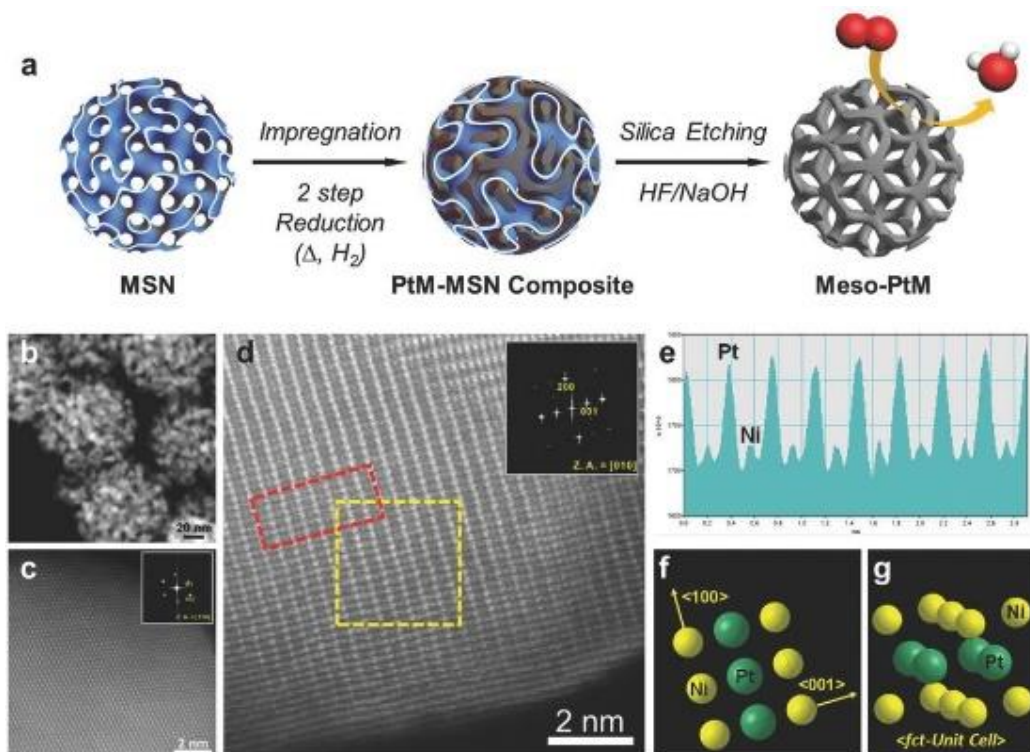
Figure 1.3 Synthesis and characterization of mesostructured Pt-based intermetallic nanospheres (Meso-PtM). (a) Schematic illustration of the synthesis of Meso-PtM. (b) HAADF-TEM image of Meso-PtNi. (c) HAADF-STEM image of Meso-PtNi. (d) Atomic-resolution ADF-STEM image of Meso-PtNi and FFT pattern of yellow square area. (e) Line profile of red rectangular area in figure (d). (f) Projected unit cell of the marked area, along the [010] axis. Reprinted with permission from Ref. 91.

Su and coworkers synthesized Pd_2Ga/C through the impregnation of carbon nanotubes followed by reduction under H_2 gas. The heterostructures showed high activity and selectivity for the semihydrogenation of acetylene.[93] Komatsu and coworkers synthesized Rh-based IMC NPs through the successive impregnation and annealing of various metal precursors in mesoporous oxides, with Rh_2Sb/SiO_2 showing particularly high activity and selectivity for the semihydrogenation and subsequent isomerization of diphenylacetylene to *trans*-stilbene.[94] Komatsu and coworkers synthesized Pd-based IMC NPs on SiO_2 through reduction under flowing H_2 at 1073 K, applying them to the selective hydrogenation of phenylacetylene to form styrene. They found that PdZn IMC NPs were particularly active, and that this activity could be further enhanced by introducing a third metal through galvanic replacement, with PdZn + 0.25Pb performing the best.[95]

Fiordaliso and coworkers synthesized Pd_2Ga IMC NPs through wetness impregnation of SiO_2, which proved active for the hydrogenation of CO_2 to methanol.[96] Chen, Kang, and coworkers electrodeposited Sn on a Cu foam and used annealing to form IMC Cu_3Sn and Cu_6Sn_5 NPs, which were active for the electrochemical reduction of CO_2 to formate.[97]

The annealing of random alloy NPs on a support is perhaps the most natural method for the synthesis of IMC NPs, as the support offers a straightforward way to increase the resilience of NPs to annealing and can supply synergistic effects to increase activity. Carbon is a natural conductive choice for electrochemistry, and oxides are well-studied platforms for controlled syntheses. This approach has thus yielded a rich array of IMC nanocatalysts. However, while these materials are natural targets, future work should be done to explore materials that fall outside of these Pt-based, C/oxide-supported NPs applied to the ORR. One great promise of IMC NPs lies in the atomic-level control of their surface structure, with the hope of tailoring composition and

geometry for specific reactions, displayed in a few works that have pushed composition in new directions and to new reactions.[80-82, 93-94, 96-97] More such studies are needed to expand the scope and fulfill the potential of IMC nanocatalysts.

1.3.3 Annealing in an Inorganic Shell

More recently, this approach has been modified to yield even greater control over the annealing environment by completely encapsulating the nanoparticles in an inorganic shell. Building on initial work in magnetic PtFe IMC NPs,[98-99] Sun and coworkers synthesized IMC fct PtFe NPs through a multistep reduction process involving the use of MgO as an oxide shell for the formation of fct IMC PtFe during annealing.[100] For catalysis, the oxide shell was etched away and the IMC NPs were supported on carbon, displaying high activity and stability for HER and ORR.[101] They additionally found that the use of a second annealing step to form a thin Pt shell in a core@shell PtFe@Pt structure could further enhance activity and prevent Fe leaching.[102]
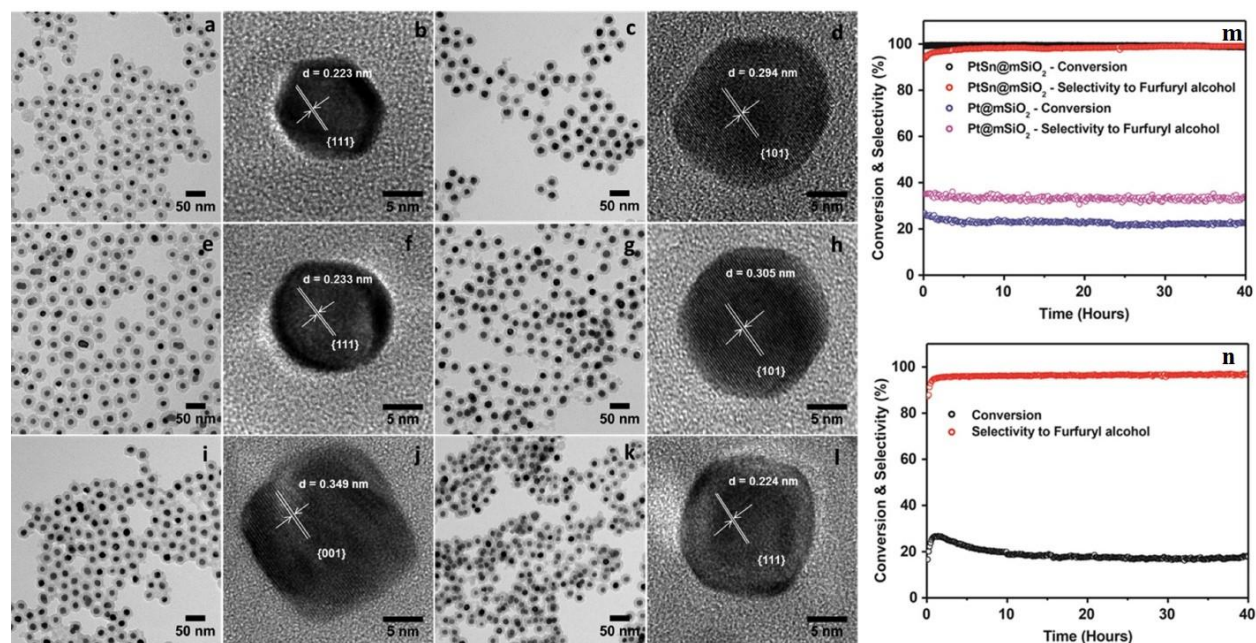
Figure 1.4 Characterization and catalytic activity of intermetallic $Pt_xM@mSiO_2$. (Left) TEM and HRTEM images of (a,b) $Pt@mSiO_2$ and (c-l) intermetallic $Pt_xM@mSiO_2$ for (c,d) PtSn, (e,f) Pt_3Sn, (g,h) PtPb, (i,j) PtZn, and (k,l) Pt_3Zn. Lattice spacings calculated from the HRTEM images as indicated. (Right) (a) Catalytic performance of $Pt@mSiO_2$ and $PtSn@mSiO_2$. (b) Furfural hydrogenation by $PtSn@mSiO_2$ with a lower amount of the catalyst (0.26 mg, Pt mass = 0.124 mg). Reaction conditions for furfural hydrogenation: Furfural/H_2/He = 0.023/11.4/8.6 mL/min, 160 °C. Adapted with permission from Ref. 104.

Yin and coworkers synthesized alloy AuAg NPs for plasmonic application by encapsulating Au@Ag core-shell NPs and coating them in SiO_2 to withstand the 1000 °C annealing temperature used for mixing. Base was used to dissolve the SiO_2 shell post-annealing, and the particles were used for surface-enhanced Raman spectroscopy.[103] Huang and coworkers used a similar method to form IMC PtSn NPs, coating Pt NPs in a SiO_2 shell and reducing $SnCl_2$ to form an encapsulated random alloy. Annealing at 600 °C yielded an IMC $PtSn@SiO_2$ nanoparticle that

15

was used for the selective hydrogenation of furfural, nitroarenes, and acetylene.[104-106] The Huang group recently built on this initial study to show that the degree of ordering, homogeneity of mixing, and surface composition could have a large impact on catalytic activity for the hydrogenation of furfural.[107] Another method introduced Zn into Pt NPs supported on multi-walled carbon nanotubes, with an annealing step to form PtZn IMCs followed by etching of the surrounding SiO_2 shell.[108] The SiO_2 shell served to maintain small NP size during the annealing process, with the resulting particles proving active for the MOR. This system, dubbed a "self-contained nano-reactor", also serves as an excellent platform for the study of metallic mixing and IMC phase formation.[106, 109]

Composition	Catalytic Reaction	Ref	Year
PtFe@MgO	HER, ORR	98	2015
PtFe@Pt@MgO	HER, ORR	99	2018
PtSn@SiO_2	Selective Hydrogenation	101-104	2016-19
PtZn@SiO_2	MOR	105	2017

Table 1.3 IMC Nanocatalysts synthesized through annealing in an oxide shell.

The use of an inorganic shell serves as a hybrid approach that combines some of the benefits of supported annealing (increased stability) and colloidal approaches (tunability and surface structure control; to be discussed later). However, the shell provides a barrier to catalytic activity that must be either porous, which still may introduce diffusion limitations, or etched away. This approach is fairly new, so work must be done to expand to new compositions and reactions.

Overall, though, this method is highly tunable, with many synthetic handles that creative synthetic chemists can use to their advantage – an excellent selling point for future investigations.

1.4 Bottom-Up Methods

Rather than applying bulk IMC fabrication principles to the synthesis of NPs, bottom-up methods seek to bring the fine control of NP synthesis to IMC construction. Ideally, these methods could unleash the full potential of IMC NPs, combining precise atomic composition with controlled faceting to mold the entirety of surface reaction sites – a surface composed entirely of single atom catalysts, if you will. The realization of this possibility, of course, is rife with challenges. The raw thermodynamics that underpins IMC formation is not a natural pair with the far-from-equilibrium, highly active shapes that define modern nanocatalysts. Nevertheless, progress has been made toward realizing bottom-up IMC NPs.

1.4.1 Colloidal

Colloidal methods rely on the rich history of nanoparticle synthesis to reduce metal precursors of constituent elements to form NPs with a mixed metallic structure. An annealing step is often used to induce atomic diffusion and a disorder-to-order transition, though temperatures are often kept mild enough such that no further protection (e.g. anchoring to a support) of the nanostructures is required. Simple coreduction to immediately form IMCs is challenging as there can be large differences in the reduction potentials of the desired metals that prevents a simple nucleation and growth process.

Schaak and coworkers established the use of colloidal methods to form IMC NPs,[110-124] but, though they synthesized catalytically relevant materials, their application of synthesized IMC

NPs to catalysis was limited. However, many groups have built on their foundational work to synthesize nanocatalysts.

DiSalvo, Abe, and coworkers coreduced $Pt(1,5\text{-cyclooctadiene})Cl_2$ and $Ti(\text{tetrahydrofuran})_2Cl_4$ with sodium naphthalide in tetrahydrofuran to form small random alloy Pt_3Ti, which they converted to larger IMC Pt_3Ti NPs through 600 °C annealing under vacuum.[125] The ordered catalysts outpaced Pt, Pt-Ru, and their disordered counterparts for the FOR, though the authors note that their large size (induced by the relatively high annealing temperature) leaves room for improvement of their synthetic method. Saravanan, Abe, and coworkers later found that adding dispersed SiO_2 supports could serve to anchor the particles during and retain the small Pt_3Ti IMC NPs, which proved active for the oxidation of CO.[126] Ramesh, Abe, and coworkers employed the same reducing agent to form Pt_3Zr IMC NPs, with different annealing temperatures inducing either a cubic or hexagonal crystal structure.[127] The hexagonal NPs showed better activity for the oxidation of ethanol and formic acid, which was credited to its higher surface energy. DiSalvo and coworkers synthesized Pt_3Ti and Pt_3V using a similar method with KEt_3BH in THF, which displayed significant enhancement for the MOR relative to pure Pt.[128] Though they used relatively high annealing temperatures, insoluble KCl served as a matrix that prevented sintering. Their method also yielded IMC Pt_3Cr NPs, with the best results produced when using annealing temperatures below the KCl melting point to reduce sintering, that were highly active for the ORR.[129] Peter and coworkers likewise used $NaBH_4$ for the coreduction of Pd and Cu to form PdCu IMC NPs, with the unsupported ordered structure efficiently oxidizing benzylamine to dibenzylimine.[130]

Schlogl and coworkers used coprecipitation to synthesize precursor $Pd_{0.025}Mg_{0.675}Ga_{0.3}(OH)_2(CO_3)_{0.15}$, which, when annealed under H_2 at 550 °C, formed Pd_2Ga IMC

NPs on a porous MgO/MgGa$_2$O$_4$ support that were several orders of magnitude more active for acetylene semihydrogenation than bulk Pd$_2$Ga.[131] Armbruster and coworkers used LiEt$_3$BH in THF as a strong reducing agent and a 185 °C annealing step to form PdGa and Pd$_2$Ga IMC NPs, which served as effective catalysts for the semihydrogenation of acetylene, showing enhancement over the bulk materials.[132] Chen and coworkers synthesized IMC AuCu$_3$ NRs through a seeded coreduction strategy and subsequent annealing at 280 °C.[133] They found that both shape and order had an effect on the reduction of 4-nitrophenol, with activity increasing in the order of disordered Cu$_3$Au NPs, ordered Cu$_3$Au NPs, disordered Cu$_3$Au nanorods, and, most active, ordered Cu$_3$Au nanorods.
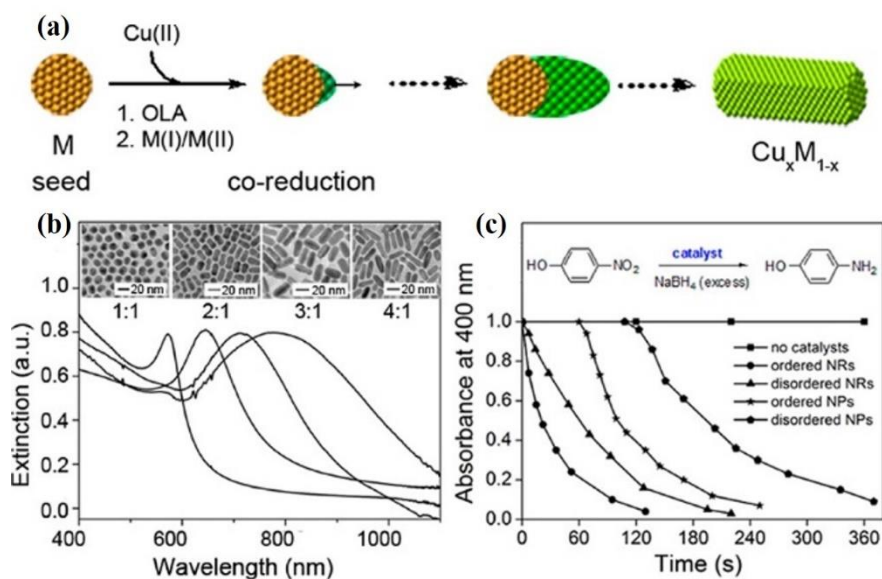
Figure 1.5 Synthesis and characterization of bimetallic Cu-based nanostructures. (a) Schematic illustration of the seeded coreduction strategy for the synthesis of bimetallic Cu-based nanorods. (b) UV–vis–NIR spectra of Cu$_3$Au nanorods with LSPR peaks at 572, 643, 716, and 781 nm as aspect ratio increases from 1:1 to 4:1. The insets are the corresponding TEM images. (c) Plot of

normalized absorbance (I/I_0) of p-nitrophenolate ion at 400 nm as a function of time for different catalysts. Adapted with permission from Ref. 133.

Wei and coworkers synthesized NiGa/MgO, CoSn/Al$_2$ZnO$_4$, and NiIn/Al$_2$O$_3$ supported IMC NPs by annealing layered double hydroxides, which proved active for the selective hydrogenation of several different carbonyl compounds.[134-136] Guided by DFT, Li and coworkers synthesized colloidal PdIn and Pd$_3$In IMC NPs through polyol and hot injection approaches, respectively.[137] The PdIn NPs, dried on a MgAl$_2$O$_4$ support, showed high selectivity for the semihydrogenation of several alkynes, which was assigned to the isolation of single-atom Pd sites in the IMC crystal structure. Peter and coworkers synthesized Ni$_x$Sn$_y$-Al$_2$O$_3$ through coprecipitation, finding that order and composition could affect furfural hydrogenation, serving as handles to tune activity and selectivity based on intermediate adsorption energies.[138] Yang and coworkers synthesized ordered AuCu nanoparticles through seeded coreduction, altering synthesis temperature and time to determine the degree of ordering.[139] Increasing atomic order suppressed the HER and increased the faradaic efficiency of CO$_2$ reduction.

Composition	Catalytic Reaction	Ref	Year
Pt$_3$Ti	FOR	125, 126	2008,10
Pt$_3$Zr	EOR, FOR	127	2014
Pt$_3$Ti, Pt$_3$V	MOR	128	2014
Pt$_3$Cr	ORR	129	2015
PdCu	Organic Oxidation	130	2017

Pd$_2$Ga	Selective Hydrogenation	131	2011
Pd$_2$Ga, PdGa	Selective Hydrogenation	132	2011
AuCu$_3$	Organic Reduction	133	2013
NiGa, CoSn, NiIn	Selective Hydrogenation	134-136	2013-16
PdIn	Selective Hydrogenation	137	2017
Ni$_x$Sn$_y$	Selective Hydrogenation	138	2018
AuCu	CO$_2$RR	139	2017

Table 1.4 IMC Nanocatalysts synthesized through colloidal approaches.

Colloidal methods have thus far been the most effective strategy for expanding IMC NP catalytic scope, as evidenced by the diversity of their compositions and catalyzed reactions. Indeed, it might even be said that more attention should be given to applying colloidal approaches to the Pt-based ORR nanocatalysts that dominate other synthesis methods. Future work can, however, seek to further enrich the scope of materials and reactions to which colloidal IMC NPs are applied. Overall, the colloidal synthesis of IMC NPs has made significant progress over the past decade, but a wide array of compositions and geometries remain.

1.5 Conclusion

The future remains bright for IMC NPs, with their recent increase in synthetic attention yielded nanocatalysts with a wide range of compositions and catalytic applications. Bulk annealing offers a route to IMC NPs with complex compositions, with the ordered IMC crystal structure allowing for controlled catalysis despite the rough, equilibrium NP shapes generated. Future work should be done to focus on expanding the compositional and catalytic scope of IMC NPs

synthesized through bulk annealing, with synthesized structures serving to identify new targets for other synthetic methods. Annealing on a support already has served as a path to a wide array of IMC nanocatalysts. Though some diversity exists, work is still needed to increase the number of IMC NPs that are Pt-based ORR catalysts. Annealing in an inorganic shell has combined supported and colloidal methods to yield a synthetically tunable showground for the study of IMC formation and its application to catalysis, but this nascent field must move beyond the few identified compositions and reactions. Colloidal methods have only begun to scratch the surface of the rich alloy and single-metal approaches that have profoundly impacted modern catalysis. Overall, though, the past 15 years has seen the rise of IMC NPs to the forefront of nanocatalysis. Their promise is clear, and intelligent research directions continue the march toward generating a set of a design rules for the creation of atomically-controlled, made-to-order nanocatalysts.

The understanding of the nanocrystal surface and its impact on catalysis is fundamental to the work presented in the following chapters. Chapter 2 presents the synthesis of a layered core-shell nanostructure that serves as an arena for the study of the fundamental processes involved nanoscale metallic mixing. Combined with theoretical analysis, this work provides the first step in a route toward shape-controlled IMC nanocatalysts. Chapter 3 discusses the fabrication of core-alloyed shell NPs that allow for the identification of the degree of lattice strain at the NP surface. Chapter 4 builds on the previous two chapters to discuss how the two methods can be applied to catalysis. Overall, the understanding presented herein represents a brick in the foundation of the construction and application of multimetallic nanocatalysts.

References

1.   Energy Information Adminstration, U. S., International Energy Outlook 2019. **2019**.

2.   Shao, M.; Chang, Q.; Dodelet, J.-P.; Chenitz, R., Recent Advances in Electrocatalysts for Oxygen Reduction Reaction. *Chem. Rev.* **2016,** *116*, 3594-3657.

3.   Morozan, A.; Jousselme, B.; Palacin, S., Low-platinum and platinum-free catalysts for the oxygen reduction reaction at fuel cell cathodes. *Energ. Environ. Sci.* **2011,** *4*, 1238-1254.

4.   Wang, C.; Markovic, N. M.; Stamenkovic, V. R., Advanced Platinum Alloy Electrocatalysts for the Oxygen Reduction Reaction. *ACS Catal.* **2012,** *2*, 891-898.

5.   Zhang, L.; Roling, L. T.; Wang, X.; Vara, M.; Chi, M.; Liu, J.; Choi, S.-I.; Park, J.; Herron, J. A.; Xie, Z.; Mavrikakis, M.; Xia, Y., Platinum-based nanocages with subnanometer-thick walls and well-defined, controllable facets. *Science* **2015,** *349*, 412-416.

6.   Antolini, E., Formation of carbon-supported PtM alloys for low temperature fuel cells: a review. *Mater. Chem. Phys.* **2003,** *78*, 563-573.

7.   Strasser, P.; Koh, S.; Anniyev, T.; Greeley, J.; More, K.; Yu, C.; Liu, Z.; Kaya, S.; Nordlund, D.; Ogasawara, H.; Toney, M. F.; Nilsson, A., Lattice-strain control of the activity in dealloyed core-shell fuel cell catalysts. *Nat. Chem.* **2010,** *6*, 32-41.

8.   Bing, Y.; Liu, H.; Zhang, L.; Ghosh, D.; Zhang, J., Nanostructured Pt-alloy electrocatalysts for PEM fuel cell oxygen reduction reaction. *Chem. Soc. Rev.* **2010,** *39*, 2184-2202.

9.   Zhao, Y.; Yu, J. K.; Wu, L. L.; Wan, B.; Zhang, Y. K.; Gao, R.; Zhang, J. W.; Gou, H. Y., Mechanical properties and electronic structures of diverse Pt-Al intermetallics: First-principles calculations. *Comp Mater Sci* **2016,** *124*, 273-281.

10.   Furukawa, S.; Ehara, K.; Ozawa, K.; Komatsu, T., A study on the hydrogen activation properties of Ni-based intermetallics: a relationship between reactivity and the electronic state. *Phys Chem Chem Phys* **2014,** *16* (37), 19828-19831.

11.   Xiao, W.; Lei, W.; Gong, M.; Xin, H. L.; Wang, D., Recent Advances of Structurally Ordered Intermetallic Nanoparticles for Electrocatalysis. *ACS Catal.* **2018,** *8* (4), 3237-3256.

12.   Dikshtein, I.; Koledov, V.; Shavrov, V.; Tulaikova, A.; Cherechukin, A.; Buchelnikov, V.; Khovailo, V.; Matsumoto, M.; Takagi, T.; Tani, J., Phase transitions in intermetallic compounds Ni-Mn-Ga with shape memory effect. *IEEE Trans.* **1999,** *35* (5), 3811-3813.

13.   Li, B.-Y.; Rong, L.-J.; Li, Y.-Y., Stress-strain behavior of porous Ni-Ti shape memory intermetallics synthesized from powder sintering. *Intermetallics* **2000,** *8*, 643-646.

14.   Uijttewaal, M. A.; Hickel, T.; Neugebauer, J.; Gruner, M. E.; Entel, P., Understanding the Phase Transitions of the Ni_2MnGa Magnetic Shape Memory System from First Principles. *Phys. Rev. Lett.* **2009,** *102*, 035702/1-035702/4.

15.   Evans, M. J.; Wu, Y.; Kranak, V. F.; Newman, N.; Reller, A.; Garcia-Garcia, F. J.; Haeussermann, U., Structural properties and superconductivity in the ternary intermetallic compounds MAB (M=Ca, Sr, Ba; A=Al, Ga, In; B=Si, Ge, Sn). *Phys. Rev. B* **2009,** *80* (6), 064514.

16.   Chen, J.; Kuriyama, N.; Takeshita, H. T.; Tanaka, H.; Sakai, T.; Haruta, M., Hydrogen storage alloys with $PuNi_3$-type structure as metal hydride electrodes. *Electrochem. Solid. St.* **2000,** *3*, 249-252.

17.   Chou, K.-C.; Xu, K., A new model for hydriding and dehydriding reactions in intermetallics. *Intermetallics* **2007,** *15*, 767-777.

18.   Fernandez, J. F.; Cuevas, F.; Leardini, F.; Bodega, J.; Ares, J. R.; Garces, G.; Perez, P.; Sanchez, C., A new pseudo-binary $Mg_{(6)}Ni_{(0.5)}Pd_{(0.5)}$ intermetallic compound stabilised by Pd for hydrogen storage. *J. Alloy. Compd.* **2010,** *495* (2), 663-666.

19.   Bud'ko, S. L.; Lapertot, G.; Petrovic, C.; Cunningham, C. E.; Anderson, N.; Canfield, P. C., Boron Isotope Effect in Superconducting MgB_2. *Phys. Rev. Lett.* **2001,** *86*, 1877-1880.

20.   Cava, R. J.; Takagi, H.; Zandbergen, H. W.; Krajewski, J. J.; Peck Jr., W. F.; Siegrist, T.; Batlogg, B.; van Dover, R. B.; Felder, R. J.; Mizuhashi, K.; Lee, J. O.; Eisaki, H.; Uchida, S., Superconductivity in the quaternary intermetallic compounds $LnNi_2B_2C$. *Nature* **1994,** *367*, 252-253.

21.   Clarke, S. M.; Walsh, J. P. S.; Amsler, M.; Malliakas, C. D.; Yu, T.; Goedecker, S.; Wang, Y.; Wolverton, C.; Freedman, D. E., Discovery of Superconducting Cu-Bi Intermetallic Compound by High-Pressure Synthesis. *Angew. Chem.* **2016,** *55*, 13446-13449.

22.   Hasché, F.; Oezaslan, M.; Strasser, P., Activity, Structure and Degradation of Dealloyed $PtNi_3$ Nanoparticle Electrocatalyst for the Oxygen Reduction Reaction in PEMFC. *J. Electrochem. Soc.* **2012,** *159* (1), B24-B33.

23.   Stamenkovic, V. R.; Fowler, B.; Mun, B. S.; Wang, G.; Ross, P. N.; Lucas, C. A.; Markovic, N. M., Improved Oxygen Reduction Activity on $Pt_3Ni(111)$ via Increased Surface Site Availability. *Science* **2007,** *315*, 493-497.

24.   Komatsu, T.; Tamura, A., Pt_3Co and PtCu intermetallic compounds: Promising catalysts for preferentialoxidation of CO in excess hydrogen. *J. Catal.* **2008,** *258*, 306-314.

25.   Wang, D.; Xin, H. L.; Hovden, R.; Wang, H.; Yu, Y.; Muller, D. A.; DiSalvo, F. J.; Abruña, H. D., Structurally ordered intermetallic platinum–cobalt core–shell nanoparticles with enhanced activity and stability as oxygen reduction electrocatalysts. *Nat. Mater.* **2013,** *12*, 81-87.

26.   Sun, S.; Murray, C. B.; Weller, D.; Folks, L.; Moser, A., Monodisperse FePt Nanoparticles and Ferromagnetic FePt Nanocrystal Superlattices. *Science* **2000,** *287*, 1989-1992.

27.   Elkins, K. E.; Vedantam, T. S.; Liu, J. P.; Zeng, H.; Sun, S.; Ding, Y.; Wang, Z. L., Ultrafine FePt Nanoparticles Prepared by the Chemical Reduction Method. *Nano Lett.* **2003,** *3* (12), 1647-1649.

28.   Teng, X.; Yang, H., Synthesis of Face-Centered Tetragonal FePt Nanoparticles and Granular Films from Pt@Fe$_2$O$_3$ Core-Shell Nanoparticles. *J. Am. Chem. Soc.* **2003,** *125*, 14559-14563.

29.   Narayanan, R.; El-Sayed, M. A., Catalysis with Transition Metal Nanoparticles in Colloidal Solution: Nanoparticle Shape Dependence and Stability. *J. Phys. Chem. C* **2005,** *109*, 12663-12676.

30.   Cao, S.; Tao, F.; Tang, Y.; Li, Y.; Yu, J., Size- and shape-dependent catalytic performances of oxidation and reduction reactions on nanocatalysts. *Chem. Soc. Rev.* **2016,** *45*, 4747-4765.

31.   Zhao, M.; Wang, X.; Yang, X.; Gilroy, K. D.; Qin, D.; Xia, Y., Hollow Metal Nanocrystals with Ultrathin, Porous Walls and Well-Controlled Surface Structures. *Adv. Mater.* **2018,** *30*, 1801956.

32.   Yin, A.-X.; Min, X.-Q.; Zhang, Y.-W.; Yan, C.-H., Shape-Selective Synthesis and Facet-Dependent Enhanced Electrocatalytic Activity and Durability of Monodisperse Sub-10 nm Pt-Pd Tetrahedrons and Cubes. *J. Am. Chem. Soc.* **2011,** *133*, 3816-3819.

33.   Xu, D.; Bliznakov, S.; Liu, Z.; Fang, J.; Dimitrov, N., Composition-Dependent Electrocatalytic Activity of Pt-Cu Nanocube Catalysts for Formic Acid Oxidation. *Angew. Chem.* **2010,** *49*, 1282-1285.

34.   Zhang, J.; Yang, H.; Fang, J.; Zou, S., Synthesis and Oxygen Reduction Activity of Shape-Controlled Pt$_3$Ni Nanopolyhedra. *Nano Lett.* **2010,** *131*, 7542-7543.

35.   Cui, C.; Gan, L.; Li, H.-H.; Yu, S.-H.; Heggen, M.; Strasser, P., Octahedral PtNi Nanoparticle Catalysts: Exceptional Oxygen Reduction Activity by Tuning the Alloy Particle Surface Composition. *Nano Lett.* **2012,** *12*, 5885-5889.

36.   Kim, D.; Resasco, J.; Yu, Y.; Asiri, A. M.; Yang, P., Synergistic geometric and electronic effects for electrochemical reduction of carbon dioxide using gold-copper bimetallic nanoparticles. *Nat. Commun.* **2014,** *5*, 4948.

37.   Xu, Z.; Lai, E.; Shao-Horn, Y.; Hamad-Schifferli, K., Compositional dependence of the stability of AuCu alloy nanoparticles. *Chem. Commun.* **2012,** *48*, 5626-5628.

38.   Liu, Q.; Yan, Z.; Henderson, N. L.; Bauer, J. C.; Goodman, D. W.; Batteas, J. D.; Schaak, R. E., Synthesis of CuPt Nanorod Catalysts with Tunable Lengths. *J. Am. Chem. Soc.* **2009,** *131*, 5720-5721.

39.   Wu, J.; Gross, A.; Yang, H., Shape and Composition-Controlled Platinum Alloy Nanocrystals Using Carbon Monoxide as Reducing Agent. *Nano Lett.* **2011,** *11*, 798-802.

40.   Gan, L.; Heggen, M.; Cui, C.; Strasser, P., Thermal Facet Healing of Concave Octahedral Pt-Ni Nanoparticles Imaged in Situ at the Atomic Scale: Implications for the Rational Synthesis of Durable High-Performance ORR Electrocatalysts. *ACS Catal.* **2016,** *6*, 692-695.

41.   Beermann, V.; Gocyla, M.; Kuhl, S.; Padgett, E.; Schmies, H.; Goerlin, M.; Erini, N.; Shviro, M.; Heggen, M.; Dunin-Borkowski, R. E.; Muller, D. A.; Strasser, P., Tuning the Electrocatalytic Oxygen Reduction Reaction Activity and Stability of Shape-Controlled Pt–Ni Nanoparticles by Thermal Annealing − Elucidating the Surface Atomic Structural and Compositional Changes. *J. Am. Chem. Soc.* **2017,** *139*, 16536-16547.

42.   Chen, C.; Kang, Y.; Huo, Z.; Zhu, Z.; Huang, W.; Xin, H. L.; Snyder, J. D.; Li, D.; Herron, J. A.; Mavrikakis, M.; Chi, M.; More, K. L.; Li, Y.; Markovic, N. M.; Somorjai, G. A.; Yang, P.; Stamenkovic, V. R., Highly Crystalline Multimetallic Nanoframes with Three-Dimensional Electrocatalytic Surfaces. *Science* **2014,** *343* (6177), 1339-1343.

43.   Tian, X.; Zhao, X.; Su, Y.-Q.; Wang, L.; Wang, H.; Dang, D.; Chi, B.; Liu, H.; Hensen, E. J. M.; Lou, X. W.; Xia, B. Y., Engineering bunched Pt-Ni alloy nanocages for efficient oxygen reduction in practical fuel cells. *Science* **2019,** *366*, 850-856.

44.   Armbruster, M.; Schlogl, R.; Grin, Y., Intermetallic compounds in heterogeneous catalysis -- a quickly developing field. *Adv. Mater.* **2014,** *15*, 034803.

45.   Gilroy, K. D.; Ruditskiy, A.; Peng, H.-C.; Qin, D.; Xia, Y., Bimetallic Nanocrystals: Syntheses, Properties, and Applications. *Chem. Rev.* **2016,** *116*, 10414-10472.

46.   Furukawa, S.; Komatsu, T., Intermetallic Compounds: Promising Inorganic Materials for Well-Structured and Electronically Modified Reaction Environments for Efficient Catalysis. *ACS Catal.* **2017,** *7*, 735-765.

47.   Yan, Y.; Du, J. S.; Gilroy, K. D.; Yang, D.; Xia, Y.; Zhang, H., Intermetallic Nanocrystals: Syntheses and Catalytic Applications. *Adv. Mater.* **2017,** *29*, 1605997.

48.   Xiao, W.; Lei, W.; Gong, M.; Xin, H. L.; Wang, D., Recent Advances of Structurally Ordered Intermetallic Nanoparticles for Electrocatalysis. *ACS Catal.* **2018,** *8*, 3237-3256.

49.   Dasgupta, A.; Rioux, R. M., Intermetallics in catalysis: An exciting subset of multimetallic catalysts. *Catal. Today* **2019,** *330*, 2-15.

50.   Rößner, L.; Armbruster, M., Electrochemical Energy Conversion on Intermetallic Compounds: A Review. *ACS Catal.* **2019,** *9*, 2018-2062.

51.   Sun, S.; Li, J., Intermetallic Nanoparticles: Synthetic Control and Their Enhanced Electrocatalysis. *Acc. Chem. Res.* **2019,** *52*, 2015-2025.

52. Yang, Y.; Wei, M., Intermetallic compound catalysts: synthetic scheme, structure characterization and catalytic application. *J. Mater. Chem. A* **2020,** *8*, 2207-2221.

53. Rodriguez, J. A.; Liu, P.; Hrbek, J.; Evans, J.; Perez, M., Water gas shift reaction on Cu and Au nanoparticles supported on $CeO_2(111)$ and $ZnO(0001)$: intrinsic activity and importance of support interactions. *Angew. Chem.* **2007,** *46*, 1329-1332.

54. Vayssilov, G. N.; Lykhach, Y.; Migani, A.; Staudt, T.; Petrova, G. P.; Tsud, N.; Skala, T.; Bruix, A.; Illas, F.; Prince, K. C.; Matolin, V.; Neyman, K. M.; Libuda, J., Support nanostructure boosts oxygen transfer to catalytically active platinum nanoparticles. *Nat. Mater.* **2011,** *10*, 310-315.

55. Yoon, S.; Oh, K.; Liu, F.; Seo, J. H.; Somorjai, G. A.; Lee, J. H.; An, K., Specific Metal-Support Interactions between Nanoparticle Layers for Catalysts with Enhanced Methanol Oxidation Activity. *ACS Catal.* **2018,** *8*, 5391-5398.

56. Jaksic, J. M.; Vojnovic, M. V.; Krstajic, N. V., Kinetic Analysis of Hydrogen Evolution at Ni-Mo Alloy Electrodes. *Electrochim. Acta* **2000,** *45*, 4151-4158.

57. Osswald, J.; Giedigkeit, R.; Jentoft, R. E.; Armbruster, M.; Girgsdies, F.; Kovnir, K.; Ressler, T.; Grin, Y.; Schlogl, R., Palladium-Gallium Intermetallic Compounds for the Selective Hydrogenation of Acetylene Part II: Surface Characterization and Catalytic Performance. *J. Catal.* **2008,** *258*, 210-218.

58. Osswald, J.; Kovnir, K.; Armbruster, M.; Giedigkeit, R.; Jentoft, R. E.; Wild, U.; Grin, Y.; Schlogl, R., Palladium-Gallium Intermetallic Compounds for the Selective Hydrogenation of Acetylene Part I: Preparation and Structural Investigation under Reaction Conditions. *J. Catal.* **2008,** *258*, 219-227.

59. Kovnir, K.; Osswald, J.; Armbruster, M.; Teschner, D.; Weinberg, G.; Wild, U.; Knop-Gericke, A.; Ressler, T.; Grin, Y.; Schlogl, R., Etching of the Intermetallic Compounds PdGa and Pd_3Ga_7: An Effective Way to Increase Catalytic Activity. *J. Catal.* **2009,** *264*, 93-103.

60. Armbruster, M.; Kovnir, K.; Behrens, M.; Teschner, D.; Grin, Y.; Schlogl, R., Pd-Ga Intermetallic Compounds as Highly Selective Semihydrogenation Catalysts. *J. Am. Chem. Soc.* **2010,** *132*, 14745-14747.

61. Kovnir, K.; Armbruster, M.; Teschner, D.; Venkov, T. V.; Szentmiklosi, L.; Jentoft, F. C.; Knop-Gericke, A.; Grin, Y.; Schlogl, R., In situ surface characterization of the intermetallic compound PdGa – A highly selective hydrogenation catalyst. *Surf. Sci.* **2009,** *603*, 1784-1792.

62. Friedrich, M.; Villaseca, S. A.; Szentmiklosi, L.; Teschner, D.; Armbruster, M., Order-Induced Selectivity Increase of $Cu_{60}Pd_{40}$ in the Semi-Hydrogenation of Acetylene. *Materials* **2013,** *6*, 2958-2977.

63.   Matselko, O.; Zimmermann, R. R.; Ormeci, A.; Burkhardt, U.; Gladyshevskii, R.; Grin, Y.; Armbruster, M., Revealing Electronic Influences in the Semihydrogenation of Acetylene. *J. Phys. Chem. C* **2018**, *122*, 21891-21896.

64.   Lang, X.-Y.; Han, G.-F.; Xiao, B.-B.; Gu, L.; Yang, Z.-Z.; Wen, Z.; Zhu, Y.-F.; Zhao, M.; Li, J.-C.; Jiang, Q., Mesostructured Intermetallic Compounds of Platinum and Non-Transition Metals for Enhanced Electrocatalysis of Oxygen Reduction Reaction. *Adv. Funct. Mater.* **2015,** *25*, 230-237.

65.   Cheng, T.; Lang, X.-Y.; Han, G.-F.; Yao, R.-Q.; Wen, Z.; Jiang, Q., Nanoporous $(Pt_{1-x}Fe_x)_3Al$ intermetallic compounds for greatly enhanced oxygen reduction catalysis. *J. Mater. Chem. A* **2016**, *4*, 18878-18884.

66.   Han, G.-F.; Gu, L.; Lang, X.-Y.; Xiao, B.-B.; Yang, Z.-Z.; Wen, Z.; Jiang, Q., Scalable Nanoporous $(Pt_{1-x}Ni_x)_3Al$ Intermetallic Compounds as Highly Active and Stable Catalysts for Oxygen Electroreduction. *ACS Appl. Mater. Inter.* **2016**, *8*, 32910-32917.

67.   Yao, R.-Q.; Han, L.-P.; Lang, X.-Y.; Cheng, T.; Wen, Z.; Liu, G.; Jiang, Q., Nanoporous $(Pt_{1-x}Co_x)_3Al$ intermetallic compound as a high-performance catalyst for oxygen reduction reaction. *Int. J. Hydrogen Energ.* **2018**, *43*, 19947-19954.

68.   Han, L.-P.; Yao, R.-Q.; Wan, W.-B.; Shi, H.; Wen, Z.; Lang, X.-Y.; Jiang, Q., Hierarchical nanoporous intermetallic compounds with self-grown transition-metal hydroxides as bifunctional catalysts for the alkaline hydrogen evolution reaction. *J. Mater. Chem. A* **2019,** *7*, 25925-25931.

69.   Sun, J.-S.; Wen, Z.; Han, L. P.; Chen, Z.-W.; Lang, X.-Y.; Jiang, Q., Nonprecious Intermetallic Al_7Cu_4Ni Nanocrystals Seamlessly Integrated in Freestanding Bimodal Nanoporous Copper for Efficient Hydrogen Evolution Catalysis. *Adv. Funct. Mater.* **2018**, *28*, 1706127.

70.   Alloyeau, D.; Langlois, C.; Ricolleau, C.; Le Bouar, Y.; Louiseau, A., A TEM in situ experiment as a guideline for the synthesis of as-grown ordered CoPt nanoparticles. *Nanotechnology* **2007,** *18*, 375301.

71.   Alloyeau, D.; Ricolleau, C.; Mottet, C.; Oikawa, T.; Langlois, C.; Le Bouar, Y.; Braidy, N.; Loiseau, A., Size and shape effects on the order–disorder phase transition in CoPt nanoparticles. *Nat. Mater.* **2009,** *8*, 940-946.

72.   Oezaslan, M.; Hasche, F.; Strasser, P., In Situ Observation of Bimetallic Alloy Nanoparticle Formation and Growth Using High-Temperature XRD. *Chem. Mater.* **2011**, *23*, 2159-2165.

73.   Zhang, S.; Qi, W.; Huang, B., Size effect on order-disorder transition kinetics of FePt nanoparticles. *J. Chem. Phys.* **2014**, *140*, 044328.

74.	Chi, M.; Wang, C.; Lei, Y.; Wang, G.; Dongguo, L.; More, K. L.; Lupini, A.; Allard, L. F.; Markovic, N. M.; Stamenkovic, V. R., Surface faceting and elemental diffusion behaviour at atomic scale for alloy nanoparticles during in situ annealing. *Nat. Commun.* **2015,** *6*, 8925.

75.	Williams, B. P.; Young, A. P.; Andoni, I.; Han, Y.; Lo, W.-S.; Golden, M.; Yang, J.; Lyu, L.-M.; Kuo, C.-H.; Evans, J. W.; Huang, W.; Tsung, C.-K., Strain-Enhanced Metallic Intermixing in Shape-Controlled Multi-layered Core-Shell Nanostructures: Toward Shaped Intermetallics. *Angew. Chem.* **2020**.

76.	Bauer, J. C.; Chen, X.; Liu, Q.; Phan, T.-H.; Schaak, R. E., Converting nanocrystalline metals into alloys and intermetallic compounds for application in catalysis. *J. Mater. Chem.* **2008,** *18*, 275-282.

77.	Ji, X.; Lee, K. T.; Holden, R.; Zhang, L.; Zhang, J.; Botton, G. A.; Couillard, M.; Nazar, L. F., Nanocrystalline intermetallics on mesoporous carbon for direct formic acid fuel cell anodes. *Nat. Chem.* **2010,** *2*, 286-293.

78.	Li, J.; Jilani, S. Z.; Lin, H.; Liu, X.; Wei, K.; Jia, Y.; Zhang, P.; Chi, M.; Tong, Y. J.; Xi, Z.; Sun, S., Ternary CoPtAu Nanoparticles as a General Catalyst for Highly Efficient Electro-oxidation of Liquid Fuels. *Angew. Chem.* **2019,** *58*, 11527-11533.

79.	Komatsu, T.; Takasaki, M.; Ozawa, K.; Furukawa, S.; Muramatsu, A., PtCu Intermetallic Compound Supported on Alumina Active for Preferential Oxidation of CO in Hydrogen. *J. Phys. Chem. C* **2013,** *117*, 10483-10491.

80.	Furukawa, S.; Ozawa, K.; Komatsu, T., Preparation of alumina-supported intermetallic compounds. *RSC Adv.* **2013,** *3*, 23269-23277.

81.	Furukawa, S.; Suga, A.; Komatsu, T., Highly efficient aerobic oxidation of various amines using Pd_3Pb intermetallic compounds as catalysts. *Chem. Commun.* **2014,** *50*, 3277-3280.

82.	Furukawa, S.; Suga, A.; Komatsu, T., Mechanistic Study on Aerobic Oxidation of Amine over Intermetallic Pd_3Pb: Concerted Promotion Effects by Pb and Support Basicity. *ACS Catal.* **2015,** *5*, 1214-1222.

83.	Cui, C.-H.; Li, H.-H.; Liu, X.-J.; Gao, M.-R.; Yu, S.-H., Surface Composition and Lattice Ordering-Controlled Activity and Durability of CuPt Electrocatalysts for Oxygen Reduction Reaction. *ACS Catal.* **2012,** *2*, 916-924.

84.	Wang, D.; Yu, Y.; Xin, H. L.; Hovden, R.; Ercius, P.; Mundy, J. A.; Chen, H.; Richard, J. H.; Muller, D. A.; DiSalvo, F. J.; Abruña, H. D., Tuning Oxygen Reduction Reaction Activity via Controllable Dealloying: A Model Study of Ordered Cu_3Pt/C Intermetallic Nanocatalysts. *Nano Lett.* **2012,** *12*, 5230-5238.

85.   Chen, L.; Chan, M. C. Y.; Nan, F.; Bock, C.; Botton, G. A.; Mercier, P. H. J.; MacDougall, B. R., Compositional and Morphological Changes of Ordered Pt_xFe_y/C Oxygen Electroreduction Catalysts. *ChemCatChem* **2013,** *5*, 1449-1460.

86.   Prabhudev, S.; Bugnet, M.; Bock, C.; Botton, G. A., Strained Lattice with Persistent Atomic Order in Pt_3Fe_2 Intermetallic Core-Shell Nanocatalysts. *ACS Nano* **2013,** *7*, 6103-6110.

87.   Zou, L.; Li, J.; Yuan, T.; Zhou, Y.; Li, X.; Yang, H., Structural transformation of carbon-supported Pt_3Cr nanoparticles from a disordered to an ordered phase as a durable oxygen reduction electrocatalyst. *Nanoscale* **2014,** *6*, 10686-10692.

88.   Zhang, N.; Chen, X.; Lu, Y.; An, L.; Li, X.; Dingguo, X.; Zhang, Z.; Li, J., Nano-Intermetallic $AuCu_3$ Catalyst for Oxygen Reduction Reaction: Performance and Mechanism. *Small* **2014,** *10* (13), 2662-2669.

89.   Chung, D. Y.; Jun, S. W.; Yoon, G.; Kwon, S. G.; Shin, D. Y.; Seo, P.; Yoo, J. M.; Shin, H.; Chung, Y.-H.; Kim, H.; Mun, B. S.; Lee, K.-S.; Lee, N.-S.; Yoo, S. J.; Lim, D.-H.; Kang, K.; Sung, Y.-E.; Hyeon, T., Highly Durable and Active PtFe Nanocatalyst for Electrochemical Oxygen Reduction Reaction. *J. Am. Chem. Soc.* **2015,** *137*, 15478-15485.

90.   Zou, L.; Fan, J.; Zhou, Y.; Wang, C.; Li, J.; Zou, Z.; Yang, H., Conversion of PtNi alloy from disordered to ordered for enhanced activity and durability in methanol-tolerant oxygen reduction reactions. *Nano Res.* **2015,** *8*, 2777-2788.

91.   Kim, H. Y.; Cho, S.; Sa, Y. J.; Hwang, S.-M.; Park, G.-G.; Shin, T. J.; Jeong, H. Y.; Yim, S.-D.; Joo, S. H., Self-Supported Mesostructured Pt-Based Bimetallic Nanospheres Containing an Intermetallic Phase as Ultrastable Oxygen Reduction Electrocatalysts. *Small* **2016,** *38*, 5347-5353.

92.   Wang, T.; Liang, J.; Zhao, Z.; Li, S.; Lu, G.; Xia, Z.; Wang, C.; Luo, J.; Han, J.; Ma, C.; Huang, Y.; Li, Q., Sub-6 nm Fully Ordered $L1_0$-Pt–Ni–Co Nanoparticles Enhance Oxygen Reduction via Co Doping Induced Ferromagnetism Enhancement and Optimized Surface Strain. *Adv. Energy Mater.* **2019,** *9*, 1803771.

93.   Shao, L.; Zhang, W.; Armbruster, M.; Teschner, D.; Girgsdies, F.; Zhang, B.; Timpe, O.; Friedrich, M.; Schlogl, R.; Su, D. S., Nanosizing Intermetallic Compounds Onto Carbon Nanotubes: Active and Selective Hydrogenation Catalysts. *Angew. Chem.* **2011,** *50*, 10231-10235.

94.   Furukawa, S.; Yokoyama, A.; Komatsu, T., Efficient Catalytic System for Synthesis of trans-Stilbene from Diphenylacetylene Using Rh-Based Intermetallic Compounds. *ACS Catal.* **2014,** *4*, 3581-3585.

95.   Miyazaki, M.; Furukawa, S.; Takayama, T.; Yamazoe, S.; Komatsu, T., Surface Modification of PdZn Nanoparticles via Galvanic Replacement for the Selective Hydrogenation of Terminal Alkynes. *ACS Appl. Nano Mater.* **2019,** *2*, 3307-3314.

96.   Fiordaliso, E. M.; Sharafutdinov, I.; Carvalho, H. W. P.; Grunwaldt, J.-D.; Hansen, T. W.; Chorkendorff, I.; Wagner, J. B.; Damsgaard, C. D., Intermetallic $GaPd_2$ Nanoparticles on SiO_2 for Low-Pressure CO_2 Hydrogenation to Methanol: Catalytic Performance and In Situ Characterization. *ACS Catal.* **2015,** *5*, 5827-5836.

97.   Wang, J.; Zou, J.; Hu, X.; Ning, S.; Wang, X.; Kang, X.; Chen, S., Heterostructured intermetallic CuSn catalysts: high performance towards the electrochemical reduction of CO2 to formate. *J. Mater. Chem. A* **2019,** *7*, 27514.

98.   Chen, M.; Kim, J.; Liu, J. P.; Fan, H.; Sun, S., Synthesis of FePt Nanocubes and Their Oriented Self-Assembly. *J. Am. Chem. Soc.* **2006,** *128*, 7132-7133.

99.   Liu, F.; Zhu, J.; Yang, W.; Dong, Y.; Hou, Y.; Zhang, C.; Yin, H.; Sun, S., Building Nanocomposite Magnets by Coating a Hard Magnetic Corewith a Soft Magnetic Shell. *Angew. Chem.* **2014,** *53*, 2176-2180.

100.   Kim, J.; Lee, Y.; Sun, S., Structurally Ordered FePt Nanoparticles and Their Enhanced Catalysis for Oxygen Reduction Reaction. *J. Am. Chem. Soc.* **2010,** *132*, 4996-4997.

101.   Li, Q.; Wu, L.; Wu, G.; Su, D.; Lv, H.; Zhang, S.; Zhu, W.; Casimir, A.; Zhu, H.; Mendoza-Garcia, A.; Sun, S., New Approach to Fully Ordered fct-FePt Nanoparticles for Much Enhanced Electrocatalysis in Acid. *Nano Lett.* **2015,** *15*, 2468-2473.

102.   Li, J.; Xi, Z.; Pan, Y.-T.; Spendelow, J. S.; Duchesne, P. N.; Su, D.; Li, Q.; Yu, C.; Yin, Z.; Shen, B.; Kim, Y. S.; Zhang, P.; Sun, S., Fe Stabilization by Intermetallic $L1_0$-FePt and Pt Catalysis Enhancement in $L1_0$-FePt/Pt Nanoparticles for Efficient Oxygen Reduction Reaction in Fuel Cells. *J. Am. Chem. Soc.* **2018,** *140*, 2926-2932.

103.   Gao, C.; Hu, Y.; Wang, M.; Chi, M.; Yin, Y., Fully Alloyed Ag/Au Nanospheres: Combining the Plasmonic Property of Ag with the Stability of Au. *J. Am. Chem. Soc.* **2014,** *136*, 7474-7479.

104.   Maligal-Ganesh, R. V.; Xiao, C.; Goh, T. W.; Wang, L.-L.; Gustafson, J.; Pei, Y.; Qi, Z.; Johnson, D. D.; Zhang, S.; Tao, F.; Huang, W., A Ship-in-a-Bottle Strategy To Synthesize Encapsulated Intermetallic Nanoparticle Catalysts: Exemplified for Furfural Hydrogenation. *ACS Catal.* **2016,** *6*, 1754-1763.

105.   Pei, Y.; Qi, Z.; Goh, T. W.; Wang, L.-L.; Maligal-Ganesh, R. V.; MacMurdo, H. L.; Zhang, S.; Xiao, C.; Li, X.; Tao, F.; Johnson, D. D.; Huang, W., Intermetallic structures with atomic precision for selective hydrogenation of nitroarenes. *J. Catal.* **2017,** *356*, 307-314.

106.   Ma, T.; Wang, S.; Chen, M.; Maligal-Ganesh, R. V.; Wang, L.-L.; Johnson, D. D.; Kramer, M. J.; Huang, W.; Zhou, L., Toward Phase and Catalysis Control: Tracking the Formation of Intermetallic Nanoparticles at Atomic Scale. *Chem* **2019,** *5*, 1235-1247.

107.   Pei, Y.; Zhang, B.; Maligal-Ganesh, R. V.; Naik, P. J.; Goh, T. W.; MacMurdo, H. L.; Qi, Z.; Chen, M.; Behera, R. K.; Slowing, I. I.; Huang, W., Catalytic properties of intermetallic platinum-tin nanoparticles with non-stoichiometric compositions. *J. Catal.* **2019,** *374*, 136-142.

108.   Qi, Z.; Xiao, C.; Liu, C.; Goh, T. W.; Zhou, L.; Maligal-Ganesh, R. V.; Pei, Y.; Li, X.; Curtiss, L. A.; Huang, W., Sub-4 nm PtZn Intermetallic Nanoparticles for Enhanced Mass and Specific Activities in Catalytic Electrooxidation Reaction. *J. Am. Chem. Soc.* **2017,** *139*, 4762-4768.

109.   Chen, M.; Han, Y.; Goh, T. W.; Sun, R.; Maligal-Ganesh, R. V.; Pei, Y.; Tsung, C.-K.; Evans, J. W.; Huang, W., Kinetics, energetics, and size dependence of the transformation from Pt to ordered PtSn intermetallic nanoparticles. *Nanoscale* **2019,** *11* (5336-5345).

110.   Sra, A. K.; Schaak, R. E., Synthesis of Atomically Ordered AuCu and AuCu$_3$ Nanocrystals from Bimetallic Nanoparticle Precursors. *J. Am. Chem. Soc.* **2004,** *126*, 6667-6672.

111.   Schaak, R. E.; Sra, A. K.; Leonard, B. M.; Cable, R. E.; Bauer, J. C.; Han, Y.-F.; Means, J.; Teizer, W.; Vasquez, Y.; Funck, E. S., Metallurgy in a Beaker: Nanoparticle Toolkit for the Rapid Low-Temperature Solution Synthesis of Functional Multimetallic Solid-State Materials. *J. Am. Chem. Soc.* **2005,** *127*, 3506-3515.

112.   Cable, R. E.; Schaak, R. E., Low-Temperature Solution Synthesis of Nanocrystalline Binary Intermetallic Compounds Using the Polyol Process. *Chem. Mater.* **2005,** *17*, 6835-6841.

113.   Leonard, B. M.; Bhuvanesh, N. S. P.; Schaak, R. E., Low-temperature polyol synthesis of AuCuSn2 and AuNiSn2: Using solution chemistry to access ternary intermetallic compounds as nanocrystals. *J. Am. Chem. Soc.* **2005,** *127*, 7326-7327.

114.   Sra, A. K.; Ewers, T. D.; Schaak, R. E., Direct Solution Synthesis of Intermetallic AuCu and AuCu$_3$ Nanocrystals and Nanowire Networks. *Chem. Mater.* **2005,** *2005*, 758-766.

115.   Cable, R. E.; Schaak, R. E., Reacting the unreactive: A toolbox of low-temperature solution-mediated reactions for the facile interconversion of nanocrystalline intermetallic compounds. *J. Am. Chem. Soc.* **2006,** *128*, 9588-9589.

116.   Leonard, B. M.; Schaak, R. E., Multistep Solution-Mediated Formation of AuCuSn2: Mechanistic Insights for the Guided Design of Intermetallic Solid-State Materials and Complex Multimetal Nanocrystals. *J. Am. Chem. Soc.* **2006,** *128*, 11475-11482.

117.   Cable, R. E.; Schaak, R. E., Solution synthesis of nanocrystalline M-Zn (M = Pd, Au, Cu) intermetallic compounds via chemical conversion of metal nanoparticle precursors. *Chem. Mater.* **2007,** *19*, 4098-4104.

118.   Chou, N. H.; Schaak, R. E., Shape-Controlled Conversion of β-Sn Nanocrystals into Intermetallic M-Sn (M = Fe, Co, Ni, Pd) Nanocrystals. *J. Am. Chem. Soc.* **2007,** *129*, 7339-7345.

119.   Vazquez, Y.; Luo, Z.; Schaak, R. E., Low-Temperature Solution Synthesis of the Non-Equilibrium Ordered Intermetallic Compounds Au_3Fe, Au_3Co, and Au_3Ni as Nanocrystals. *J. Am. Chem. Soc.* **2008,** *130*, 11866-11867.

120.   Chou, N. H.; Schaak, R. E., A Library of Single-Crystal Metal-Tin Nanorods: Using Diffusion as a Tool for Controlling the Morphology of Intermetallic Nanocrystals. *Chem. Mater.* **2008,** *20*, 2081-2085.

121.   Leonard, B. M.; Anderson, M. E.; Oyler, K. D.; Phan, T.-H.; Schaak, R. E., Orthogonal Reactivity of Metal and Multimetal Nanostructures for Selective, Stepwise, and Spatially-Controlled Solid-State Modification. *ACS Nano* **2009,** *3*, 940-948.

122.   Bondi, J. F.; Misra, R.; Ke, X.; Sines, I. T.; Schiffer, P.; Schaak, R. E., Optimized Synthesis and Magnetic Properties of Intermetallic Au_3Fe_{1-x}, Au_3Co_{1-x}, and Au_3Ni_{1-x} Nanoparticles. *Chem. Mater.* **2010,** *22*, 3988-3994.

123.   Bradley, M. J.; Biacchi, A. J.; Schaak, R. E., Chemical Transformation of Pt-Fe3O4 Colloidal Hybrid Nanoparticles into $PtPb-Fe_3O_4$ and $Pt_3Sn-Fe_3O_4$ Heterodimers and $(PtPb-Fe_3O_4)$ n Nanoflowers. *Chem. Mater.* **2013,** *25*, 1886-1892.

124.   McEnaney, J. M.; Schaak, R. E., Solution Synthesis of Metal Silicide Nanoparticles. *Inorg. Chem.* **2015,** *54*, 707-709.

125.   Abe, H.; Matsumoto, F.; Alden, L. R.; Warren, S. C.; Abruña, H. D.; DiSalvo, F. J., Electrocatalytic Performance of Fuel Oxidation by Pt_3Ti Nanoparticles. *J. Am. Chem. Soc.* **2008,** *130*, 5452-5458.

126.   Saravanan, G.; Abe, H.; Xu, Y.; Sekido, N.; Hirata, H.; Matsumoto, S.; Yoshikawa, H.; Yamabe-Mitarai, Y., Pt_3Ti Nanoparticles: Fine Dispersion on SiO_2 Supports, Enhanced Catalytic CO Oxidation, and Chemical Stability at Elevated Temperatures. *Langmuir* **2010,** *26*, 11446-11451.

127.   Ramesh, G. V.; Kodiyath, R.; Tanabe, T.; Manikandan, M.; Fujita, T.; Umezawa, N.; Ueda, S.; Ishihara, S.; Ariga, K.; Abe, H., Stimulation of Electro-oxidation Catalysis by Bulk-Structural Transformation in Intermetallic $ZrPt_3$ Nanoparticles. *ACS Appl. Mater. Inter.* **2014,** *6*, 16124-16130.

128.   Cui, Z.; Chen, H.; Zhao, M.; Marshall, D.; Yu, Y.; Abruña, H. D.; DiSalvo, F. J., Synthesis of Structurally Ordered Pt_3Ti and Pt_3V Nanoparticles as Methanol Oxidation Catalysts. *J. Am. Chem. Soc.* **2014,** *136*, 10206-10209.

129.   Cui, Z.; Chen, H.; Zhou, W.; Zhao, M.; DiSalvo, F. J., Structurally Ordered Pt_3Cr as Oxygen Reduction Electrocatalyst: Ordering Control and Origin of Enhanced Stability. *Chem. Mater.* **2015,** *27*, 7538-7545.

130. Marakatti, V. S.; Sarma, S. C.; Joseph, B.; Banerjee, D.; Peter, S. C., Synthetically Tuned Atomic Ordering in PdCu Nanoparticles with Enhanced Catalytic Activity toward Solvent-Free Benzylamine Oxidation. *ACS Appl. Mater. Inter.* **2017,** *9*, 3602-3615.

131. Ota, A.; Armbruster, M.; Behrens, M.; Rosenthal, D.; Friedrich, M.; Kasatkin, I.; Girgsdies, F.; Zhang, W.; Wagner, R.; Schlogl, R., Intermetallic Compound Pd_2Ga as a Selective Catalyst for the Semi-Hydrogenation of Acetylene: From Model to High Performance Systems. *J. Phys. Chem. C* **2011,** *115*, 1368-1374.

132. Armbruster, M.; Wowsnick, G.; Friedrich, M.; Heggen, M.; Cardoso-Gil, R., Synthesis and Catalytic Properties of Nanoparticulate Intermetallic Ga-Pd Compounds. *J. Am. Chem. Soc.* **2011,** *133*, 9112-9118.

133. Chen, S.; Jenkins, S. V.; Tao, J.; Zhu, Y.; Chen, J., Anisotropic Seeded Growth of Cu–M (M = Au, Pt, or Pd) Bimetallic Nanorods with Tunable Optical and Catalytic Properties. *J. Phys. Chem. C* **2013,** *117*, 8924-8932.

134. Li, C.; Chen, Y.; Zhang, S.; Xu, S.; Zhou, J.; Wang, F.; Wei, M.; Evans, D. G.; Duan, X., Ni–In Intermetallic Nanocrystals as Efficient Catalysts toward Unsaturated Aldehydes Hydrogenation. *Chem. Mater.* **2013,** *25*, 3888-3896.

135. Zhou, J.; Yang, Y.; Li, C.; Zhang, S.; Chen, Y.; Shi, S.; Wei, M., Synthesis of Co–Sn intermetallic nanocatalysts toward selective hydrogenation of citral. *J. Mater. Chem. A* **2016,** *4*, 12825-12832.

136. Li, C.; Chen, Y.; Zhang, S.; Zhou, J.; Wang, F.; He, S.; Wei, M.; Evans, D. G.; Duan, X., Nickel–Gallium Intermetallic Nanocrystal Catalysts in the Semihydrogenation of Phenylacetylene. *ChemCatChem* **2014,** *6*, 824-831.

137. Feng, Q.; Zhao, S.; Wang, Y.; Dong, J.; Chen, W.; He, D.; Wang, D.; Yang, J.; Zhu, Y.; Zhu, H.; Gu, L.; Li, Z.; Liu, Y.; Yu, R.; Li, J.; Li, Y., Isolated Single-Atom Pd Sites in Intermetallic Nanostructures: High Catalytic Selectivity for Semihydrogenation of Alkynes. *J. Am. Chem. Soc.* **2017,** *139*, 7294-7301.

138. Marakatti, V. S.; Arora, N.; Rai, S.; Sarma, S. C.; Peter, S. C., Understanding the Role of Atomic Ordering in the Crystal Structures of Ni_xSn_y toward Efficient Vapor Phase Furfural Hydrogenation. *ACS Sustain. Chem. Eng.* **2018,** *6*, 7325-7338.

139. Kim, D.; Xie, C.; Becknell, N.; Yu, Y.; Karamad, M.; Chan, K.; Crumlin, E. J.; Norskov, J. K.; Yang, P., Electrochemical Activation of CO2 through Atomic Ordering Transformations of AuCu Nanoparticles. *J. Am. Chem. Soc.* **2017,** *139*, 8329-8336.

Chapter 2

Strain-Enhanced Metallic Intermixing in Shape-Controlled Multilayered Core-Shell Nanostructures: Toward Shaped Intermetallics
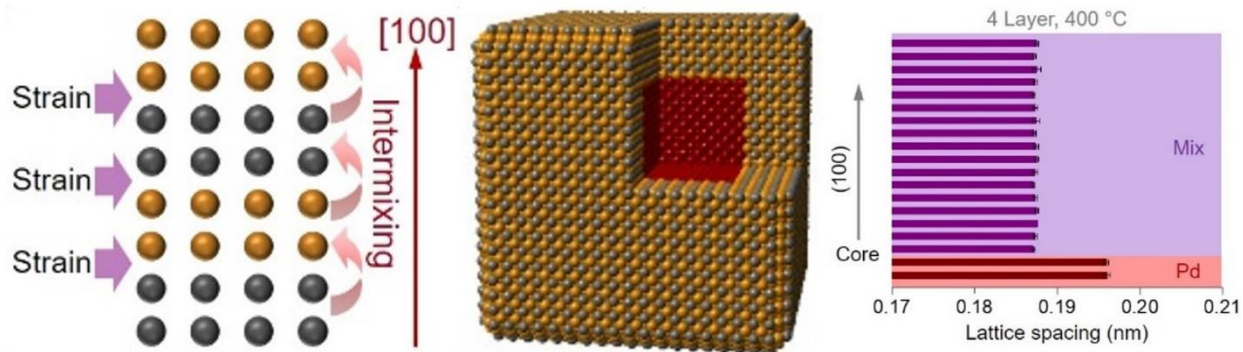
2.1 Abstract

Controlling the surface composition of shaped bimetallic nanoparticles could offer precise tunability of geometric and electronic surface structure for new nanocatalysts. To achieve this goal, we design a platform for studying the intermixing process in a shaped nanoparticle, using multilayered Pd-Ni-Pt core-shell nanocubes as precursors. We find that, under mild conditions, the intermixing between Ni and Pt could be tuned by changing layer thickness and number, triggering intermixing while preserving nanoparticle shape. Intermixing of the two metals is monitored using transmission electron microscopy. DFT calculations suggest that the low-temperature mixing is enhanced by shorter diffusion lengths and strain introduced by the layered structure. The platform and insights presented here represent an advance toward the realization of shape-controlled multimetallic nanoparticles tailored to each potential application.

2.2 Introduction

Nanomaterial design has increasingly focused on developing highly active and stable catalysts for chemical transformations.[1-9] Platinum group metals are particularly active for a diverse set of reactions, but they are expensive and susceptible to surface poisoning. By incorporating nonprecious metals, catalyst cost can be lowered and performance can be improved.[10-16] The degree of intermixing between the metals has recently been shown to dramatically affect catalyst performance, but the mechanism of mixing is not well understood.[2, 17-18] Thus, we aim to study the intermixing process and clarify its effect on catalysis.

Among alloys, the compositions that form intermetallic compounds (IMCs) have attracted recent attention because, in these cases, intermixing is thermodynamically favored and surface structure is well-defined.[19-21] Generally, IMCs are crystalline alloys composed of two or more metallic/metalloid elements with specific stoichiometry and long-range order. More robust and

resilient to etching,[22-24] these atomically ordered structures offer unique properties, including shape-memory,[25-26] hydrogen storage,[27-28] and superconductivity.[29-31]

Further, their tunable surface electronic structures[19-21] allow their adsorption and desorption properties to be tailored to specific chemical reactions. In previous work, bulk IMCs have been extensively studied.[32-34] More recent studies have focused on IMC nanoparticles (NPs) for their tailorable geometries, electronic surface structures and molecular adsorption properties.[35-43] The kinetics of solid-state intermixing to form IMCs, however, has received little attention.

We note three approaches to the formation of IMC NPs.[38, 44] The first is a top-down synthesis method, where particles are formed by the mechanical alloying of mixed metallic powders through ball milling and annealing to form IMC phases.[43] The size and shape of particles synthesized by these methods cannot be controlled, and no information can be gained on the nanoscale intermixing process. The second is direct, bottom-up synthesis by wet-chemistry methods. Shaped IMC NPs have been generated using this method,[45-46] but the need to precisely and simultaneously control the deposition rates of the chosen metals makes extending their scope and understanding their formation kinetics challenging. The third reported strategy involves synthesizing alloyed or heterostructured bimetallic NPs (e.g. core-shell or dimer) by wet-chemistry and then converting these NPs to the intermetallic phase through intermixing triggered by thermal annealing at high temperatures.[47] While promising, intermixing under these harsh conditions degrades the NP, generally through sintering and reshaping, preventing the study of intermixing in a specific geometry. The resulting indistinct particle shapes can further convolute catalytic results due to inconsistencies in size, shape/faceting, and surface composition, making the fundamental study of the catalyst surface or active sites difficult. In this work, we aim to optimize this third approach because we believe that intermixing, taking place in well-controlled nanoscale

geometries, offers the best opportunity to understand the shape-dependent formation kinetics of IMC phases, which could, in turn, lead to a general synthesis scheme for shaped IMC NPs.
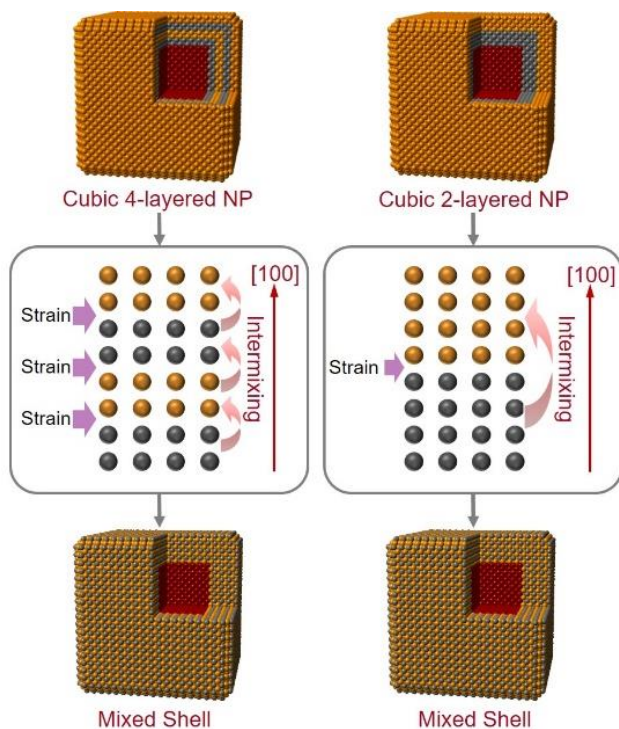
Figure 2.1 Schematic representation of the conversion process to mixed shell structures through atomic diffusion.

Since the solid-solid inter-diffusion of metal atoms to form ordered intermetallic structures is the greatest contributor to the need for high annealing temperatures,[48-50] we focus on lowering the effective diffusion barriers, which we hypothesize can be reduced by the use of strained metallic layers of reduced thickness. Moreover, varying the layer thickness could allow us to test the effect of these variables on metallic mixing. Structures with a higher number of thinner layers (and thus higher strain and shorter diffusion lengths), we hypothesize, should show mixing at lower temperature than those with fewer, thicker layers. Previously, our group developed defined

overgrowth methods for well-controlled core-shell NPs using mild aqueous phase systems.[12-13, 51] During these syntheses, variables such as substrate size and shape, layer thickness and compositions, and layer number could be controlled. Notably, our Pd-Ni-Pt system[13] stands out as an interesting candidate for the study of intermetallic formation, as the incorporation of Ni into Pt NPs has been shown to increase catalytic activity towards small molecule redox reactions.[11, 47, 52-53] This well-defined platform serves as an ideal arena to study intermetallic formation, because this controlled, layered structure allows for a simple mixing process that can be easily characterized compared to other systems, such as alloy nanoparticles (Figure 2.1). The Pt-Ni system offers several advantages. The fcc nature of Ni, Pt, and the mixed Pt_3Ni and $PtNi_3$ phases simplifies the analysis of mixing. Further, Pt-Ni intermetallics have shown catalytic activity that is dependent on surface faceting, which will allow us to use catalysis as a probe of surface structure.[54]

2.3 Characterization of Pd-Ni-Pt and Pd-(Ni-Pt)$_2$

Herein, we focus on the $PtNi_3$ system as it has the highest loading of the nonprecious metal, Ni, relative to the precious metal, Pt. To maintain a bimetallic and more easily studied system, the core particle used to direct the shape of the NPs should be inert to the layer above it. For this reason, the Pd core was chosen; Pd and Ni are not known to form stable IMC phases under mild annealing temperatures. We have performed DFT analysis to support this hypothesis, which will be discussed in detail below. Further, our experimental results show that the outer shell maintains a consistent thickness despite annealing, indicating limited diffusion between the core and shell. By intermixing the multilayered shell of defined core-shell structures, we can begin to construct a set of design parameters to be extended to other IMC NP structures of various shapes and compositions.
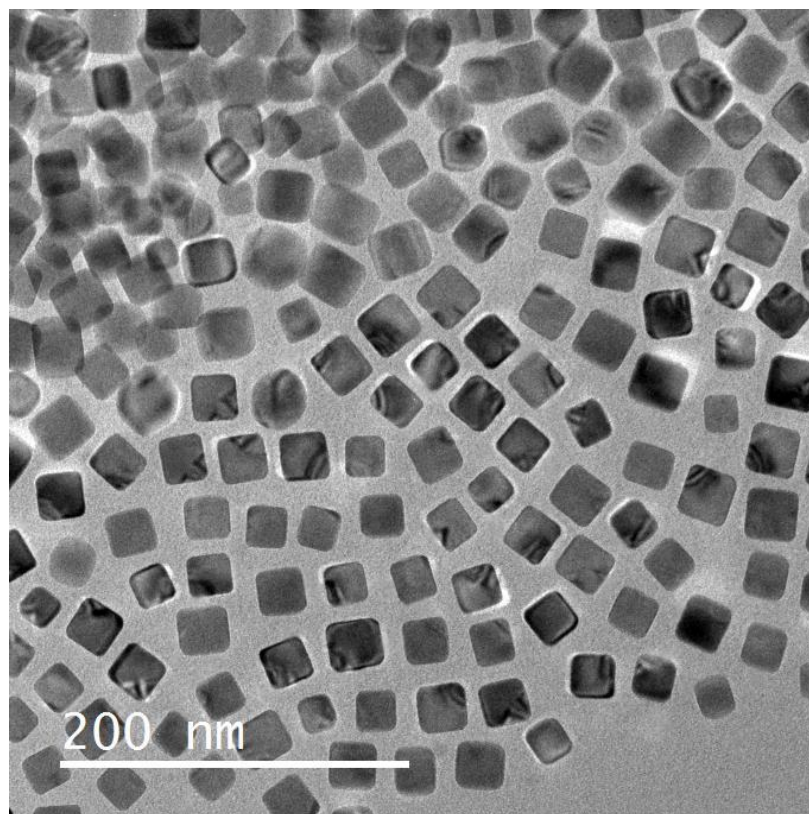
Figure 2.2 TEM images of Pd nanocubes used as substrates for layered overgrowth.

Figure 2.2 shows transmission electron microscopy (TEM) images of the cubic Pd NPs used for the core of the layered structure. They are found to be ~30 nm in edge length. Representative (TEM) images of the Pd-Ni-Pt (a and c) and the Pd-$(Ni-Pt)_2$ (b and d) core-multilayered shell NP precursors can be seen in Figure 2.2. Synthesis details are outlined in the Materials and Methods section. Mapping by energy dispersive x-ray spectroscopy (EDX) clearly shows Pd located in the core cube with Ni and Pt layered in the shell. Each layer shows epitaxial overgrowth, even with the high interfacial energy and strain associated with the metal boundary between the highly mismatched (~10%) lattices of Ni and Pt. This induced strain should contribute

to a lower effective diffusion barrier facilitating metal-metal migration, particularly through the open (100) facet (which dominates the surface of our cubic NPs). Calculations for the expected thickness of the metallic layers were performed based on atomic ratios, obtained through inductively coupled plasma optical emission spectroscopy (ICP-OES, Table 2.1).
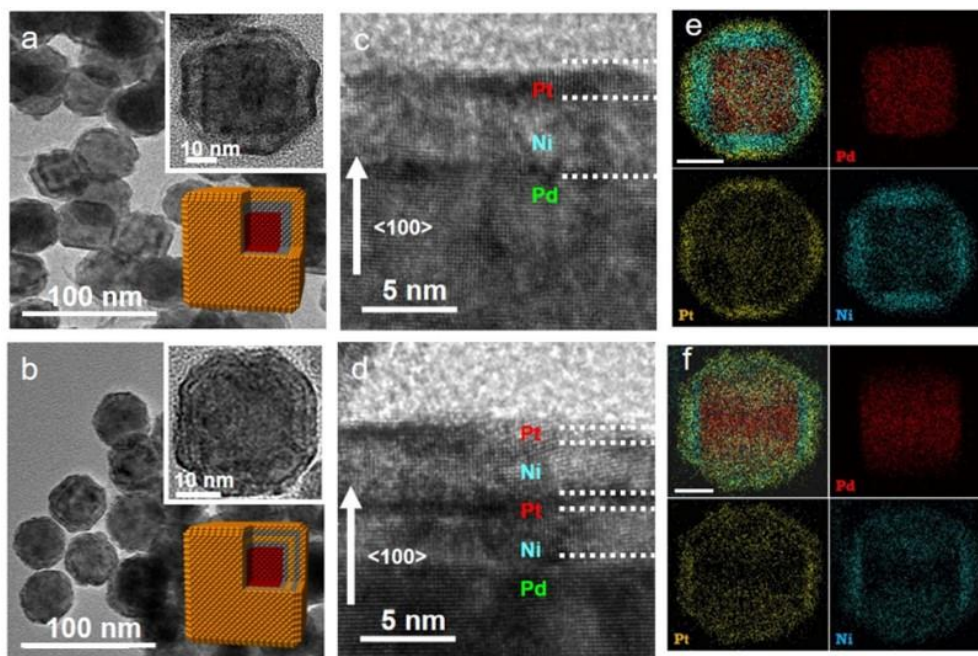
Figure 2.3 Transmission electron microscopy images of the as-synthesized nanoparticles. (a) Pd-Ni-Pt samples at low magnification with the inset showing a single precursor particle and (b) Pd-(Ni-Pt)$_2$ samples at low magnification with the inset showing a single precursor particle. (c and d) High magnification images of the Pd-Ni-Pt and Pd-(Ni-Pt)$_2$ particles, respectively, with the lighter Ni phase "sandwiched" between the darker Pd and Pt phases. (e and f) Energy dispersive x-ray mapping of the Pd, Ni, and Pt phases showing the Pd core and Ni and Pt surface layers; scale bars are 10 nm.

Sample	Ni	Pt
Pd-Ni-Pt	3.2	1.0
Pd-(Ni-Pt)$_2$	2.6	1.0

Table 2.1 Ni:Pt molar ratios calculated form ICP-OES analysis. For Pd-(Ni-Pt)$_2$, the Ni and Pt content are a combination of alternating sandwich layers.

By TEM, the base Pd cube is found to be ~30 nm in edge length and the final layered structure, either two- or four-layered, is ~35 nm in edge length. Lattice constants of 352.4 pm and 392.42 pm were used for Ni and Pt, respectively. For the Pd-Ni-Pt particles, layers of 3.6 nm and 1.4 nm were found respectively for the Ni and Pt (3.52 and 1.43 were measured by TEM). The calculation for the four-layered particles assumed that both shell layers were of equivalent thickness for each metal. Based on this assumption, thicknesses of 1.7 nm and 0.8 nm (1.78 nm and 0.77 nm were measured by TEM) were found for Ni and Pt, respectively. These values are close to target value of 3:1 and the expected values from the nominal concentration loading.
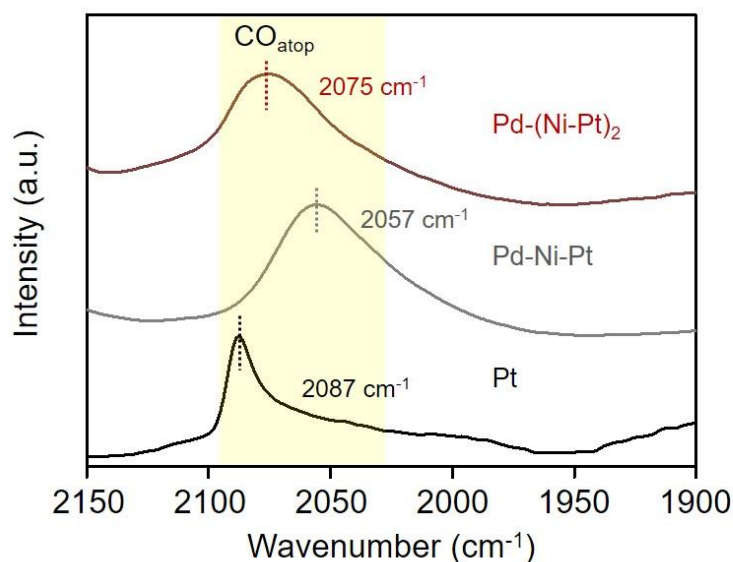
Figure 2.4 Normalized Pd-(Ni-Pt)$_x$ CO-DRIFTS spectra showing a shift in the energy of the characteristic C-O stretching peak. A larger shift in energy is seen for the thicker-layered Pd-Ni-Pt than the thinner-layered Pd-(Ni-Pt)$_2$.

To test the surface electronic structures of these two samples, we carried out diffuse reflectance infrared spectroscopy using adsorbed CO (CO-DRIFTS) (Figure 2.4).[55-56] In each case, the NPs are supported on SiO$_2$. For pure Pt NPs, a characteristic C-O stretch is seen around 2087 cm^{-1}, corresponding to CO adsorbed atop a Pt atom.[57-58] When the thicker Ni layer is introduced below the Pt surface (Pd-Ni-Pt), a large shift in the C-O peak to 2057 cm^{-1} is observed. This shift indicates that the Ni layer has indeed significantly impacted the surface Pt layer. With the thinner, alternating Ni and Pt layers (Pd-(Ni-Pt)$_2$), the peak shifts to 2075 cm^{-1}. This shift clearly indicates that the two layer thicknesses impact the surface differently, but it is challenging to interpret the trend in the shifts, which depends largely on two factors: the ligand effect and lattice strain. In the first case, Ni has a Fermi level energy of 9.46 eV while the Fermi level of Pt sits at 8.79 eV.[59] As

such, charge is transferred from the inner Ni layer to the outer Pt layer, shifting the C-O stretch frequency.[60] In the latter case, introduced strain from Ni is compressive, due to its compact lattice, which increases orbital overlap and again shifts the C-O stretch frequency. A fundamental understanding of these two processes suggests that both should cause the d-band center to shift in the same direction (to lower energy). It is thus not straightforward to explain how these two factors lead to the observed shifts. As such, we simply claim that the shift in the DRIFTS peak suggests that the layered structures have introduced structural differences.

2.4 TEM Analysis of Metallic Intermixing

Mixing of the layered structures was performed by drying the NPs on a carbon substrate and annealing them in a tube furnace under nitrogen. More details can be found in the Materials and Methods section. The surface of the mixed NPs generally retains its parent faceting and remains single crystalline (Figure 2.5). To more quantitatively track the degree of mixing for each temperature, high-resolution TEM (HRTEM) images were taken to study the change in lattice parameter through the different layers of the NP (Figure 2.6). Additionally, an ordered pattern associated with IMC can be seen in some parts of the particle in Figure 2.6(a), corresponding to the $L1_2$ crystal structure adopted by $PtNi_3$ with bright Pt atoms on the corners and darker Ni atoms on the six faces of the cubic structure. The few atomic layers directly below the NP surface, however, seem to show consistent brightness, which we attribute to fcc Pt and suggests mixing has not progressed throughout the entire shell layer. A Ni:Pt ratio of 3:1 further agrees well with our initial precursor concentrations and ICP-OES analysis. For the $Pd-(Ni-Pt)_2$ system, the image shown is taken from the [110] direction. From that perspective, the shell shows the $L1_2$ crystal structure layers of contrasting brightness. This pattern indicates intermixing and formation of the IMC phase.
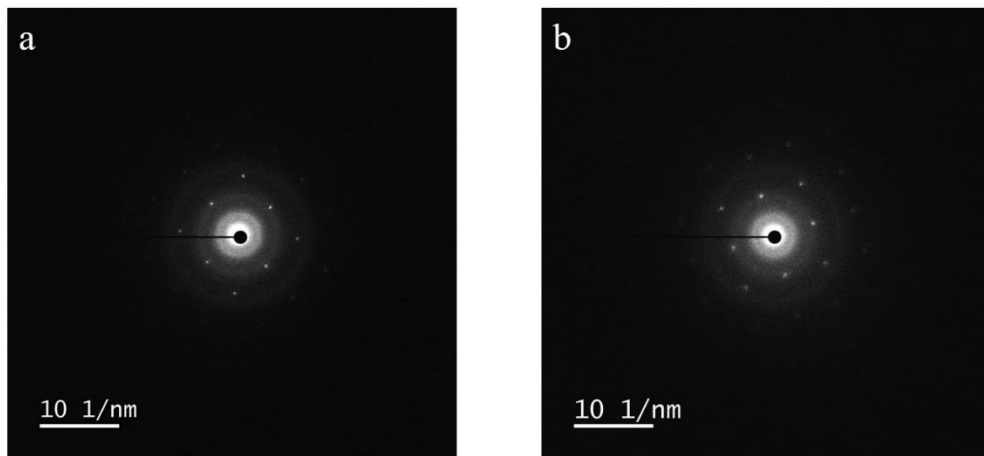
Figure 2.5 Representative Pd-(Ni-Pt)$_x$ selected area electron diffraction images of (a) Pd-Ni-Pt and (b) Pd-(Ni-Pt)$_2$ after calcination, reinforcing their single-crystallinity.
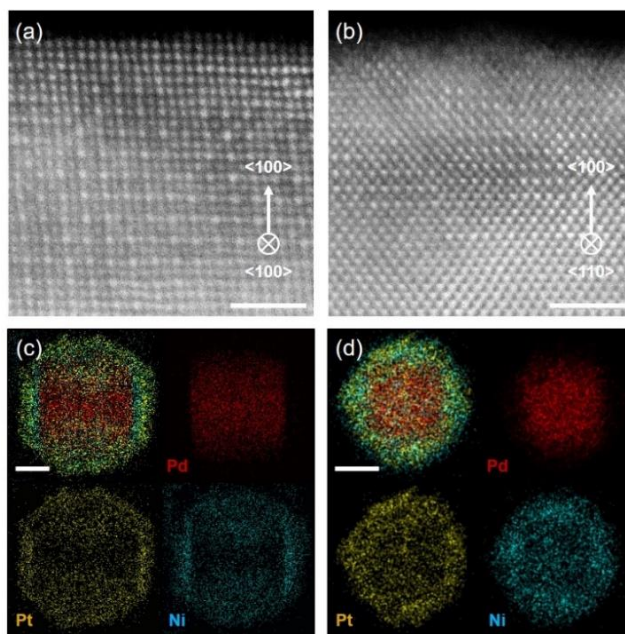

Figure 2.6 Representative high-resolution TEM images of (a) Pd-Ni-Pt and (b) Pd-(Ni-Pt)$_2$ after annealing at 400 °C. Energy dispersive x-ray images of Pd-(Ni-Pt)$_2$ (c) before and (d) after

annealing, showing the core Pd cube and the mixing of the outer layers. Scale bars are 10 nm. Scale bars are 2 nm.

For a more systematic understanding of the intermixing process, we have analyzed the lattice spacings of several (>10) particles at each annealing temperature, with the results summarized in Figure 2.7. For pristine Pd, Ni, and Pt, the d-spacing measurements in the [200] direction are 0.1945 nm, 0.1760 nm, 0.1960 nm, respectively. With the migration of the metal atoms, the lattice spacing is expected to change due to the different lattice constants. The larger Pt lattice will compress due to epitaxy with and incorporation of Ni while Ni will expand. Once completely mixed and stable, the lattice measurements throughout the mixed shell should be the same. For the ideal $PtNi_3$ phase, the lattice spacing in the [200] direction is ~0.1875 nm. We chose this composition based on the initial precursor concentrations of 3:1 Ni:Pt. The ICP-OES data presented in Table 2.1 reinforces this ratio of Ni to Pt in the synthesized NPs. Figure 2.7 shows a graphical representation of the changes in the lattice parameters from the Pt shell down to the Pd core. It should be noted that, due to thinner metallic layers in the $Pd-(Ni-Pt)_2$ system, both Pd-Ni-Pt and $Pd-(Ni-Pt)_2$ NPs have similar overall size, so we do not believe particle size is a contributing factor in mixing. At 200 °C a clear difference can be seen between the mixing in the two structures. The four-layered, strained structure shows mixing initiated at the Ni/Pt interfaces, while clear, separated Ni and Pt layers are seen in the two-layered structure. At 300 °C, the four-layered structure begins to approach full mixing and the two-layered shows the beginning of it at the Ni/Pt interface. At 400 °C, the shell of $Pd-(Ni-Pt)_2$ is fully mixed, while Ni and Pt layers are still visible in Pd-Ni-Pt. Overall, this analysis reinforces our idea that reduced diffusion lengths and increased strain in $Pd-(Ni-Pt)_2$ allow for mixing at lower temperatures.
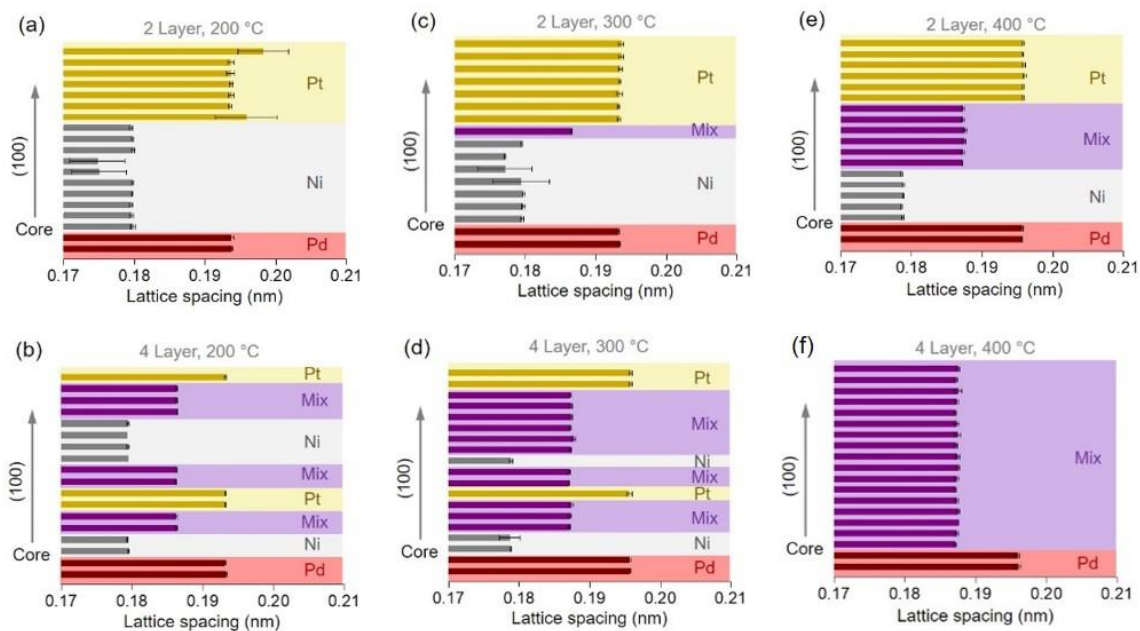
Figure 2.7 Lattice spacing measurement of Pd (red), Ni (grey), Pt (gold), and intermixed layered (purple) NPs. The intermixing is more pronounced at lower annealing temperatures for four-layered samples compared to the two-layered sample.

These quantitative data agree well with our post-annealing characterization by EDX (Figure 2.6). Full mixing can be seen throughout the outer shell layers of the Pd-(Ni-Pt)$_2$ NPs after annealing at 400 °C. Similarly complete mixing of Pd-Ni-Pt requires annealing at 500 °C, which induces some surface reshaping (Figure 2.8), reinforcing the benefits of the several thin layers in the Pd-(Ni-Pt)$_2$ structure. Importantly, the Pd cube is clearly visible in the core of the mixed particle. This supports our hypothesis that Pd will not migrate into the shell layers at the mild temperatures chosen for our annealing.
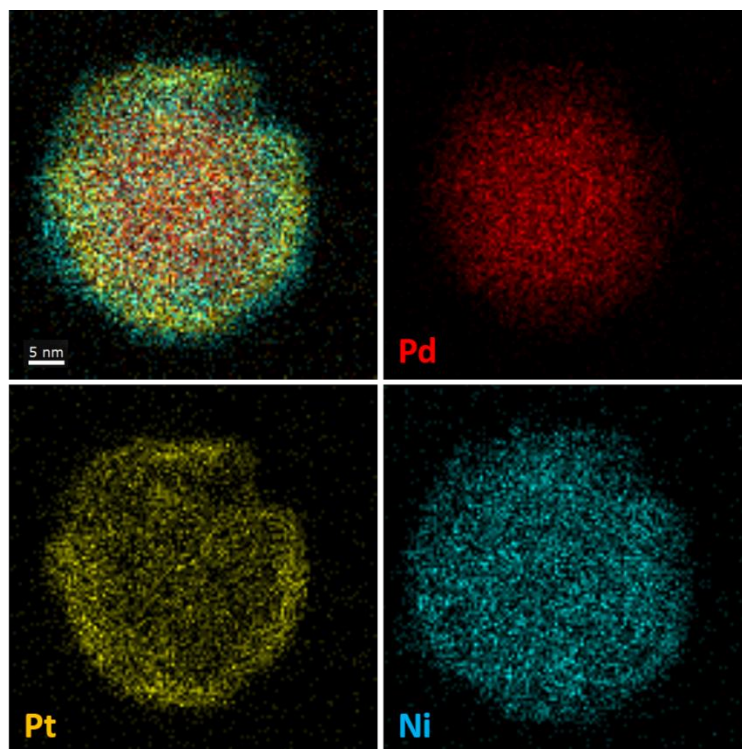
Figure 2.8 EDX analysis of the Pd-Ni-Pt NP after annealing at 500 °C showing the mixed outer shell and some surface deformation.

We have also carried out x-ray diffraction (XRD) (Figure 2.9). The information on intermixing gained from XRD analysis is limited in our system due to the thinness of the shell layers. The Pd cores dominate the majority of the XRD spectrum. We are, therefore, unable to observe the emergence of a peaks corresponding to the $PtNi_3$ phase, though we do see a disappearance of the characteristic Ni peak upon annealing. Clear peaks are seen for both Pd-Ni-Pt and Pd-$(Ni-Pt)_2$ NPs around 40° and 47°, attributed to the Pd and Pt in the sample but likely dominated by the Pd cube. A peak around 44.5° can be seen for the thicker Ni layer in the Pd-Ni-Pt NPs, which is attributed to the [111] reflection of Ni. After annealing of the Pd-$(Ni-Pt)_2$ NPs, no new peaks are seen, although the peak for the [111] Ni reflection is fully attenuated. The

broadness of the peaks is likely due to the thinness of their layers, per the Scherrer effect. All attributions are based on data from the Inorganic Crystal Structure Database.
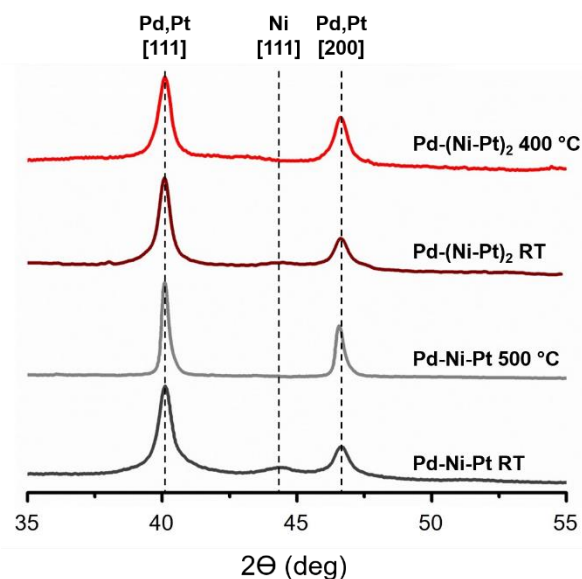
Figure 2.9 XRD analysis of Pd-Ni-Pt and Pd-(Ni-Pt)$_2$ before and after annealing at relevant full-mixing temperatures.

2.5 Theoretical Analysis of Metallic Mixing

Next, we discuss theoretical insights into energetics relevant to this lower-temperature intermixing in this system using Density Functional Theory (DFT) analysis contributed by our collaborators Prof. James W. Evans and Dr. Yong Han. A detailed description of the DFT analysis is provided in the materials and methods section. An overview is given here. As a preliminary analysis, using the PBEsol functional, the results support our hypothesis that intermixing of Ni and Pt to form Ni$_3$Pt is thermodynamically favored by 0.27 eV (per 3 Ni + 1 Pt), but intermixing of Ni and Pd to for Ni$_3$Pd is disfavored by 0.13 eV (per 3 Ni + 1 Pd). We have also checked that

intermixing of Ni with Pt is favored, and with Pd is disfavored, for other stoichiometries. Regarding the kinetics of intermixing, we first performed a benchmark analysis for the vacancy-mediated diffusion of Ni in bulk Pt. Here, a vacancy diffuses through Pt to a site adjacent to the Ni impurity, thereby allowing Ni to hop to that adjacent site. The effective barrier, E_{eff}, for such a process is the sum of a barrier for an atom hopping into an adjacent vacancy, E_{dv}, and a formation energy for creating the vacancy, E_{fv}.[61] Nuances are described below and in previous work.[62] Here, we only report results from the PBEsol functional, which has been shown to be reliable for vacancy diffusion.[63] For the diffusion of Ni in Pt, the barrier for the Ni impurity to hop into an adjacent vacancy is found to be $E_{dv} = 0.93$ eV (versus $E_{dv} = 1.4$ eV for a Pt atom to hop into an adjacent vacancy in Pt). Thus, diffusion of the vacancy through Pt to reach a site adjacent to the Ni impurity (rather than the hopping of Ni into the vacancy) is the rate-controlling step. Consequently, the higher $E_{dv} = 1.4$ eV determines E_{eff}. The formation energy for a vacancy next to a Ni impurity in Pt is $E_{fv} = 0.94$ eV (versus $E_{fv} = 0.84$ eV for formation of a vacancy in pure Pt), and the former higher value determines E_{eff}. However, DFT underestimates E_{fv} due to so-called "surface intrinsic error", so, guided by previous analysis for pure Pt,[61] we use $E_{fv} = 1.2$ eV (rather than 0.94 eV) to obtain $E_{eff} \approx 1.4 + 1.2 = 2.6$ eV for Ni diffusion in Pt. The corresponding effective rate for hopping of the Ni impurity, assuming an Arrhenius form with a typical prefactor of 10^{13}/s is about $10^{-6.5}$/s at 400 °C, too low for effective intermixing on the experimental timescale.

However, motivated by the proposed importance of strain effects in intermixing, we consider the effect of compressive Pt strain, $\varepsilon < 0$, on E_{fv}, and E_{dv}. (Recall that epitaxy at the Ni-Pt interface within the NP, as well as Ni incorporation into Pt, should induce compressive strain.) Significantly, we find a strong decrease in the vacancy formation energy, E_{fv}, with increasing strain magnitude, $|\varepsilon|$, for triaxial strain, and, in fact, E_{fv} vanishes when $|\varepsilon|$ increases to only 2% (Figure

2.10). A weaker decrease occurs for biaxial strain. On the other hand, E_{dv} increases with $|\varepsilon|$ to 1.2 eV (1.7 eV) for Ni (Pt) hopping into a vacancy where $|\varepsilon| = 2\%$ for triaxial strain (with a lesser increase for biaxial strain). Assuming that compressive strain makes E_{fv} negligible, then $E_{eff} \approx E_{dv} \approx 1.7$ eV. Then, the effective hop rate for the Ni impurity is about 2/s at 400 °C, which is sufficiently high for effective intermixing.
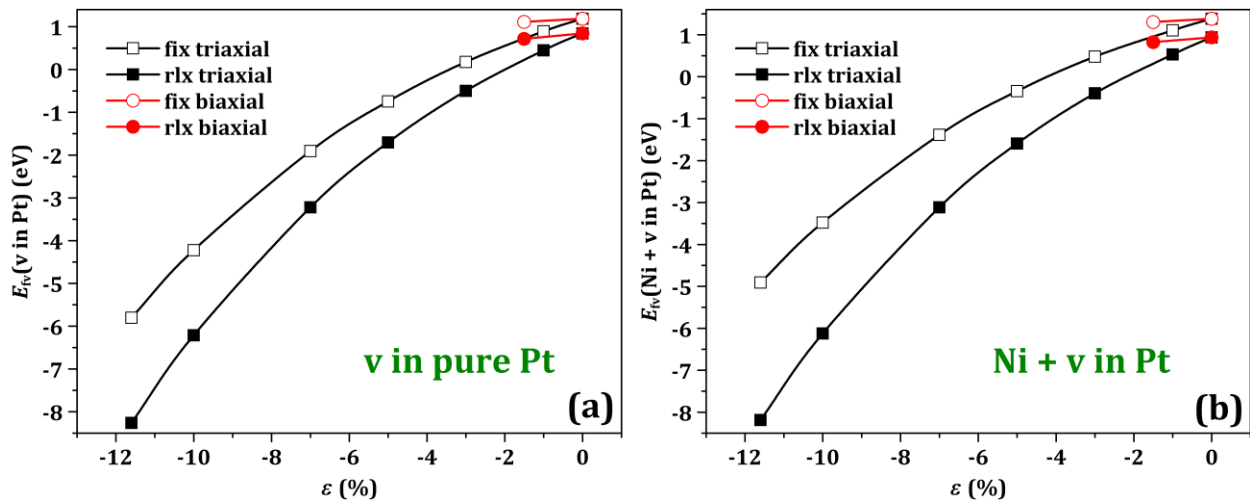
Figure 2.10 Vacancy formation energies in fcc Pt. (a) E_{fv}(v in Pt) and (b) E_{fv}(Ni+v in Pt) versus (compressive) strain ε from our PBEsol calculations.

Second, we briefly consider the vacancy-mediated diffusion of Pt in bulk Ni (Figure 2.11). PBEsol predicts that $E_{dv} = 1.4$ eV (1.2 eV) for a Pt (Ni) atom to hop into an adjacent vacancy in Ni. PBEsol also predicts that $E_{fv} = 1.5$ eV for vacancy formation next to a Pt impurity in Ni and $E_{fv} = 1.6$ eV in pure Ni (which might be increased by ~0.2 eV accounting for surface intrinsic error). Thus, we conclude that $E_{eff} \approx 1.4 + 1.8 = 3.2$ eV, too high for this intermixing process to be effective. Additional studies to explore the effect of tensile strain on Ni (induced by epitaxy at the

Ni-Pt interfaces and Pt incorporation in Ni) reveal that E_{fv} actually increases with strain (at least up to ~6%). Although E_{dv} increases somewhat, there is no net decrease in E_{eff}. Thus, we conclude that intermixing in the Ni-Pt system is asymmetric and associated with strain-enhanced diffusion of Ni into Pt, rather than by Pt diffusion into Ni.
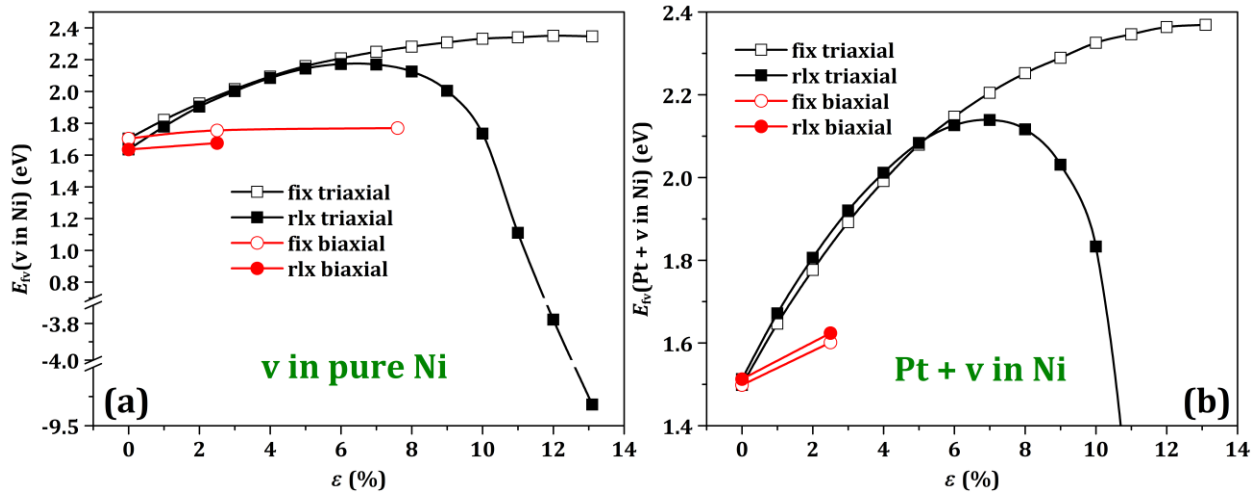
Figure 2.11 Vacancy formation energies in fcc Ni. (a) E_{fv}(v in Ni) and (b) E_{fv}(Pt+v in Ni) versus ε from our PBEsol calculations.

In sum, the theoretical analysis suggests that the mixing process is largely one-directional, with Ni diffusing into Pt to form the mixed outer shell structure. It also suggests that strain plays a crucial role in the fundamental energetics of mixing. The compressive strain introduced into the Pt layer by the subsurface Ni reduces the barrier to vacancy formation, allowing mixing to occur at temperatures lower than for the two bulk metals. This reduced mixing temperature is fundamental to the platform introduced here, which seeks to induce mixing at annealing temperatures that preserve nanoparticle shape.

2.6 Conclusion

In conclusion, we have used a variety of techniques to investigate metallic mixing on the nanoscale. Through TEM and HRTEM analysis, we have shown that atomic diffusion is dependent on the thickness of the layers that make up the mixing metals. Through CO-DRIFTS, we have shown that our shell layers increase strain on the outer Pt surface, which DFT calculations suggest is essential for low-temperature metallic mixing. Overall, the insight gained represents an important step toward the development of shape-controlled bimetallic and IMC NPs. In the future, our platform can be extended to more exotic crystal structures beyond the *fcc*, d-block metals presented here, with an eye toward the ultimate goal of generating a set of design rules for the synthesis of nanocatalysts with custom-made geometric and electronic surface structure. The impact of the identified nanoscale mixing and resulting surface structure will be discussed in detail in Chapter 4.

Materials and Methods

Materials

Nickel (II) chloride hexahydrate (NiCl$_2$·6H$_2$O), potassium tetrachloroplatinate (II) (K$_2$PtCl$_4$), palladium (II) chloride (PdCl$_2$), L-ascorbic acid (AA, 99%), sodium iodide (NaI, 99.5%), and potassium hydroxide (KOH) were all obtained from Sigma-Aldrich Co., LLC. Hydrazine monohydrate (N$_2$H$_4$·H$_2$O, 98%) was purchased from Alfa Aesar. Cetyltrimethylammonium bromide (CTAB, 99%) was bought from Calbiochem. Ammonia borane (AB, 95%) was obtained from GFS Organic Chemicals and methanol (CH$_3$OH, 99.8%) was purchased through Acros Organics. Ultrapure distilled and deionized water (18.2 MΩ) was utilized in all experiments.

Nitrogen gas (N_2, UHP300) was obtained from Airgas. All reagents were used as received unless otherwise stated.

Synthesis

Pd-Ni-Pt Cubes: Cubic Pd substrates (~30 nm) were prepared according to our previous work[64]. 0.05 g of CTAB was dissolved in 10 mL of DI water *via* sonication in a 20 mL glass vial. 500 µL of a concentrated Pd nanocube solution (containing Pd cubes from eight reactions, redispersed in 5 mL of water) was added to the vial, which was gently swirled. 300 µL of 0.01 M $NiCl_2$ were added as Ni^{2+} ion source and 500 µL of 1.0 M hydrazine were added as reducing agent. The vial was swirled, capped, and left unstirred for ~2 h in an oil bath set to 50 °C. The appearance of small particulates in the reaction solution indicated completed overgrowth. The vial was then removed from the bath and briefly sonicated. 100 µL of 0.01 M K_2PtCl_4 were added as Pt^{2+} ion source. The solution was returned to the oil bath, still at 50 °C, and left unstirred for ~30 min. The Pd-Ni-Pt nanoparticles were collected *via* centrifugation at 4000 rpm and washed three times with water.

Pd-(Ni-Pt)₂ Cubes: To create the Pd-(Ni-Pt)₂ samples, the initial amount of Ni precursor added was 150 µL and that of Pt was 50 µL. Prior to centrifugation, the same procedure was performed as was used to reduce down the layer of Ni and subsequent layer of Pt. These samples were then collected *via* centrifugation at 4000 rpm and washed three times with water.

Deposition of Nanoparticles on Vulcan Carbon Support. 3.25 mg of carbon was added to the collected nanoparticles dispersed in ~1 mL of DI water. The carbon and nanoparticle mixture was sonicated for about 5 min. Sonicating for longer led induced carbon coverage of the nanoparticle surface, decreasing catalytic surface area. The vial was then capped with a rubber septum and moved to an oil bath at 90 °C. The particles were dried overnight under nitrogen flow and removed

from the oil bath. The same method was used to form both nanoparticle/carbon composites (Pd-Ni-Pt/C and Pd-(Ni-Pt)$_2$/C).

Annealing of Pd-(Ni-Pt)$_x$/C. The dried samples were added to a porcelain boat and calcined in a Lindberg/Blue M TF55030A-1 tube furnace at a ramp rate of 5 °C/min under nitrogen flow. Once to temperature (200-600 °C), the samples were held at the constant temperature for 1 h then allowed to cool immediately.

Characterization

Transmission Electron Microscopy: For analysis by transmission electron microscopy (TEM), the samples were washed three times in water by centrifugation at 4,000 rotations per minute. Once washed three times, the samples were concentrated to ~500 μL. From this solution, 10 μL was dropcast directly onto a carbon-coated copper grid (Ted Pella Inc., Formvar/Carbon 200 mesh, Cu); for the calcined samples, they were dropcast onto silicon oxide-coated gold grids (SPI Supplies, holey silicon oxide, Au). TEM characterization was run using a JEOL JEM2010F accompanied with EDX attachment operated at 200 kV.

X-Ray Diffraction: For analysis by XRD, particles were concentrated in 20 μL of ink solution then dropped on a thin glass slide and allowed to dry; for the calcined samples, a silicon chip was used as the substrate. A Bruker AXS D2 Phaser diffractometer was used for the XRD characterization.

Inductively Coupled Plasma-Optical Emission Spectroscopy: Analysis by ICP-OES measurements were performed by the following. Multi-element standard solutions for ICP-OES of 100 μg/mL of Pt, Pd, and other elements were purchased from Inorganic Ventures. Trace metal grade 70 % (w/w) nitric acid, 37 % (w/w) hydrochloric acid, and 49 % (w/w) hydrofluoric acid

were purchased from Fisher Scientific. ICP-OES data were acquired using an Agilent 5100 VDV spectrometer equipped with an HF-resistant sample introduction system. Concentrations were determined by external calibration with three points for ca. 1, 10, and 100 μg/mL of each element. Multi-element standard solutions of 100 μg/mL of Pt, Pd, and other elements in a 4.3 %(w/w) HCl matrix were used to prepare the 10 and 1 μg/mL standards volumetrically by dilution with identical matrices.

Detailed Description of DFT Analysis

Section 1. DFT Benchmarking and Bulk Alloy Thermodynamics

DFT calculations are performed by using the Vienna Ab Initio Simulation Package (VASP)[65]. For the electron-core interactions, we use the projector-augmented-wave (PAW) pseudopotentials[66], which were generated and released in 2013 by the VASP group. For Ni, Pt, and Pd metals as well as their alloys, we use Perdew-Burke-Ernzerhof (PBE) generalized-gradient approximation (GGA)[67], and also PBE GGA for solid state and surface systems (PBEsol GGA)[68] for purposes of comparison. Spin-polarization effects have been considered in all DFT calculations. The Γ-centered k mesh depends on the system to be analyzed, as specified below. The energy convergence is reached by setting any component of force exerted on each atom is not greater than 0.1 eV/nm. The energy cutoff is set to be 400 eV for any system in this work.

We first calculate lattice constants, cohesive energies, and magnetic moment of three pure fcc metals (Ni, Pt, and Pd) to assess the effectiveness of our DFT method described above by comparing with experimental data. In these calculations, we always use a fcc primitive cell and the k mesh of $61 \times 61 \times 61$. The cohesive energy is calculated from $E_{\text{coh}} = E_{\text{gas}} - \sigma_{\text{bulk}}$, where σ_{bulk} is the energy per atom in the primitive cell, and E_{gas} is the energy of one atom in the gas

phase. As can be seen from Table 2.2, the lattice constants, cohesive energies, and magnetic moment from both PBE and PBEsol calculations have overall agreement with experimental values. For fcc Ni, both lattice constant and cohesive energy from PBE are better (closer to the experimental value) than PBEsol, but magnetic moment from PBEsol is slightly better than PBE. For fcc Pt or Pd, the PBEsol value of lattice constant is better than the PBE value, but the cohesive energy from PBE is better than PBEsol. Both PBE and PBEsol predict no magnetism for fcc Pt, and therefore it is consistent with experiment, but not consistent for fcc Pd. This inconsistency of magnetic moment from GGA for fcc Pd has been noted previously[69, 70]. However, our test shows that the contribution to the energy per Pd atom from the magnetism is below 1 meV. Also considering the cancellation of such contributions in an energy difference for a system including Pd, one can neglect the artificial magnetic contribution, and therefore the results from PBE or PBEsol calculations is still reliable for total-energy analyses (not for studying magnetism). Thus, in this work, we choose PBE and PBEsol functionals. In fact, the lattice constants calculated from both functionals for the Ni-Pt alloys (Ni$_3$Pt, NiPt, and NiPt$_3$) are also in excellent agreement with available experimental data, as listed in Table 2.3.

System	Method	a (nm)	E_{coh} (eV)	m (μ_B)
Ni	PBE	**0.3518**	**4.787**	0.6270
	PBEsol	0.3462	5.457	**0.6166**
	experiments	0.35239[a]	4.44[b]	0.6060[c]
Pt	PBE	0.3968	**5.489**	**0.0000**
	PBEsol	**0.3916**	6.405	**0.0000**
	experiments	0.39160[d]	5.84[b]	0.0000
Pd	PBE	0.3944	**3.743**	0.3377[e]

PBEsol	**0.3874**	4.471	**0.2124**[e]
experiments	0.38893[f]	3.89[b]	0.0000

Table 2.2 Calculated lattice constants (a), cohesive energies (E_{coh}), and magnetic moments (m). For fcc metals (Ni, Pt, and Pd) from our DFT calculations with PBE and PBEsol functionals, compared with experimental values. A bold font represents a value closer to the experimental data in the two values from PBE and PBEsol calculations. [a]At 25 °C[71]. [b]Ref. 72. [c]Ref. 73. [d]Extrapolated to 0 K[74]. [e]PBE or PBEsol GGA cannot reproduce nonmagnetic property of pure fcc Pd[69, 70]. [f]At room temperature[75].

Next, we consider the thermodynamic propensity for alloy formation of Ni and Pt versus Ni and Pd. We analyze potential alloy formation for three different stoichiometries: Ni_3X, NiX, and NiX_3, where X = Pt or Pd. Crystal structures for these alloys are selected to correspond to CuAu for NiX, and Cu_3Au for the other cases. We determine the formation energy (or intermixing energy), E_{mix}, which corresponds to the energy change between an initial state of separated metals and a final alloyed state. The energy change is given per appropriate pair or quartet of atoms: 3Ni + 1X for Ni_3X, 1Ni + 1X for NiX, and 1Ni +3X for NiX_3. Note that the formation energy for a bulk multicomponent material from the DFT calculation is often compared with its corresponding standard formation enthalpy[76], which can be experimentally measured at the standard pressure of 100 kPa and a specified temperature (usually 298.15 K). Results shown in Table 2.2 reveal negative formation energies for all Pt + Ni alloys (i.e., intermixing is thermodynamically preferred), but positive for all Ni + Pd alloys (i.e., intermixing is disfavored). Why the 3d-5d compounds (CuAu and NiPt) are stable, whereas the 3d-4d compounds (CuAg and NiPd) are not,

has been analyzed by Wang and Zunger[77]. Here we show that, besides the NiX phases, the Ni_3X or NiX_3, phases still follow this rule. The physical origin of this behavior has been attributed to relativistic effects[78]. In these calculations, we use the primitive cells corresponding to CuAu or Cu_3Au structure and the k mesh is always taken to be $61 \times 61 \times 61$. Incidentally, we also note the magnetism predicted from our DFT calculations for all these alloys, as listed in Table 2.2.

System	Prototype structure	Method	a (nm)	c (nm)	m (μ_B)	E_{mix} (eV)
NiPt	CuAu	PBE	0.3843	0.3629	1.0613	-0.193
		PBEsol	0.3791	0.3571	1.0033	-0.177
		experiment	0.3823[a]	0.3589[a]		
Ni_3Pt	Cu_3Au	PBE	0.3655		2.4614	-0.288
		PBEsol	0.3599		2.2789	-0.265
		experiment	0.36515[a]			
$NiPt_3$	Cu_3Au	PBE	0.3875		1.1230	-0.272
		PBEsol	0.3823		1.0172	-0.256
		experiment	0.385[a]			
NiPd	CuAu	PBE	0.3833	0.3607	1.0854	+0.057
		PBEsol	0.3764	0.3557	1.0559	+0.067
Ni_3Pd	Cu_3Au	PBE	0.3644		2.3823	+0.114
		PBEsol	0.3585		2.3355	+0.126
$NiPd_3$	Cu_3Au	PBE	0.3857		1.7010	+0.100
		PBEsol	0.3791		1.5560	+0.116

Table 2.3 Alloy lattice constants (a and c, or a), magnetic moments (m) per unit formula, and formation energies (E_{mix}). For NiPt, Ni_3Pt, $NiPt_3$, NiPd, Ni_3Pd, and $NiPd_3$, from our DFT calculations with PBE and PBEsol functionals, compared with available experimental values. [a]Ref. 78.

Section 2. DFT Results for Vacancy Formation Energies and Hopping Barriers Relevant for Intermixing

For analysis of <u>vacancy-mediated diffusion of Ni through unstrained and strained bulk Pt</u>, we determine both the formation energy, $E_{fv}(v$ in Pt), for a vacancy in pure bulk Pt, and also the refined formation energy, $E_{fv}(Ni+v$ in Pt), of a vacancy next to a single Ni impurity in bulk Pt. In addition, we determine the activation barrier, $E_{dv}(v$ in Pt), for a Pt atom to hop to an adjacent vacancy in pure Pt, and the barrier, $E_{dv}(Ni+v$ in Pt), for a Ni impurity to hop to an adjacent vacancy in Pt. In these calculations, we always use a cubic unit cell of $4 \times 4 \times 4$ (in units of fcc lattice constant a for cell lengths) and the k mesh is always taken to be $5 \times 5 \times 5$. Below, we show results from the most appropriate analysis where Pt atoms are fully relaxed (rlx). However, for comparison, we also show results where they are fixed at their bulk fcc positions (fix), thereby allowing assessment of the effect of relaxation.

To determine the conventional vacancy formation energy, $E_{fv}(v$ in Pt) in pure fcc Pt, the standard procedure is as follows. One evaluates the total energy E_{vac} for a periodic supercell of N fcc sites where N - 1 sites are populated by metal atoms, and one site is a vacancy. If E_{bulk} denotes the total energy of the same cell populated with N metal atoms, then one has that $E_{fv}(v$ in Pt) = E_{vac} - (N - 1)E_{bulk}/N. To determine the less conventional $E_{fv}(Ni+v$ in Pt), we calculate the total energy $E_{vac}(Ni$ in Pt) of a supercell of N fcc sites with N - 2 sites occupied by Pt, one site occupied by Ni, and one vacancy adjacent to the Ni. We also determine the total energy $E_{bulk}(Ni$ in Pt) of a supercell of N fcc sites with N - 1 sites occupied by Pt and one site occupied by Ni. Then, together with E_{bulk} for pure Pt mentioned above, one has that $E_{fv}(Ni+v$ in Pt) = $E_{vac}(Ni$ in Pt) + E_{bulk}/N - $E_{bulk}(Ni$ in Pt). To estimate activation barriers for hopping to a vacancy, rather than performing a Nudged Elastic Band (NEB) analysis to map out the minimum energy path for hopping, we just determine the difference in energy between that at the initial site and that at the midpoint of the

line connecting initial and final sites of the hopping atom. Table 2.4 shows results for E_{fv} and E_{dv} for the case where there is no strain in the Pt.

	E_{fv}(v in Pt)	E_{dv}(v in Pt)	E_{fv}(Ni+v in Pt)	E_{dv}(Ni+v in Pt)
PBE	0.646 (0.971)	1.233 (1.754)	0.693 (1.110)	0.840 (0.740)
PBEsol	0.844 (1.186)	1.409 (2.006)	0.937 (1.381)	0.928 (0.818)

Table 2.4 Results for vacancy formation energies (in eV) in fcc Pt in the absence of strain. The values outside and inside a parenthesis are for rlx and fix, respectively.

As noted in the text, Pt layers in the NP are expected to be under compressive strain, $\varepsilon < 0$, due to epitaxy with Ni layers, and due to incorporation of Ni into Pt (where the latter effect is reflected in Vegard's law). Thus, we determine the behavior of both E_{fv}(v in Pt) and E_{fv}(Ni+v in Pt) for a range of compressive strain, $-12\% < \varepsilon \leq 0\%$ just using the PBEsol functional. The most detailed analysis is for triaxial strain, but we also present limited results for biaxial compressive strain. Results shown in Figure 2.10 demonstrate that both E_{fv}(v in Pt) and E_{fv}(Ni+v in Pt) decrease strongly with increasing magnitude $|\varepsilon|$ of the triaxial compressive strain. A weaker decrease is observed for biaxial strain.

We have also performed more limited analysis of E_{dv}(v in Pt) and E_{dv}(Ni+v in Pt) using the PBEsol functional. Just reporting results from analysis which relaxes atom positions (rlx), we find that E_{dv}(v in Pt) $\approx 1.41 - 15.2\varepsilon$ eV for triaxial strain, and E_{dv}(v in Pt) $\approx 1.41 - 9.21\varepsilon$ eV ($1.41 + 19.3\varepsilon$ eV) for biaxial strain orthogonal (parallel) to the direction of imposed strain, at least for small $|\varepsilon|$ below about 3%. We also find that E_{dv}(Ni+v in Pt) $\approx 0.93 - 14.7\varepsilon$ eV for triaxial strain,

and E_{dv}(Ni+v in Pt) $\approx 0.93 - 7.3\varepsilon$ eV $(0.93 + 9.1\varepsilon$ eV) for biaxial strain orthogonal (parallel) to the direction of imposed strain, at least for small $|\varepsilon|$ below about 3%.

For <u>vacancy-mediated diffusion of Pt through unstrained and strained bulk Ni</u>, we perform analysis analogous to the above treatment for Ni diffusion through Pt. Table 2.5 shows results for the relevant E_{fv} and E_{dv} for the case where there is no strain in the Ni. As noted in the text, Ni layers in the NP are expected to be under tensile strain, $\varepsilon > 0$, due to epitaxy with Pt layers, and due to potential incorporation of Pt into Ni. In Figure 2.11, we just show results from the PBEsol functional, revealing that both E_{fv}(v in Ni) and E_{fv}(Pt+v in Ni) increase with increasing ε (at least up to about 6%) for triaxial tensile strain. A weaker increase is observed for biaxial strain.

	E_{fv}(v in Ni)	E_{dv}(v in Ni)	E_{fv}(Pt+v in Ni)	E_{dv}(Pt+v in Ni)
PBE	1.444 (1.502)	1.085 (1.613)	1.349 (1.316)	1.295 (2.996)
PBEsol	1.635 (1.703)	1.189 (1.762)	1.512 (1.498)	1.426 (3.286)

Table 2.5 Results for E_{fv} and E_{dv} (in eV) for the case where there is no strain in fcc Ni. The values outside and inside a parenthesis are for rlx and fix, respectively.

Using the PBEsol functional and relaxing atom positions (rlx), we find that E_{dv}(v in Ni) $\approx$ $1.19 - 6.3\varepsilon$ eV for triaxial strain, and E_{dv}(v in Ni) $\approx 1.19 - 9.8\varepsilon$ $(1.19 + 9.9\varepsilon)$ eV for biaxial strain orthogonal (parallel) to the direction of imposed strain, at least for small $|\varepsilon|$ below about 3%. We also find that E_{dv}(Pt+v in Ni) $\approx 1.43 - 4.3\varepsilon$ eV for triaxial strain, and E_{dv}(Pt+v in Ni) $\approx 1.43 - 13.1\varepsilon$ eV $(1.43 + 10.3\varepsilon$ eV) for biaxial strain orthogonal (parallel) to the direction of imposed strain, at least for small $|\varepsilon|$ below about 3%.

References

1.   Li, L. D.; Zhou, L.; Ould-Chikh, S.; Anjum, D. H.; Kanoun, M. B.; Scaranto, J.; Hedhili, M. N.; Khalid, S.; Laveille, P. V.; D'Souza, L.; Clo, A.; Basset, J. M., Controlled Surface Segregation Leads to Efficient Coke-Resistant Nickel/Platinum Bimetallic Catalysts for the Dry Reforming of Methane. *ChemCatChem* **2015,** *7* (5), 819-829.

2.   Li, X.; An, L.; Chen, X.; Zhang, N. L.; Xia, D. G.; Huang, W. F.; Chu, W. S.; Wu, Z. Y., Durability Enhancement of Intermetallics Electrocatalysts via N-anchor Effect for Fuel Cells. *Sci Rep-Uk* **2013,** *3*, 3234.

3.   Xia, T. Y.; Liu, J. L.; Wang, S. G.; Wang, C.; Sun, Y.; Gu, L.; Wang, R. M., Enhanced Catalytic Activities of NiPt Truncated Octahedral Nanoparticles toward Ethylene Glycol Oxidation and Oxygen Reduction in Alkaline Electrolyte. *ACS Appl. Mater. Inter.* **2016,** *8* (17), 10841-10849.

4.   Xu, S. C.; Walter, E. D.; Zhao, Z. C.; Hu, M. Y.; Han, X. W.; Hu, J. Z.; Bao, X. H., Dynamic Structural Changes of SiO2 Supported Pt-Ni Bimetallic Catalysts over Redox Treatments Revealed by NMR and EPR. *J. Phys. Chem. C* **2015,** *119* (36), 21219-21226.

5.   Zhu, Z. J.; Zhai, Y. L.; Dong, S. J., Facial Synthesis of PtM (M = Fe, Co, Cu, Ni) Bimetallic Alloy Nanosponges and Their Enhanced Catalysis for Oxygen Reduction Reaction. *ACS Appl. Mater. Inter.* **2014,** *6* (19), 16721-16726.

6.   Zhang, S.; Zhang, X.; Jiang, G. M.; Zhu, H. Y.; Guo, S. J.; Su, D.; Lu, G.; Sun, S. H., Tuning Nanoparticle Structure and Surface Strain for Catalysis Optimization. *J. Am. Chem. Soc.* **2014,** *136* (21), 7734-7739.

7.   Zhu, J.; Yang, Y.; Chen, L.; Xiao, W.; Liu, H.; Abruna, H. D.; Wang, D., Copper-Induced Formation of Structurally Ordered Pt-Fe-Cu Ternary Intermetallic Electrocatalysts with Tunable Phase Structure and Improved Stability. *Chem. Mater.* **2018,** *30*, 5987-5995.

8.   Bhunia, K.; Khilari, S.; Pradhan, D., Monodispersed PtPdNi Trimetallic Nanoparticles-Integrated Reduced Graphene Oxide Hybrid Platform for Direct Alcohol Fuel Cell. *ACS Sustain. Chem. Eng.* **2018,** *6* (6), 7769-7778.

9.   Ross, M. B.; De Luna, P.; Li, Y.; Dinh, C.-T.; Kim, D.; Yang, P.; Sargent, E. H., Designing materials for electrochemical carbon dioxide recycling. *Nat. Catal.* **2019,** *2*, 648-658.

10.   Zou, L.; Fan, J.; Zhou, Y.; Wang, C.; Li, J.; Zou, Z.; Yang, H., Conversion of PtNi alloy from disordered to ordered for enhanced activity and durability of methanol tolerant oxygen reduction reaction. *Nano Res.* **2015,** *8* (8), 2777-2788.

11.   Cui, C.; Gan, L.; Li, H.; Yu, S.; Heggen, M.; Strasser, P., Octahedral PtNi Nanoparticle Catalysts: Exceptional Oxygen Reduction Activity by Tuning the Alloy Particle Surface Composition. *Nano Lett.* **2012,** *12*, 5885-5889.

12.   Sneed, B.; Brodsky, C.; Kuo, C. H.; Lamontagne, L.; Jiang, Y.; Wang, Y.; Tao, F.; Huang, W.; Tsung, C. K., Nanoscale-Phase-Separated Pd-Rh Boxes Synthesized via Metal Migration: An Archetype for Studying Lattice Strain and Composition Effects in Electrocatalysis. *J. Am. Chem. Soc.* **2013,** *135* (39), 14691-14700.

13.   Sneed, B.; Young, A.; Jalalpoor, D.; Golden, M.; Mao, S.; Jiang, Y.; Wang, Y.; K., T. C., Shaped Pd-Ni-Pt Core-Sandwich-Shell Nanoparticles: Influence of Ni Sandwich Layers on Catalytic Electrooxidations. *ACS Nano* **2014,** *8* (7), 7239-7250.

14.   Park, K. W.; Choi, J. H.; Kwon, B. K.; Lee, S. A.; Sung, Y. E., Chemical and Electronic Effects of Ni in Pt/Ni and Pt/Ru/Ni Alloy Nanoparticles in Methanol Electrooxidation. *J. Phys. Chem. B* **2002,** *106* (8), 1869-1877.

15.   Yang, H.; Vogel, W.; Lamy, C.; Alonso-Vante, N., Structure and Electrocatalytic Activity of Carbon-Supported Pt-Ni Alloy Nanoparticles Toward the Oxygen Reduction Reaction. *J. Phys. Chem. B* **2004,** *108* (30), 11024-11034.

16.   Strasser, P.; Kuehl, S., Dealloyed Pt-based core-shell oxygen reduction electrocatalysts. *Nano Energy* **2016,** *29*, 166-177.

17.   Gamler, J. T.; Ashberry, H. M.; Skrabalak, S. E.; Koczkur, K. M., Random Alloyed versus Intermetallic Nanoparticles: A Comparison of Electrocatalytic Performance. *Adv. Mater.* **2018,** *30* (40), 1801563.

18.   Wolff, I. M.; Hill, P. J., Platinum Metals-Based Intermetallics for High-Temperature Service. *Platin Met Rev* **2000,** *44* (4), 158-166.

19.   Zhao, Y.; Yu, J. K.; Wu, L. L.; Wan, B.; Zhang, Y. K.; Gao, R.; Zhang, J. W.; Gou, H. Y., Mechanical properties and electronic structures of diverse Pt-Al intermetallics: First-principles calculations. *Comp Mater Sci* **2016,** *124*, 273-281.

20.   Furukawa, S.; Ehara, K.; Ozawa, K.; Komatsu, T., A study on the hydrogen activation properties of Ni-based intermetallics: a relationship between reactivity and the electronic state. *Phys Chem Chem Phys* **2014,** *16* (37), 19828-19831.

21.   Xiao, W.; Lei, W.; Gong, M.; Xin, H. L.; Wang, D., Recent Advances of Structurally Ordered Intermetallic Nanoparticles for Electrocatalysis. *ACS Catal.* **2018,** *8* (4), 3237-3256.

22.   Hasché, F.; Oezaslan, M.; Strasser, P., Activity, Structure and Degradation of Dealloyed PtNi$_3$ Nanoparticle Electrocatalyst for the Oxygen Reduction Reaction in PEMFC. *J. Electrochem. Soc.* **2012,** *159* (1), B24-B33.

23.   Stamenkovic, V. R.; Fowler, B.; Mun, B. S.; Wang, G.; Ross, P. N.; Lucas, C. A.; Markovic, N. M., Improved Oxygen Reduction Activity on $Pt_3Ni(111)$ via Increased Surface Site Availability. *Science* **2007,** *315*, 493-497.

24.   Wang, D.; Xin, H. L.; Hovden, R.; Wang, H.; Yu, Y.; Muller, D. A.; DiSalvo, F. J.; Abruña, H. D., Structurally ordered intermetallic platinum–cobalt core–shell nanoparticles with enhanced activity and stability as oxygen reduction electrocatalysts. *Nat. Mater.* **2013,** *12*, 81-87.

25.   Dikshtein, I.; Koledov, V.; Shavrov, V.; Tulaikova, A.; Cherechukin, A.; Buchelnikov, V.; Khovailo, V.; Matsumoto, M.; Takagi, T.; Tani, J., Phase transitions in intermetallic compounds Ni-Mn-Ga with shape memory effect. *IEEE Trans.* **1999,** *35* (5), 3811-3813.

26.   Uijttewaal, M. A.; Hickel, T.; Neugebauer, J.; Gruner, M. E.; Entel, P., Understanding the Phase Transitions of the Ni_2MnGa Magnetic Shape Memory System from First Principles. *Phys. Rev. Lett.* **2009,** *102*, 035702/1-035702/4.

27.   Evans, M. J.; Wu, Y.; Kranak, V. F.; Newman, N.; Reller, A.; Garcia-Garcia, F. J.; Haeussermann, U., Structural properties and superconductivity in the ternary intermetallic compounds MAB (M=Ca, Sr, Ba; A=Al, Ga, In; B=Si, Ge, Sn). *Phys. Rev. B* **2009,** *80* (6), 064514.
28.   Chou, K.-C.; Xu, K., A new model for hydriding and dehydriding reactions in intermetallics. *Intermetallics* **2007,** *15*, 767-777.

29.   Fernandez, J. F.; Cuevas, F.; Leardini, F.; Bodega, J.; Ares, J. R.; Garces, G.; Perez, P.; Sanchez, C., A new pseudo-binary $Mg_{(6)}Ni_{(0.5)}Pd_{(0.5)}$ intermetallic compound stabilised by Pd for hydrogen storage. *J. Alloy. Compd.* **2010,** *495* (2), 663-666.

30.   Cava, R. J.; Takagi, H.; Zandbergen, H. W.; Krajewski, J. J.; Peck Jr., W. F.; Siegrist, T.; Batlogg, B.; van Dover, R. B.; Felder, R. J.; Mizuhashi, K.; Lee, J. O.; Eisaki, H.; Uchida, S., Superconductivity in the quaternary intermetallic compounds $LnNi_2B_2C$. *Nature* **1994,** *367*, 252-253.

31.   Clarke, S. M.; Walsh, J. P. S.; Amsler, M.; Malliakas, C. D.; Yu, T.; Goedecker, S.; Wang, Y.; Wolverton, C.; Freedman, D. E., Discovery of Superconducting Cu-Bi Intermetallic Compound by High-Pressure Synthesis. *Angew. Chem.* **2016,** *55*, 13446-13449.

32.   Osswald, J.; Kovnir, K.; Armbruster, M.; Giedigkeit, R.; Jentoft, R. E.; Wild, U.; Grin, Y.; Schlogl, R., Palladium-Gallium Intermetallic Compounds for the Selective Hydrogenation of Acetylene Part I: Preparation and Structural Investigation under Reaction Conditions. *J. Catal.* **2008,** *258*, 219-227.

33.   Kovnir, K.; Osswald, J.; Armbruster, M.; Teschner, D.; Weinberg, G.; Wild, U.; Knop-Gericke, A.; Ressler, T.; Grin, Y.; Schlogl, R., Etching of the Intermetallic Compounds PdGa and Pd_3Ga_7: An Effective Way to Increase Catalytic Activity. *J. Catal.* **2009,** *264*, 93-103.

34.   Armbruster, M.; Kovnir, K.; Behrens, M.; Teschner, D.; Grin, Y.; Schlogl, R., Pd-Ga Intermetallic Compounds as Highly Selective Semihydrogenation Catalysts. *J. Am. Chem. Soc.* **2010,** *132*, 14745-14747.

35.   Besenbacher, F.; Chorkendorff, I.; Clausen, B. S.; Hammer, B.; Molenbroek, A. M.; Norskov, J. K.; Stensgaard, I., Design of a surface alloy catalyst for steam reforming. *Science* **1998,** *279* (5358), 1913-1915.

36.   Studt, F.; Abild-Pedersen, F.; Bligaard, T.; Sorensen, R. Z.; Christensen, C. H.; Norskov, J. K., Identification of non-precious metal alloy catalysts for selective hydrogenation of acetylene. *Science* **2008,** *320* (5881), 1320-1322.

37.   Armbruster, M.; Kovnir, K.; Friedrich, M.; Teschner, D.; Wowsnick, G.; Hahne, M.; Gille, P.; Szentmiklósi, L.; Feuerbacher, M.; Heggen, M.; Girgsdies, F.; Rosenthal, D.; Schlogl, R.; Grin, Y., Al$_{13}$Fe$_4$ as a low-cost alternative for palladium in heterogeneous hydrogenation. *Nat. Mater.* **2012,** *11* (8), 690-693.

38.   Yan, Y.; Du, J. S.; Gilroy, K. D.; Yang, D.; Xia, Y.; Zhang, H., Intermetallic Nanocrystals: Syntheses and Catalytic Applications. *Adv. Mater.* **2017,** *29* (14), 1605997.

39.   Feng, Q.; Zhao, S.; Wang, Y.; Dong, J.; Chen, W.; He, D.; Wang, D.; Yang, J.; Zhu, Y.; Zhu, H.; Gu, L.; Li, Z.; Liu, Y.; Yu, R.; Li, J.; Li, Y., Isolated Single-Atom Pd Sites in Intermetallic Nanostructures: High Catalytic Selectivity for Semihydrogenation of Alkynes. *J. Am. Chem. Soc.* **2017,** *139* (21), 7294-7301.

40.   Furukawa, S.; Komatsu, T., Intermetallic Compounds: Promising Inorganic Materials for Well-Structured and Electronically Modified Reaction Environments for Efficient Catalysis. *ACS Catal.* **2017,** *7* (1), 735-765.

41.   Zhou, H.; Yang, X.; Li, L.; Liu, X.; Huang, Y.; Pan, X.; Wang, A.; Li, J.; Zhang, T., PdZn Intermetallic Nanostructure with Pd-Zn-Pd Ensembles for Highly Active and Chemoselective Semi-Hydrogenation of Acetylene. *ACS Catal.* **2016,** *6* (2), 1054-1061.

42.   Maligal-Ganesh, R.; Xiao, C.; Goh, T. W.; Wang, L.-L.; Gustafson, J.; Pei, Y.; Qi, Z.; Johnson, D. D.; Zhang, S.; Tao, F.; Huang, W., A Ship-in-a-Bottle Strategy to Synthesize Encapsulated Intermetallic Nanoparticle Catalysts: Exemplified for Furfural Hydrogenation. *ACS Catal.* **2016,** *6* (3), 1754-1763.

43.   Enayati, M. H.; Salehi, M., Formation mechanism of Fe$_3$Al and FeAl intermetallic compounds during mechanical alloying. *J. Mater. Sci.* **2005,** *40*, 3933-3938.

44.   Furukawa, S.; Komatsu, T., Intermetallic Compounds: Promising Inorganic Materials for Well-Structured and Electronically Modified Reaction Environments for Efficient Catalysis. *ACS Catal.* **2017,** *7*, 735-765.

45.   Schaefer, Z. L.; Vaughn II, D. D.; Schaak, R. E., Solution chemistry synthesis, morphology studies, and optical properties of distinct nanocrystalline Au-Zn intermetallic compounds. *J. Alloy. Compd.* **2010,** *490*, 98-102.

46.   Maksimuk, S.; Yang, S.; Peng, Z.; Yang, H., Synthesis and Characterization of Ordered Intermetallic PtPb Nanorods. *J. Am. Chem. Soc.* **2007,** *129*, 8684-8685.

47.   Leonard, B. M.; Zhou, Q.; Wu, D.; DiSalvo, F. J., Facile Synthesis of PtNi Intermetallic Nanoparticles: Influence of Reducing Agent and Precursors on Electrocatalytic Activity. *Chem. Mater.* **2011,** (23), 1136-1146.

48.   Wang, D. S.; Peng, Q.; Li, Y. D., Nanocrystalline Intermetallics and Alloys. *Nano Res.* **2010,** *3* (8), 574-580.

49.   Belova, I. V.; Murch, G. E., Interdiffusion in Intermetallics. *Metall. Mater. Trans. A* **2013,** *44A* (10), 4417-4421.

50.   Mehrer, H., Diffusion in intermetallics. *Mater. T. Jim* **1996,** *37* (6), 1259-1280.

51.   Brodsky, C.; Young, A.; Ng, K.; Kuo, C. H.; Tsung, C. K., Electrochemically Induced Surface Metal Migration in Well-Defined Core-Shell Nanoparticles and Its General Influence on Electrocatalytic Reactions. *ACS Nano* **2014,** *8* (9), 9368-9378.

52.   Hasché, F.; Oezaslan, M.; Strasser, P., Activity, Structure and Degradation of Dealloyed PtNi₃ Nanoparticle Electrocatalyst for the Oxygen Reduction Reaction in PEMFC. *J. Electrochem. Soc.* **2012,** *159* (1), B24-B33.

53.   Zou, L.; Fan, J.; Zhou, Y.; Wang, C.; Li, J.; Zou, Z.; Yang, H., Conversion of PtNi alloy from disordered to ordered for enhanced activity and durability of methanol tolerant oxygen reduction reaction. *Nano Res.* **2015,** *8* (8), 2777-2788.

54.   Du, P.; Wu, P.; Cai, C., Mechanistic Insight into the Facet-Dependent Adsorption of Methanol on a Pt₃Ni Nanocatalyst. *J. Phys. Chem. C* **2015,** *119*, 18352-18363.

55.   Vimont, A.; Thibault-Starzyk, F.; Daturi, M., Analysing and understanding the active site by IR spectroscopy. *Chem. Soc. Rev.* **2010,** *39* (12), 4928-4950.

56.   Unterhalt, H.; Rupprechter, G.; Freund, H.-J., Vibrational Sum Frequency Spectroscopy on Pd(111) and Supported Pd Nanoparticles: CO Adsorption from Ultrahigh Vacuum to Atmospheric Pressure. *J. Phys. Chem. B* **2002,** *106* (2), 356-367.

57.   Crossley, A.; King, D. A., Infrared spectra for co isotopes chemisorbed on Pt "111": Evidence for strong absorbate coupling interactions. *Surf. Sci.* **1977,** *68*, 528-538.

58.   Primet, M., Electronic transfer and ligand effects in the infrared spectra of adsorbed carbon monoxide. *J. Catal.* **1984,** *88* (2), 273-282.

59. Sigalas, M.; Papaconstantopoulos, D. A.; Bacalis, N. C., Total energy and band structure of the 3d, 4d, and 5d metals. *Phys. Rev. B* **1991,** *45*, 5777-5783.

60. Pei, Y.; Qi, Z.; Goh, T. W.; Wang, L.-L.; Maligal-Ganesh, R. V.; MacMurdo, H. L.; Zhang, S.; Xiao, C.; Li, X.; Tao, F.; Johnson, D. D.; Huang, W., Intermetallic structures with atomic precision for selective hydrogenation of nitroarenes. *J. Catal.* **2017,** *356*, 307-314.

61. Mattsson, T. R.; Mattsson, A. E., Calculating the vacancy formation energy in metals: Pt, Pd, and Mo. *Phys. Rev. B* **2002,** *66*, 214110.

62. Lai, K. C.; Han, Y.; Spurgeon, P.; Huang, W.; Thiel, P. A.; Liu, D.-J.; Evans, J. W., Reshaping, intermixing, and coarsening for metallic nanocrystals: Non-equilibrium statistical mechanical and coarse-grained modeling. *Chem. Rev.* **2019,** *119*, 6670-6678.

63. Chen, M.; Han, Y.; Goh, T. W.; Sun, R.; Maligal-Ganesh, R. V.; Pei, Y.; Tsung, C. K.; Evans, J. W.; Huang, W., Kinetics, Energetics, and Size-dependence of the Transformation from Pt to Ordered PtSn Intermetallic Nanoparticles. *Nanoscale* **2019,** *11*, 5336-5345.

64. Kuo, C.-H.; Lamontagne, L. K.; Brodsky, C. N.; Chou, L.-Y.; Zhuang, J.; Sneed, B. T.; Sheehan, M. K., Tsung, C.-K. The Effect of Lattice Strain on the Catalytic Properties of Pd Nanocrystals. *ChemSusChem*, **2013,** *6*, 1993-2000.

65. Kresse, G.; Furthmüller, J. Efficient iterative schemes for *ab initio* total-energy calculations using a plane-wave basis set. *Phys. Rev. B*, **1996,** *54*, 11169-11186.

66. Kresse, G.; Joubert, D. From ultrasoft pseudopotentials to the projector augmented-wave method. *Phys. Rev. B.*, **1999,** *59*, 1758-1775.

67. Perdew, J. P.; Burke, K.; Ernzerhof, M. Generalized Gradient Approximation Made Simple. *Phys. Rev. Lett.*, **1996,** *77*, 3865-3868.

68. Perdew, J. P.; Ruzsinszky, A.; Csonka, G. I.; Vydrov, O. A.; Scuseria, G. E.; Constantin, L. A.; Zhou, X.; Burke, K. Restoring the Density-Gradient Expansion for Exchange in Solids and Surfaces. *Phys. Rev. Lett.*, **2008,** *100*, 136406.

69. Alexandre, S. S.; Mattesini, M.; Soler, J. M.; Yndurain, F. Comment on "Magnetism in Atomic-Size Palladium Contacts and Nanowires". *Phys. Rev. Lett.*, **2006,** *96*, 079701.

70. Stewart, D. A. Magnetism in coaxial palladium nanowires. *J. Appl. Phys.*, **2007,** *101*, 09D503.

71. Jette, E. R.; Foote, F. Precision Determination of Lattice Constants. *J. Chem. Phys.*, **1935,** *3*, 605-616.

72. Kittel, C. *Introduction to Solid State Physics*, John Wiley & Sons, New York, **1996**.

73.   Mook, H. A. Magnetic Moment Distribution of Nickel Metal. *Phys. Rev.*, **1966,** *148*, 495-501.

74.   Arblaster, J. W. Crystallographic Properties of Platinum. *Platin. Met. Rev.*, **1997,** *41*, 12-21.

75.   Lamber, R.; Wetjen, S.; Jaeger, N. I. Size dependence of the lattice parameter of small palladium particles. *Phys. Rev. B*, **1995,** *51*, 10968-10971.

76.   Jiang, Y.; Shi, Y.; Xiang, X.; Qi, J.; Han, Y.; Liao, Z.; Lu, T. Thermodynamic Stabilities of Perfect and Vacancy-Defected Li_2TiO_3 (001) Surfaces from First-Principles Analyses. *Phys. Rev. Appl.*, **2019,** *11*, 054088.

77.   Wang, L. G.; Zunger, A. Why are the *3d-5d* compounds CuAu and NiPt stable, whereas the *3d-4d* compounds CuAg and NiPd are not. *Phys. Rev. B*, **2003,** *67*, 092103.

78.   Esch, U.; Schneider, A. The System Ni-Pt. *Z. Elektrochem.* **1944,** *50*, 268-274.

Chapter 3

Investigating Lattice Strain Impact on the Alloyed Surface of Small Au@PdPt

Core-Shell Nanoparticles
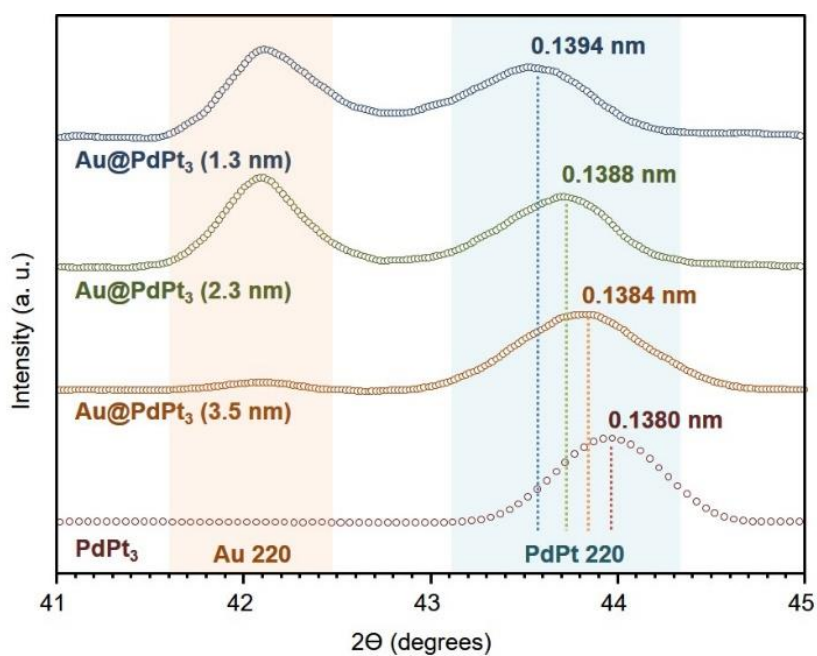
A significant portion of the work described in Chapters 3 and 4 has been published in: Williams,

B. P.*; Yaguchi, M.*; Lo, W.-S.; Kao, C.-R.; Lamontagne, L. K.; Sneed, B. T.; Brodsky, C. N.;

Chou, L.-Y.; Kuo, C.-H.; Tsung, C.-K. Investigating Lattice Strain Impact on the Alloyed Surface

of Small Au@PdPt Core-Shell Nanoparticles. *Nanoscale*, **2020**, DOI: 10.1039/D0NR01021A.

3.1 Abstract

We investigated lattice strain on alloyed surfaces using ~10 nm core-shell nanoparticles with controlled size, shape, and composition. We developed a wet-chemistry method for synthesizing small octahedral PdPt alloy nanoparticles and Au@PdPt core-shell nanoparticles with Pd-Pt alloy shells and Au cores. Upon introduction of the Au core, the size and shape of the overall nanostructure and the composition of the alloyed PdPt were maintained, enabling the use of the electrooxidation of formic acid as a probe to compare the surface structures with different lattice strain. We have found that the structure of the alloyed surface is indeed impacted by the lattice strain generated by the Au core. To further reveal the impact of lattice strain, we fine-tuned the shell thickness. Then, we used synchrotron-based x-ray diffraction to investigate the degree of lattice strain, finding that the degree of surface strain is dependent on the shell thickness.

3.2 Introduction

Precious metal nanoparticles are the major active catalyst in many electrochemical energy conversion processes.[1-5] Due to their high cost, much effort has been given to the ongoing improvement of their catalytic properties by refining their shape[6-12] and alloying them with other metals.[13-16] During this process, the influence of shape and alloying effects on catalytic activity has been studied.[3, 17-19] Even the investigation of the combined effect of shape and alloying has been reported: Markovic[20] has shown for Pt_3Ni crystal facets, for example, that alloying nickel into platinum can increase activity toward oxygen reduction, with a dependence on shape related to the dominant facet. This change in activity can be explained by an energy shift in the d-band center that affects catalysis by increasing or decreasing reactant absorption energies, leading to higher activities.[21-23] Creating surface lattice strain, which can similarly shift the d-band center, has been reported to promote catalytic activity as well.[1, 13, 24-29] However, unlike alloying and shape

control, which must be located at the surface to impact catalytic activity, lattice strain can impact surface reactivity through metal-metal interfaces that are more than a few atomic layers away.[1] This extended range of impact allows lattice strain to be imparted to a shape- and composition-controlled system where its effect can be tested without changing the dominant surface facet or composition.

To test this hypothesis, we selected a simple model system, choosing an octahedral shape, Pd-Pt alloy composition, and a Au core as the lattice strain source. There is an approximately 5% lattice mismatch between the Au core and PdPt shell that provides the lattice strain. The nanoparticles were characterized using transmission electron microscopy (TEM) and energy dispersive X-ray spectroscopy (EDX). The composition of the nanoparticles was characterized through scanning-TEM/EDX (STEM/EDX). The formic acid oxidation reaction (FOR) is used as a probe reaction to investigate the surface because it has been demonstrated to be sensitive to surface electronic structure.[30-31] We synthesized ~10 nm PdPt alloyed nanooctahedra and ~10 nm core-alloyed shell nanooctahedra with an 8 nm Au octahedral core and a 2 nm PdPt alloyed shell. Three alloy compositions were tested, Pd_3Pt_1, Pd_1Pt_1, and Pd_1Pt_3. It was found that the lattice strain generated by the Au core indeed changed FOR activity, regardless of the alloy composition. Core-alloyed shell nanoparticles were further synthesized with the same core size but different shell thickness (while maintaining shape and alloy composition).[32-33] Their FOR performance was compared with lattice strain analyzed by synchrotron-based high resolution powder x-ray diffraction (HRXRD). It was observed that there is an optimal intermediate level of lattice strain that maximizes FOR performance.

3.3 Synthesis

To have small nanoparticles with well-defined size, shape, alloying, and core-shell structure is not straightforward. We adapted a hydrothermal synthesis mediated by two common strategies: co-reduction[34] and seed-mediated growth.[35] The octahedral alloyed nanoparticles were synthesized through the hydrothermal co-reduction[34] of Pd^{2+} and Pt^{2+} by sodium citrate at 110 °C. Cetyltrimethylammonium bromide (CTAB) was used as a capping agent. The weak reducing agent and mild reaction temperature slow reduction and deposition rates, promoting formation of the (111) facets that dominate the surface of the octahedral shape. We found that the amount of oxygen in the synthesis solution is critical since oxygen could etch newborn nuclei and slow the growth rate. If too much oxygen is introduced, it leads to octahedra and nanoprisms that are still dominated by (111) facets but larger than our target size. Adjusting the molar ratio between the reactant Pt^{2+} and Pd^{2+} ions allowed for the three different compositions of the Pd_3Pt_1, Pd_1Pt_1, and Pd_1Pt_3 octahedra (Figures 3.1). To make core-shell structures, we synthesized 8 nm Au seeds of single crystalline structure and monodisperse truncated octahedral shape. While the nanoparticles do not serve as shape-directing agents, the presence of many (111) surface facets in the seeds promotes epitaxial growth. They are then added to the growth solution of Pd and Pt (DI water, Pt^{2+}, Pd^{2+}, and sodium citrate) before reduction in the oven. After reaction, Au@PdPt core-alloyed shell octahedra formed (Figures 3.1).
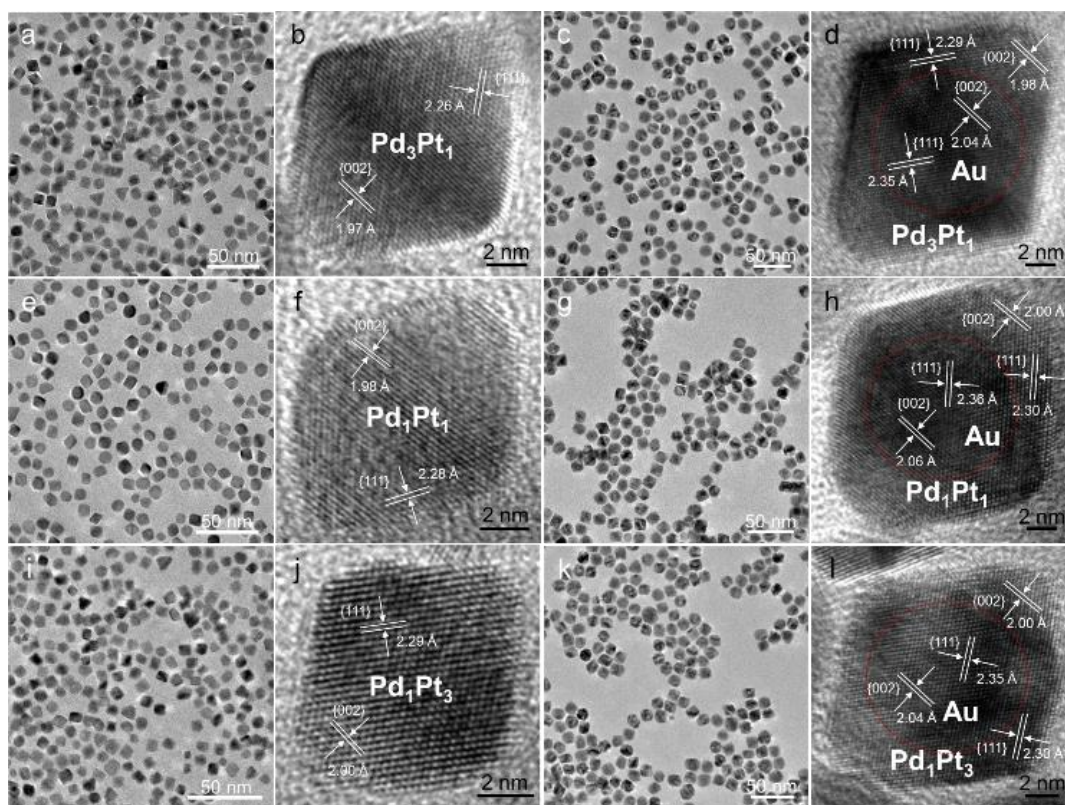
Figure 3.1 TEM images of (a, e, i) PdPt alloy octahedral nanoparticles and (c, g, k) Au@PdPt core-shell octahedral nanoparticles. High-resolution TEM images show the clear lattice fringes of (b, f, j) PdPt and (d, h, l) Au@PdPt with different Pd/Pt compositions. The dashed red line surrounds the Au core, in which lattice spacings are larger than in the shell due to the larger lattice parameter of Au than Pd and Pt (a_{Au} 4.087 Å, a_{Pd} 3.867 Å, and a_{Pt} 3.920 Å, respectively).

TEM images in Figure 1 show uniform PdPt alloy and Au@PdPt core-shell octahedral nanoparticles with three compositions. Figure 3.1b, f, and j are high-resolution TEM images showing the lattices from the [110] zone axis (octahedra sitting on a (110) edge). The HRTEM images show that all the nanoparticles are single crystalline with (111) facets exposed on their alloyed surface. HRTEM images of core-shell nanoparticles display the lattices of both the Au cores and the PdPt alloy shells (Figures 3.1d, h, and l). The PdPt shells are conformal, single

74

crystalline alloys, and epitaxial to the Au cores. A slight expansion of the shell lattice can be seen due to the Au core. Energy dispersive x-ray spectroscopy (EDX) was carried out to investigate the elemental distribution in the nanoparticles (Figure 3.2). Pd to Pt ratios of alloy nanoparticles and alloy shells are controlled to be similar (Tables 3.1 and 3.2).
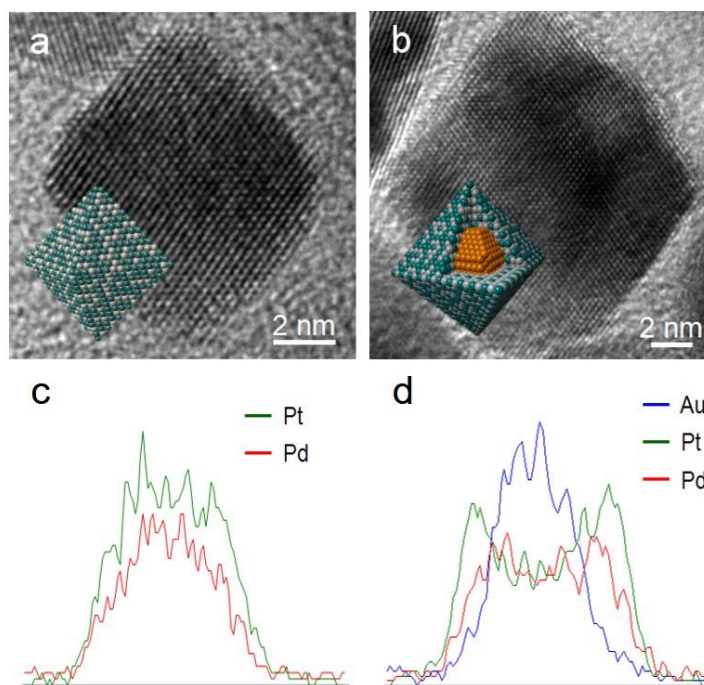

Figure 3.2 TEM images and TEM-EDX line-scanning analysis on (a,c) an octahedral Pd_1Pt_3 alloy and (b,d) Au@Pd_1Pt_3 core-shell octahedral nanoparticles.

Molar Ratio (Pd^{2+} : Pt^{2+})	Pd (atomic %)	Pt (atomic %)	Composition
3:1	19.39	7.56	$Pd_{2.6}Pt_{1.0}$
1:1	13.45	13.12	$Pd_{1.0}Pt_{1.0}$

1:3	5.60	13.10	$Pd_{1.0}Pt_{2.4}$

Table 3.1 EDX-analyzed composition of octahedral alloy NPs.

Molar Ratio (Pd^{2+} : Pt^{2+})	Pd (atomic %)	Pt (atomic %)	Composition
3:1	20.08	7.39	$Au@Pd_{2.7}Pt_{1.0}$
1:1	18.18	14.22	$Au@Pd_{1.3}Pt_{1.0}$
1:3	6.03	15.12	$Au@Pd_{1.0}Pt_{2.5}$

Table 3.2 EDX-analyzed composition of core-shell NPs.

3.4 Varying Shell Thickness

To investigate the degree of lattice strain at the alloy surface, we have tuned the strain by preparing $Au@Pd_1Pt_3$ nanoparticles with thinner and thicker shells (see experimental section). Three $Au@Pd_1Pt_3$ core-shell samples of shell thicknesses of 1.3 nm, 2.3 nm, and 3.5 nm (Figure 3.5) show a Pd to Pt ratio of 1.0:2.9, 1.0:2.5, and 1.0:2.5, respectively (Table 3.3). Shell thicknesses are calculated based on the initial size of the Au core and the final size of the Au-PdPt core-shell nanoparticle. EDX line scanning was also performed (Figure 3.2c, d) and agrees well with the assigned thicknesses. The alloy nanoparticles have an octahedral shape regardless of shell thickness (Figure 3.4).
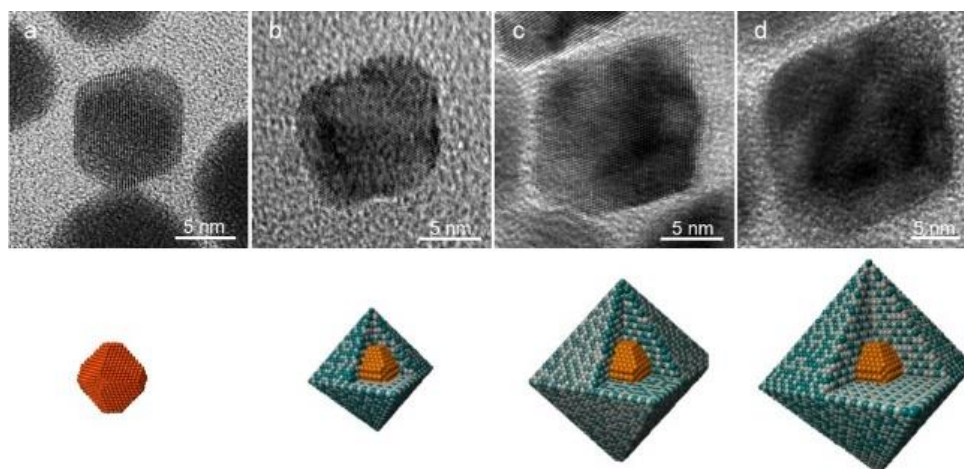
Figure 3.3 TEM images showing a) Au cores and PdPt shells of different thicknesses, b) 1.3 nm, c) 2.3 nm, and d) 3.5 nm.

Thickness (nm)	Pd (atomic %)	Pt (atomic %)	Composition
1.3	1.80	5.21	Au@Pd$_{1.0}$Pt$_{2.9}$
2.3	6.03	15.12	Au@Pd$_{1.0}$Pt$_{2.5}$
3.5	3.34	8.23	Au@Pd$_{1.0}$Pt$_{2.5}$

Table 3.3 EDX-analyzed composition of Au-Pd$_1$Pt$_3$ core-shell octahedral nanoparticles with different shell thicknesses.
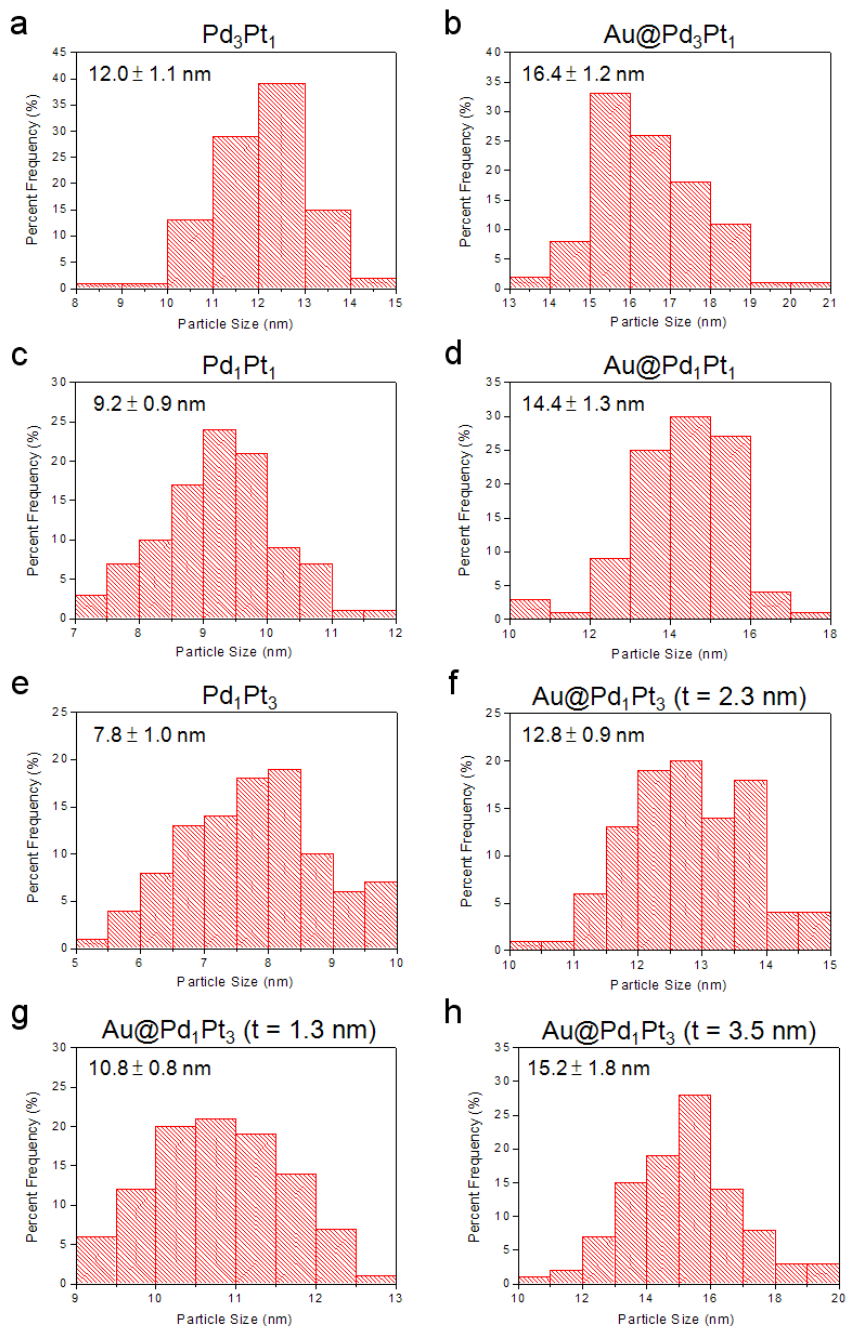
Figure 3.4 Size dispersions of alloy and core-alloyed shell nanoparticles. (a, c, e) PdPt alloy and

(b, d, f) Au-PdPt core-alloyed shell nanoparticles, with (f-h) representing the Au-Pd_1Pt_3 core-shell

nanoparticles with different thicknesses.

To estimate lattice strain, synchrotron-based x-ray diffraction (XRD) with an x-ray wavelength of 1.0332 Å was performed. For comparison, we also included the Pd_1Pt_3 alloy nanoparticles. Figure 3.5 includes the (220) peaks of the XRD patterns of Pd_1Pt_3 alloy and $Au@Pd_1Pt_3$ core-shell nanoparticles within the range from 41° to 45°. In this range, there are two peaks for $Au@Pd_1Pt_3$ core-shell nanoparticles but only one for Pd_1Pt_3 alloy nanoparticles. Peaks located around 42° are attributed to the Au cores and peaks located between 43° and 44° correspond to the Pd_1Pt_3 alloy shells. There is a clear trend of peaks shifting from 43.49° to 43.98° for the samples with different thicknesses. This shift indicates that the (220) d-spacing of the alloy exhibits a lattice expansion from 0.1380 nm to 0.1394 nm with decreasing thickness.
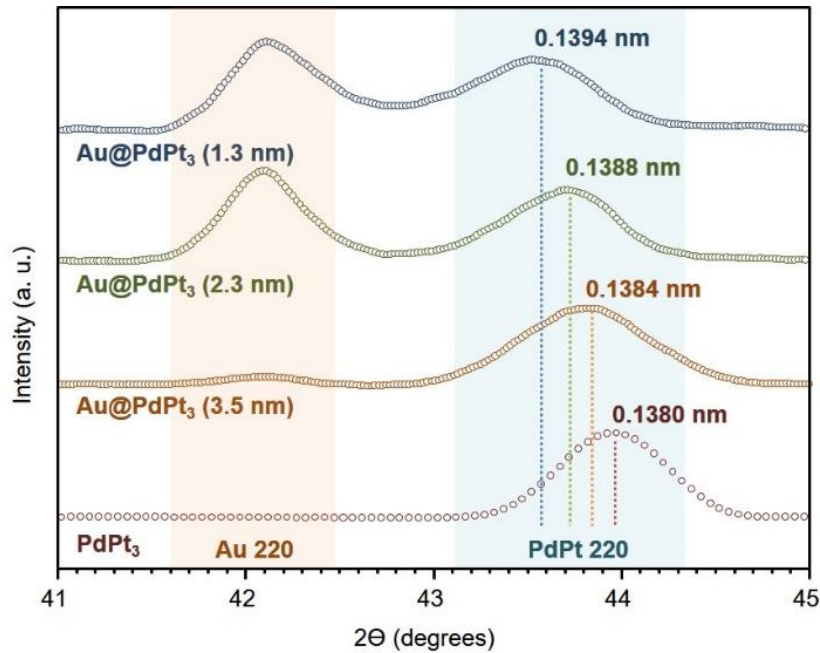

Figure 3.5 Synchrotron-based XRD patterns of the (220) peaks of Pd_1Pt_3 alloy and $Au@Pd_1Pt_3$ core-alloyed shell nanoparticles with three different shell thickness. The wavelength of the synchrotron x-ray incident on the samples is 1.0332 Å. The broad peaks between 43° and 44°

represent the (220) peak of the Pd_1Pt_3 alloy (shell), which shifts to the left as shell thickness decreases.

Pd[a]	**Pt**[b]	**$Pd_1Pt_{2.4}$** (7.8 nm)		**Au-$Pd_1Pt_{2.5}$** (3.5 nm)		**Au-$Pd_1Pt_{2.5}$** (2.3 nm)		**Au-$Pd_1Pt_{2.9}$** (1.3 nm)	
$a°_{Pd}$	$a°_{Pt}$	$a°_{PdPt}$[c]	a_{PdPt}[d]	$a°_{PdPt}$	a_{PdPt}	$a°_{PdPt}$	a_{PdPt}	$a°_{PdPt}$	a_{PdPt}
3.867	3.920	3.904	3.903	3.905	3.915	3.905	3.925	3.906	3.940
		δ_S[e] $= -0.02$ %		$\delta_S = 0.26$ %		$\delta_S = 0.51$ %		$\delta_S = 0.87$ %	

Table 3.4 Lattice parameters and strain of Pd, Pt, Pd_1Pt_3 alloy, and Au-Pd_1Pt_3 core-shell NPs with different shell thicknesses. All lattice parameters are given in Å. *a,b* Lattice parameters $a°_{Pd}$ and $a°_{Pt}$ are taken from x-ray diffraction database no. 87-0645 and no. 87-0646. *c* $a°_{PdPt}$ of the alloy Pd_xPt_{1-x} is the estimated lattice parameter from Vegard's law, where $a°PdPt$ is the sum of (x) $a°_{Pd}$ and $(1-x)a°_{Pt}$. *d* a_{PdPt} is the experimental lattice parameter obtained from the (220) peaks in synchrotron-based XRD patterns. *e* δ_S is lattice strain calculated by $[(a_{PdPt} - a°_{PdPt})/ a°_{PdPt}] \times 100$ (%).

Using these lattice parameters (Table 3.4), we estimated lattice strain (δ_s). $a°_{PdPt}$ is the estimated lattice parameter of the alloy obtained from Vegard's law, in which the lattice parameter $a°_{AB}$ of a homogeneous alloy A_xB_{1-x} is the sum of $xa°_A$ and $(1-x)a°_B$. a_{PdPt} is the experimental value of the lattice parameter. Lattice strain, δ_s, is obtained by comparing the difference between $a°_{PdPt}$ and a_{PdPt}, representing the variation in surface atomic arrangement due to the strain force. For Au@Pd_1Pt_3, the thinner the shell, the larger the lattice strain. The estimated number of Pd_1Pt_3

atomic layers in the Au@Pd$_1$Pt$_3$ samples is about 5 (t = 1.3 nm), 10 (t = 2.3 nm), and 15 (t = 3.5 nm). Fewer atomic layers in the shell allow for more surface influence from lattice mismatch at the interface of Au core and alloy shell. Strain shrinks as atomic layers increase because the surface becomes farther and farther away from the source of the lattice mismatch. It should be noted that changes in overall particle size can also effect surface lattice strain; however, this effect is strong in particularly small (<3 nm) nanoparticles.[36] Over the size range studied here, these effects should be negligible compared to strain induced by the Au core.[37]

3.5 Conclusion

In conclusion, to study the lattice strain effect on the alloyed nanoparticle surface, we have synthesized well-controlled Pd$_x$Pt$_y$ alloyed octahedral nanoparticles and Au@Pd$_x$Pt$_y$ core-alloyed shell nanoparticles of ~10 nm. We have then changed the thickness of the alloy shell to tune the lattice strain and used synchrotron-based XRD to quantify strain. The synchrotron results suggest that strain is indeed dependent on shell thickness, suggesting that the synthesized core-shell NPs are promising candidates for the identification of the impact of lattice strain on catalysis, and their performance (and its relation to surface structure) are discussed in detail in Chapter 4.

Materials and Methods

Materials

Palladium (II) chloride (PdCl$_2$, 99 %, Sigma Aldrich), potassium tetrachloroplatinate (II) (K$_2$PtCl$_4$, ≧99 %, Sigma Aldrich), gold (III) chloride hydrate (HAuCl$_4$, 99.99%, Sigma Aldrich), cetyltrimethylammonium bromide (CTAB, 98 %, CALBIOCHEM), cetyltrimethylammonium

chloride (CTAC, 95 %, TGI), sodium citrate tribasic dehydrate ($C_6H_5Na_3O_7 \cdot 2H_2O$, Sigma Aldrich, 99.5 %) were all used without further purification. Ultrapure distilled and deionized water (18.2 MΩ) was used for all solution preparations. Ultrapure Argon (Ar, Airgas) and carbon monoxide (CO, Airgas) were used during the synthesis.

Synthesis

PdPt Alloy Octahedra: Octahedral Pd-Pt alloy nanoparticles were prepared by a one-pot hydrothermal method in aqueous solution. A pressure vessel containing 28.988 mL of deionized water and 123.75 mg CTAB was sonicated until the mixture became transparent, indicating the surfactant was completely dissolved. Then, 0.375 mL of 0.01 M H_2PdCl_4 solution (3.75×10^{-3} mmol) and 0.375 mL of 0.01 M K_2PtCl_4 solution (3.75×10^{-3} mmol) were added. The total molar number of Pd^{2+} and Pt^{2+} ions are 7.5×10^{-3} mmol. After bubbling with Ar for 30 min, 0.142 mL of 0.1 M sodium citrate solution was added into the resulting salmon-pink-colored solution. The pressure vessel was then placed and heated at 110 °C for 22 h in the oven. The resulting light-brown-colored solution was cooled down to room temperature and the products were collected by centrifugation at 12000 rpm three times. To adjust alloy composition, the molar ratio of H_2PdCl_4:K_2PtCl_4 was changed to 1:3 and 3:1, but the total molar number of Pd^{2+} and Pt^{2+} ions were kept the same (7.5×10^{-3} mmol).

Au seeds: Spherical gold seeds (sub-10 nm) were prepared by a one-pot hydrothermal method in the aqueous phase. First, 270 mg CTAB was dissolved in 48.513 mL of deionized water. Then, 1.25 mL of 0.01 M $HAuCl_4$ and 0.237 mL of 0.1 M sodium citrate were added into the clear transparent solution, followed by bubbling carbon monoxide for 30 min. The bright-orange

solution in a pressure vessel was heated at 110 °C for 22 h and a red-violet-colored solution was obtained.

Au@PdPt core-shell octahedra: In a typical synthesis of octahedral Au@PdPt core-shell nanoparticles, a pressure vessel containing 25.988 mL of deionized water, 123.75 mg CTAB was sonicated until it became transparent. Once the surfactant was dissolved, 3.0 mL of Au-seed solution (7.5×10^{-4} mmol of Au atoms) was added, followed by the further addition of 0.375 mL of 0.01 M H_2PdCl_4 solution and 0.375 mL of 0.01 M K_2PtCl_4 solution. After bubbling with Ar for 30 min, 0.142 mL of 0.1M sodium citrate solution was added into the resulting pale-violet color cloudy solution. The vessel was then heated at 110 °C for 22 h in the oven. The resulting brown-colored solution in a pressure vessel was cooled down to room temperature and the products were collected via centrifugation at 12000 rpm for redispersion in water, where this rinsing was then repeated for a total of three cycles. To make Au@Pd_1Pt_3 nanoparticles of which shell thickness is 2.6, 4.6, and 7.0 nm, total molar number of 1.5×10^{-3}, 7.5×10^{-3}, and 1.125×10^{-2} mmol of H_2PdCl_4 and K_2PtCl_4 were used in a constant Pd^{2+}/Pt^{2+} ratio equal to 1/3.

Characterization

Sample Preparation. For TEM analysis, the synthesized nanoparticles were concentrated into 0.5 mL of solution. The solution color was dark brown. Taking one TEM grid (TED PELLA, INC. Lacey Carbon Type-A) with tweezers (Electron Microscopy Sciences Dumoxel - Tweezers), 5 μL of sample solution were dropped onto the grid center and left to dry. For the EDX measurement, the same TEM sample grids were used. For synchrotron-based XRD measurements, the sample solution containing nanoparticles was concentrated into ~0.1 mL. The colloid was thick and brownish-black in color. Silicon wafers were used as substrates for SEM and 20 μL of the sample solution dropped onto these and left for drying.

Instrumentation. Scanning electron microscopy (SEM) images of the samples were obtained using a JEOL JSM 6340F electron microscope. TEM, including HRTEM and EDX studies were performed on a JEOL JEM 2010F electron microscope operating at 200 keV. An x-ray of 1.0332 Å from synchrotron radiation monochromatized by Si(111) crystal was used for diffraction. The growth solution was heated using a Thermo Scientific Lindberg Blue M oven. The particles were collected by using Thermo Scientific Sorvall Legend X1R Centrifuge and Eppendorf Centrifuge 5424.

References

1.   Strasser, P.; Koh, S.; Anniyev, T.; Greeley, J.; More, K.; Yu, C. F.; Liu, Z. C.; Kaya, S.; Nordlund, D.; Ogasawara, H.; Toney, M. F.; Nilsson, A., Lattice-strain control of the activity in dealloyed core-shell fuel cell catalysts. *Nat. Chem.* **2010,** *2* (6), 454-460.

2.   Debe, M. K., Electrocatalyst approaches and challenges for automotive fuel cells. *Nature* **2012,** *486* (7401), 43-51.

3.   Narayanan, R.; El-Sayed, M. A., Shape-Dependent Catalytic Activity of Platinum Nanoparticles in Colloidal Solution. *Nano Lett.* **2004,** *4* (7), 1343-1348.

4.   Shao, M.; Chang, Q.; Dodelet, J.-P.; Chenitz, R., Recent Advances in Electrocatalysts for Oxygen Reduction Reaction. *Chem. Rev.* **2016,** *116*, 3594.

5.   Sui, S.; Wang, X.; Zhou, X.; Su, Y.; Riffat, S.; Liu, C.-J., A comprehensive review of Pt electrocatalysts for the oxygen reduction reaction: Nanostructure, activity, mechanism and carbon support in PEM fuel cells. *J. Mater. Chem. A* **2017,** *5*, 1808.

6.   Grozovski, V.; Solla-Gullon, J.; Climent, V.; Herrero, E.; Feliu, J. M., Formic Acid Oxidation on Shape-Controlled Pt Nanoparticles Studied by Pulsed Voltammetry. *J. Phys. Chem. C* **2010,** *114* (32), 13802-13812.

7.   Huang, M. H.; Lin, P. H., Shape-Controlled Synthesis of Polyhedral Nanocrystals and Their Facet-Dependent Properties. *Adv. Funct. Mater.* **2012,** *22* (1), 14-24.

8.   Chiu, C. Y.; Chung, P. J.; Lao, K. U.; Liao, C. W.; Huang, M. H., Facet-Dependent Catalytic Activity of Gold Nanocubes, Octahedra, and Rhombic Dodecahedra toward 4-Nitroaniline Reduction. *J. Phys. Chem. C* **2012,** *116* (44), 23757-23763.

9.   Chen, Y. H.; Hung, H. H.; Huang, M. H., Seed-Mediated Synthesis of Palladium Nanorods and Branched Nanocrystals and Their Use as Recyclable Suzuki Coupling Reaction Catalysts. *J. Am. Chem. Soc.* **2009,** *131* (25), 9114-9121.

10.   Laskar, M.; Skrabalak, S. E., Decoupling the Geometric Parameters of Shape-Controlled Pd Nanocatalysts. *ACS Catal.* **2014,** *4* (4), 1120-1128.

11.   Huang, M. H.; Rej, S.; Hsu, S.-C., Facet-depedet properties of polyhedral nanocrystals. *Chem. Commun.* **2014,** *50,* 1634.

12.   Liu, L.; Corma, A., Metal Catalysts for Heterogeneous Catalysis: From Single Atoms to Nanoclusters and Nanoparticles. *Chem. Rev.* **2018,** *118*, 4981.

13.   Cui, C. G., L; Li, H; Yu, S; Heggen, M; Strasser, P, Octahedral PtNi Nanoparticle Catalysts: Exceptional Oxygen Reduction Activity by Tuning the Alloy Particle Surface Composition. *Nano Lett.* **2012,** *12*, 5885-5889.

14.   Choi, S.-I.; Xie, S.; Shao, M.; Odell, J. H.; Lu, N.; Peng, H.-C.; Protsailo, L.; Guerrero, S.; Park, J.; Xia, X.; Wang, J.; Kim, M. J.; Xia, Y., Synthesis and Characterization of 9 nm Pt–Ni Octahedra with a Record High Activity of 3.3 A/mgPt for the Oxygen Reduction Reaction. *Nano Lett.* **2013,** *13* (7), 3420-3425.

15.   Zhang, N.; Bu, L.; Guo, S.; Guo, J.; Huang, X., Screw Thread-Like Platinum-Copper Nanowires Bounded with High-Index Faces for Efficient Electrocatalysis. *Nano Lett.* **2016,** *16* (8), 5037-5043.

16.   Bu, L.; Zhang, N.; Guo, S.; Zhang, X.; Li, J.; Yao, J.; Wu, T.; Lu, G.; Ma, J.-Y.; Su, D.; Huang, X., Biaxially strained PtPb/Pt core/shell nanoplate boosts oxygen reduction catalysis. *Science* **2016,** *354*, 1410.

17.   Tian, N.; Zhou, Z.-Y.; Sun, S.-G.; Ding, Y.; Wang, Z. L., Synthesis of Tetrahexahedral Platinum Nanocrystals with High-Index Facets and High Electro-Oxidation Activity. *Science* **2007,** *316* (5825), 732-735.

18.   Du, P.; Wu, P.; Cai, C., Mechanistic Insight into the Facet-Dependent Adsorption of Methanol on a Pt$_3$Ni Nanocatalyst. *J. Phys. Chem. C* **2015,** *119,* 18352-18363.

19.   Wu, J.; Li, P.; Pan, Y.-T. F.; Warren, S.; Yin, X.; Yang, H., Surface lattice-engineered bimetallic nanoparticles and their catalytic properties. *Chem. Soc. Rev.* **2012,** *41*, 8066-8074.

20.   Stamenkovic, V. R.; Fowler, B.; Mun, B. S.; Wang, G. F.; Ross, P. N.; Lucas, C. A.; Markovic, N. M., Improved oxygen reduction activity on Pt$_3$Ni(111) via increased surface site availability. *Science* **2007,** *315* (5811), 493-497.

21.   Tedsree, K.; Li, T.; Jones, S.; Chan, C. W. A.; Yu, K. M. K.; Bagot, P. A. J.; Marquis, E. A.; Smith, G. D. W.; Tsang, S. C. E., Hydrogen production from formic acid decomposition at room temperature using a Ag-Pd core-shell nanocatalyst. *Nat. Nanotechnol.* **2011,** *6* (5), 302-307.

22.   Stamenkovic, V. R.; Mun, B. S.; Mayrhofer, K. J. J.; Ross, P. N.; Markovic, N. M.; Rossmeisl, J.; Greeley, J.; Norskov, J. K., Changing the activity of electrocatalysts for oxygen reduction by tuning the surface electronic structure. *Angew. Chem.* **2006,** *45*, 2897.

23.   Kulkarni, A.; Siahrostami, S.; Patel, A.; Norskov, J. K., Understanding Catalytic Activity Trends in the Oxygen Reduction Reaction. *Chem. Rev.* **2018,** *118*, 2302.

24.   Wu, J. B.; Qi, L.; You, H. J.; Gross, A.; Li, J.; Yang, H., Icosahedral Platinum Alloy Nanocrystals with Enhanced Electrocatalytic Activities. *J. Am. Chem. Soc.* **2012,** *134* (29), 11880-11883.

25.   Yang, J. H.; Yang, J.; Ying, J. Y., Morphology and Lateral Strain Control of Pt Nanoparticles via Core-Shell Construction Using Alloy AgPd Core Toward Oxygen Reduction Reaction. *ACS Nano* **2012,** *6* (11), 9373-9382.

26.   Luo, M.; Guo, S., Strain-controlled electrocatalysis on multimetallic nanomaterials. *Nat. Rev. Mater.* **2017,** *2*, 17059.

27.   Nilsson Pingel, T.; Joergensen, M.; Yankovich, A. B.; Groenbeck, H.; Olsson, E., Influence of atomic site-specific strain on catalytic activity of supported nanoparticles. *Nat. Commun.* **2018,** *9*, 1.

28.   Zhao, X.; Chen, S.; Fang, Z.; Ding, J.; Sang, W.; Wang, Y.; Zhao, J.; Peng, Z.; Zeng, J., Octahedral Pd@Pt$_{1.8}$Ni Core-Shell Nanocrystals with Ultrathin PtNi Alloy Shells as Active Catalysts for Oxygen Reduction Reaction. *J. Am. Chem. Soc.* **2015,** *137* (8), 2804-2807.

29.   Cui, C.; Gan, L.; Heggen, M.; Rudi, S.; Strasser, P., Compositional segregation in shaped Pt alloy nanoparticles and their structural behaviour during electrocatalysis. *Nat. Mater.* **2013,** *12*, 765-771.

30.   Mazumder, V.; Chi, M.; Mankin, M. N.; Liu, Y.; Metin, O.; Sun, D.; More, K. L.; Sun, S., A Facile Synthesis of MPd (M = Co, Cu) Nanoparticles and Their Catalysis for Formic Acid Oxidation. *Nano Lett.* **2012,** *12* (2), 1102-1106.

31.   Hu, S.; Che, F.; Khorasani, B.; Jeon, M.; Yoon, C. W.; McEwen, J.-S.; Scudiero, L.; Ha, S., Improving the electrochemical oxidation of formic acid by tuning the electronic properties of Pd-based bimetallic nanoparticles. *Appl. Catal. B: Environ.* **2019,** *254*, 685-692.

32.   Wang, D.; Li, Y., Bimetallic Nanocrystals: Liquid-Phase Synthesis and Catalytic Applications. *Adv. Mater.* **2011,** *23* (9), 1044-1060.

33.   Gilroy, K. D.; Ruditskiy, A.; Peng, H.-C.; Qin, D.; Xia, Y., Bimetallic Nanocrystals: Syntheses, Properties, and Applications. *Chem. Rev.* **2016,** *116*, 10414.

34.   Kuai, L.; Yu, X.; Wang, S.; Sang, Y.; Geng, B., Au–Pd Alloy and Core–Shell Nanostructures: One-Pot Coreduction Preparation, Formation Mechanism, and Electrochemical Properties. *Langmuir* **2012,** *28* (18), 7168-7173.

35.   Li, J.; Zheng, Y.; Zeng, J.; Xia, Y., Controlling the Size and Morphology of Au@Pd Core–Shell Nanocrystals by Manipulating the Kinetics of Seeded Growth. *Chem.: Eur. J.* **2012,** *18* (26), 8150-8156.

36.   An, W.; Liu, P., Size and Shape Effects of Pd@Pt Core−Shell Nanoparticles: Unique Role of Surface Contraction and Local Structural Flexibility. *J. Phys. Chem. C* **2013,** *117*, 16144-16149.

37.   Ouyang, G.; Zhu, W. G.; Sun, C. Q.; Zhu, Z. M.; Liao, S. Z., Atomistic origin of lattice strain on stiffness of nanoparticles. *Phys. Chem. Chem. Phys.* **2010,** *12*, 1543-1549.

Chapter 4

The Impact of Nanoparticle Surface Structure on Catalytic Activity
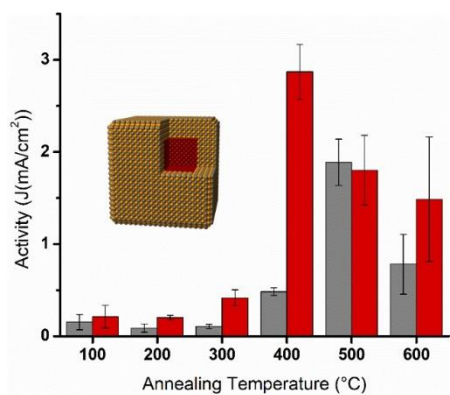
Composition
Strain
Ligand Effects
Atomic Order
Faceting
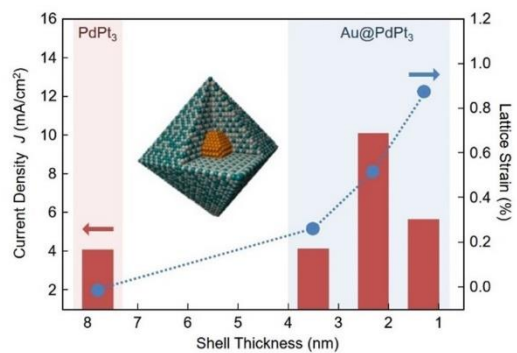
4.1 Abstract

Building on the synthetic work introduced in the previous chapters, we use a serious of small molecule oxidations to characterize the catalytic behavior of our core-shell nanostructures. Methanol oxidation serves to characterize the structural evolution of shaped Pd-(Ni-Pt)$_x$ NPs following annealing. The activity is correlated with the nanoscale mixing behavior to shed light on nanoscale mixing processes and their effect on surface structure. Core-shell Au@PdPt NPs are used as catalysts for formic acid oxidation, with a series of shell thicknesses allowing for the isolation of the impact of lattice strain on surface structure. Altogether, the results of this chapter unravel the impact of several different phenomena on nanocatalyst surface structure and their influence on catalytic activity.

4.2 Introduction

The previous chapters introduced the synthesis of two nanostructure systems with different nanoscale phenomena determining their surface structure. The layered core-shell Pd-(Ni-Pt)$_x$ structures used lattice strain to induce mixing of the shell to yield a fully mixed alloy that displayed atomic order. The low annealing temperatures allowed for the preservation of shape that maintained dominant surface faceting. In this chapter, the effect of mixing on catalytic activity will be used to further investigate the degree of mixing after annealing at each temperature and the subsequent catalytic activity of the nanocatalyst. The core-alloyed shell Au@PdPt NPs used varying shell thickness to introduce different degrees of strain at the surface. The increasing shell thickness further serves to reduce the impact of ligand effects on surface structure, as will be discussed below. Again, dominant faceting is maintained and composition is controlled. Taken together, these two systems allow for analysis of five factors that impact NP catalytic activity: composition, strain, ligand effects, atomic order, and faceting.

4.3 Probing Pd-Ni-Pt and Pd-(Ni-Pt)$_2$ Surface Structure through Methanol Oxidation

To further investigate surface structure after metallic mixing, Pd-Ni-Pt and Pd-(Ni-Pt)$_2$ annealed at each temperature introduced in Chapter 2 were tested for the alkaline methanol electro-oxidation reaction (MOR), a typical small molecule oxidation reaction with potential in fuel cell applications. Electrochemical measurements illuminate the surface electronic structure of the catalyst by testing its ability to perform desired transformations. Pt-Ni composites have been shown to display high MOR activity, as charge transfer brings the metal d-band to an optimal energy level.[1] The performance and durability of MOR catalysts can be negatively impacted by the (often irreversible) adsorption of a CO intermediate, but it has been shown that intermetallic structures are less prone to CO poisoning.[2] They are also more resistant to etching in acidic media, showcasing higher stability as a result. Each sample was loaded on Vulcan XC-72 carbon and dried under nitrogen for 24 hours. The electrochemical conversions were performed using a standard three-electrode system: Pt wire as the counter electrode, saturated calomel electrode as the reference electrode, and a glassy carbon electrode loaded with 5 µL of the synthesized nanocatalysts supported on Vulcan carbon as the working electrode. Blank scans (Figure 4.1) were performed in 0.1 M KOH with a potential sweep from -1.0 to +0.6 V. The hydrogen sorption peak is denoted by the shaded region of Figure 4.1. The integration of charge collected under this peak was used to determine the electrochemical surface area (ECSA) of the tested catalysts. The detailed procedures are outlined in Materials and Methods.
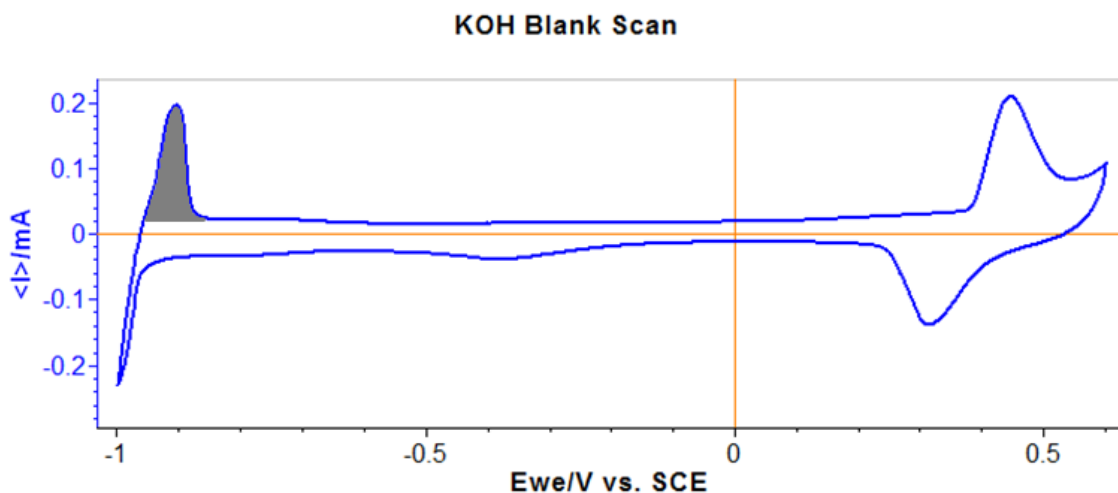
KOH Blank Scan

Figure 4.1 Representative electrochemical blank scan of Pd-(Ni-Pt)$_x$ supported on carbon.

Characteristic cyclic voltammetry (CV) scans for Pd-(Ni-Pt)$_2$ (a) and Pd-Ni-Pt (b) annealed at various temperatures are shown in Figure 4.2. The peak current densities found in these scans are used in Figure 4.3. Three scans were taken for each sample and averaged for the reported peak currents. The line shape of the Pd-Ni-Pt 400 °C sample is attributed to competition between the direct and indirect MOR pathways.
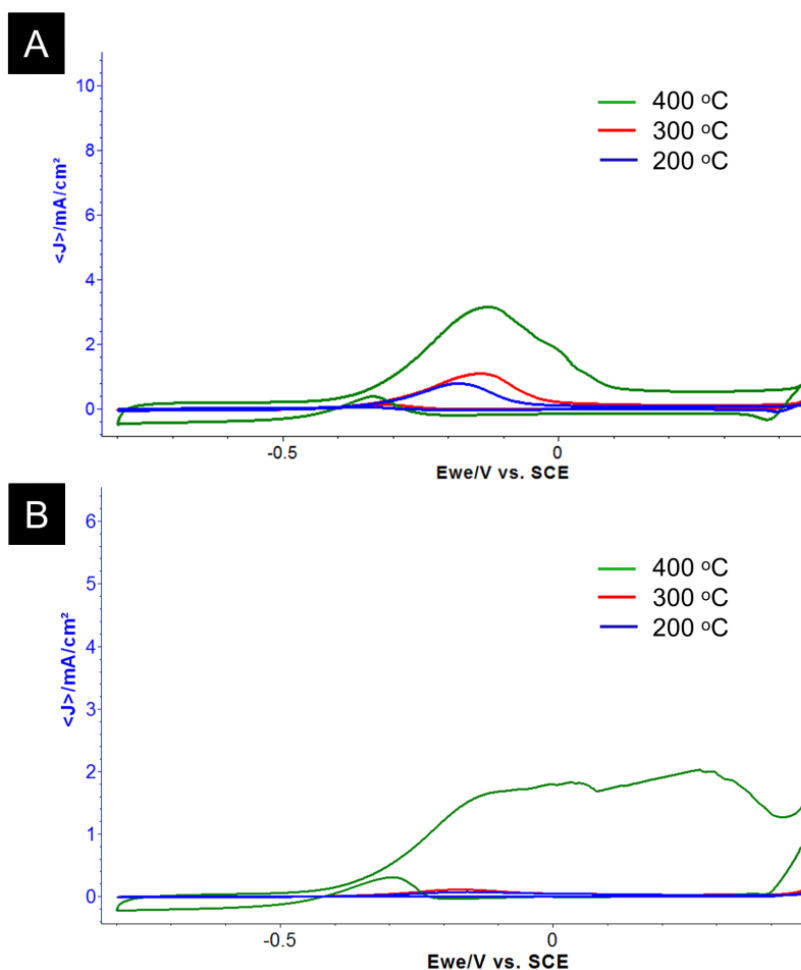
Figure 4.2 Methanol oxidation CV traces for (a) Pd-(Ni-Pt)$_2$ and (b) Pd-Ni-Pt after annealing at the listed temperatures.

From Figure 4.3, a comparison of each sample (two- and four-layered) at the designated temperatures can be seen. At 200 °C, both samples perform nominally the same as the as-synthesized samples. At 300 °C, each sample has a slight increase in activity, but the four-layered sample, with its higher lattice strain and thus greater degree of mixing, does see a somewhat larger increase. By 400 °C, as strain allows complete mixing throughout the multilayered shell, the four-layered sample has a significant jump in activity. This complete mixing can be seen in the lattice

spacing measurements (Figure 2.7), and the mixed shell yields a more active surface. However, at the same temperature, the two-layered sample has only a minor increase in activity, on par with the four-layered sample at 300 °C, as it is only partially mixed, which we attribute to the lesser strain in its thicker layers. We moved to higher temperatures to see if we could induce the same degree of migration in the two-layered sample as seen in the four-layered. By 500 °C, a larger jump in activity is observed, though it does not reach the peak activity of the Pd-(Ni-Pt)$_2$ structure. The four-layered sample, meanwhile, decreases in activity.
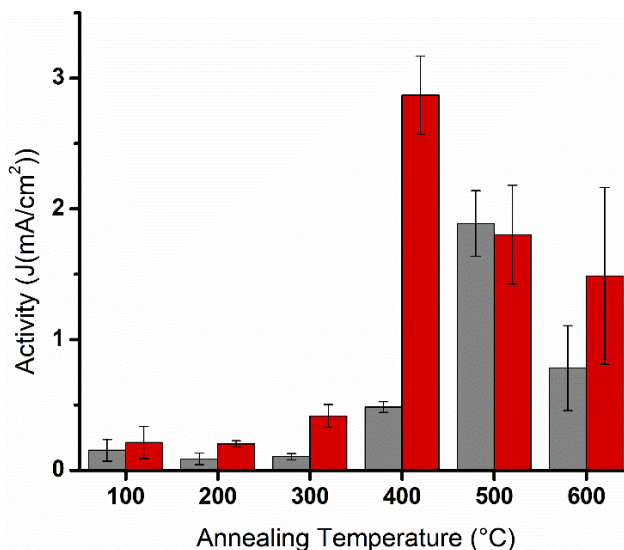

Figure 4.3 Electrochemical activity for methanol oxidation catalyzed by Pd-Ni-Pt and Pd-(Ni-Pt)$_2$ NPs annealed at various temperatures. Grey bars represent the two-layered Pd-Ni-Pt and red bars represent the four-layered Pd-(Ni-Pt)$_2$.

The lower peak activity of the two-layered catalyst and deactivation of the four-layered catalyst is attributed to the degradation of the sample at such high annealing temperatures. As

mentioned before TEM results show surface deformation of the Pd-Ni-Pt NPs. Further, Ni leaching and Pd migration into the Pt phase can be seen (Figure 4.4). In the top line of Figure 4.4, migration of the Pd core to the surface can be seen. In the bottom line, leaching of the Ni and formation of a PdPt alloy can be seen. Activity is further decreased by annealing at 600 °C. Each sample and temperature profile was run in triplicate, leading to the error bars depicted. We again attribute the large error bars at high temperatures to sample degradation at these high temperatures, which is not a reproducible process. Moreover, the change in the surface structure also causes breaks in the consistency of the active sites, which would also lead to a higher degree of error.
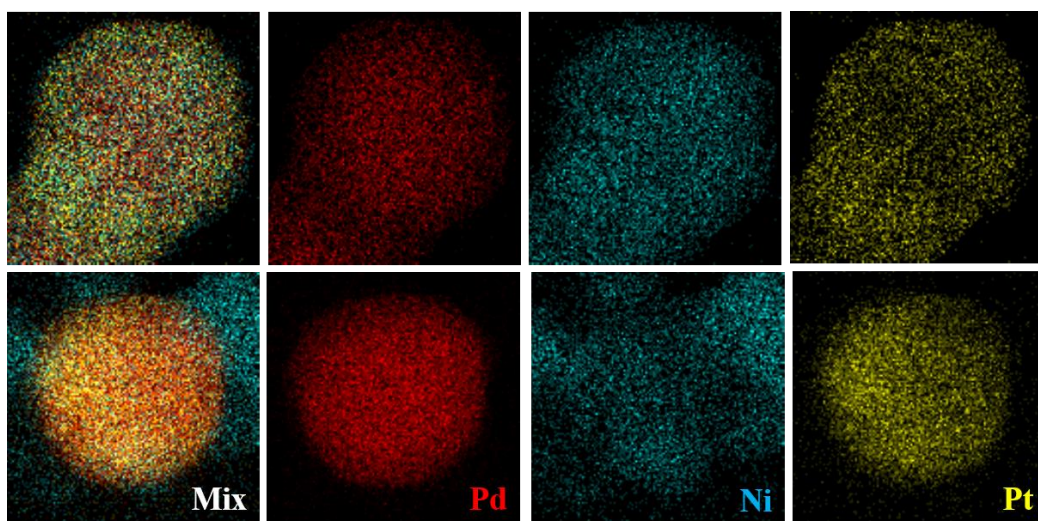

Figure 4.4 EDX analysis showing degradation of Pd-Ni-Pt after annealing at 500 °C.

The temperatures chosen for IMC synthesis beg two questions: First, is the annealing time of one-hour ideal for the mixing process? Perhaps a longer annealing time at a lower temperature could prevent aggregation and preserve fidelity to the initial cubic NP shape. Second, can the Pd-Ni-Pt NPs achieve an activity comparable to the Pd-$(Ni-Pt)_2$ NPs if given more time to mix? These questions were addressed using extended time studies, annealing the NPs for longer times at each temperature, as shown in Figure 4.5.
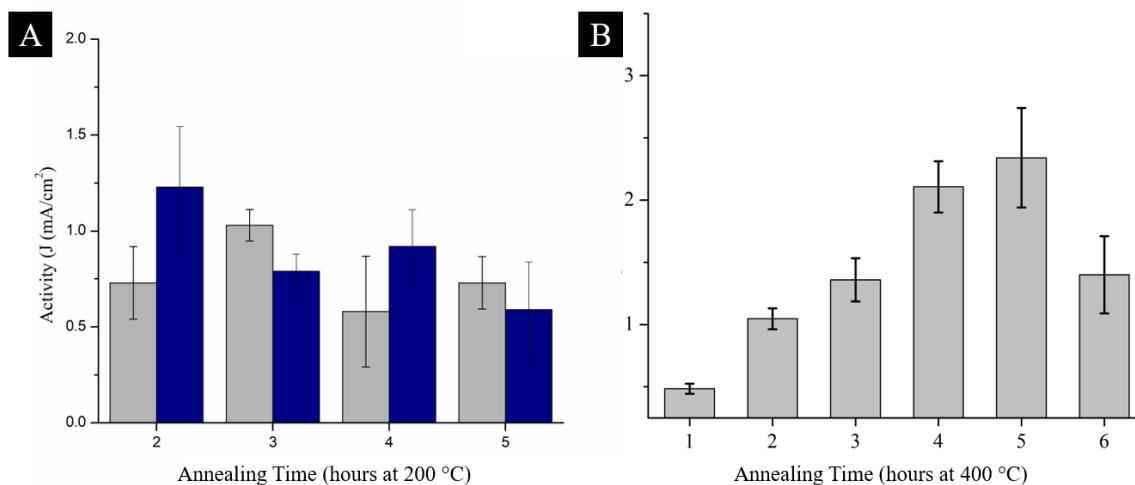
Figure 4.5 Extended annealing time studies displaying the MOR activities of Pd-Ni-Pt (grey) and Pd-(Ni-Pt)$_2$ (blue) NPs annealed at (a) 200 °C or, for Pd-Ni-Pt, (b) 400 °C for various amounts of time.

Annealing for longer than one hour at 200 °C appears to have little effect on the catalytic activity, for both the Pd-Ni-Pt and Pd-(Ni-Pt)$_2$ NPs, implying that the low annealing temperature is unable to overcome the kinetic barriers associated with mixing, irrespective of the annealing time. This experiment agrees well with our DFT results and supports the need to increase annealing temperatures in order to induce metallic mixing. The extended annealing at 400 °C shows two distinct effects for the Pd-Ni-Pt and Pd-(Ni-Pt)$_2$ NPs. For Pd-(Ni-Pt)$_2$, extending the annealing time to two hours led to no change in activity, so further studies were not carried out. This result makes sense, as the outer shell is already fully mixed after 1 h. For Pd-Ni-Pt, activity continues to increase up to a five-hour annealing time. This result suggests that, given enough time, the thicker Ni and Pt layers can achieve mixing similar to the thinner layers in Pd-(Ni-Pt)$_2$. After more than

five hours, the activity decreases, which we attribute to surface roughening and sintering after such a long annealing process at high temperature.

The activity of the mixed Pd-Ni-Pt and Pd-(Ni-Pt)$_2$ nanocatalysts reinforces the differences in mixing behavior between the two- and four-layered nanostructures. It suggests that the strain introduced by the four-layered structure allows for mixing at low annealing temperatures that preserve an active catalytic surface. Even the relatively slight increase in diffusion lengths and decrease in strain in the Pd-Ni-Pt structure escalates the mixing barriers to the point that annealing temperatures are required that damage the nanocatalyst structure. Overall, the Pd-(Ni-Pt)$_2$ structure sheds light on the energetic barriers of nanoscale metallic mixing and offers a promising structural example of an effective precursor to shaped IMC NPs.

4.4 Activity for Formic Acid Oxidation

Formic acid is a good choice for chemical fuel cells due to its high energy density (1740 Wh/kg) and ease of storage.[3] It is generally accepted that there are possible direct and indirect FOR pathways.[4-6] In the direct pathway, the removal of hydrogen happens either from the C-H bond or the O-H bond of HCOOH, followed by oxidation on the catalyst surface to generate CO_2. The indirect pathway is known as the non-Faradaic (i.e. without electron flow) dehydrogenation of formic acid, in which activated CO_{ads} is produced first and then further oxidized to form CO_2. It was found that the current density of both pathways is highly dependent on the metal surface structure; therefore, FOR is a sensitive probe to test the surface of Pt-based nanoparticles.[5-7]
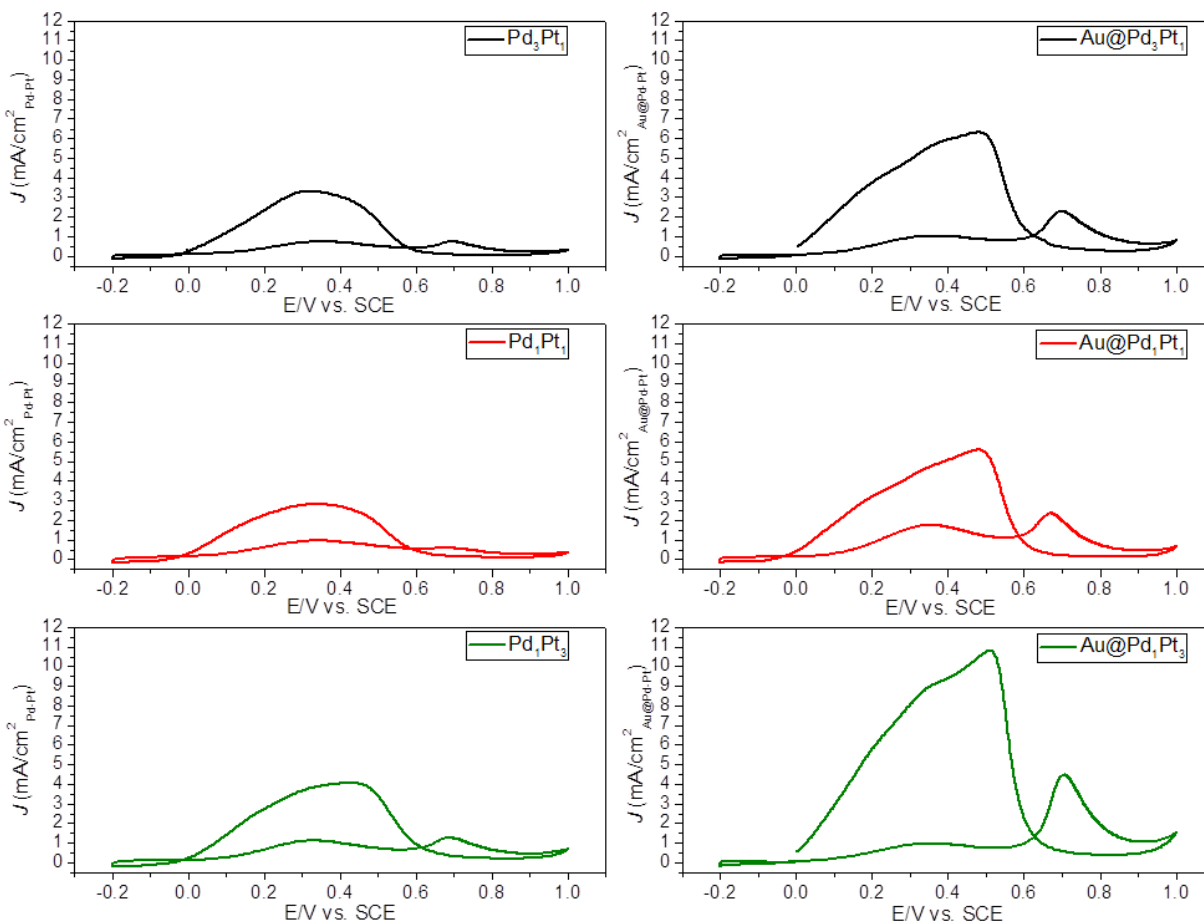
Figure 4.6 Formic acid oxidation cyclic voltammograms for Pd_xPt_y and $Au@Pd_xPt_y$ NPs.

Polarization curves indicate that the FOR on our alloy and core-shell nanoparticles follows the indirect pathway (Figure 4.6). Cyclic voltammograms were taken in a solution of 1 M H_2SO_4 and 1 M formic acid, sweeping at 100 mV/s from -0.2 V to +1.0 V. In the cathodic scan, the peak between 0.6 V and 0.0 V represents the oxidation of CO_{ads}. Current is normalized by the ECSA estimated by the integrated reduction charge of surface palladium oxide. Figure 4.7 summarizes the cathodic scan current densities of alloy and core-shell nanoparticles. It shows that alloying has altered the activity;[8] however, the influence of the Au core is more significant as all the core-shell nanoparticles have higher current density than their alloy counterparts. This result suggests that

the Au core has a large impact on the alloy surface, which we believe originates from lattice strain caused by lattice mismatch between the Au core and PdPt shell. Differences in activity between the core-shell structures are attributed to differences in composition, as they follow a similar trend to that seen for the pure PdPt nanostructures. It should be noted that there could be slight differences in lattice strain among the core-shell structures due to the variation in composition, but these should be slight due to the similar lattice constants of Pd and Pt and thicknesses of the alloy shells.
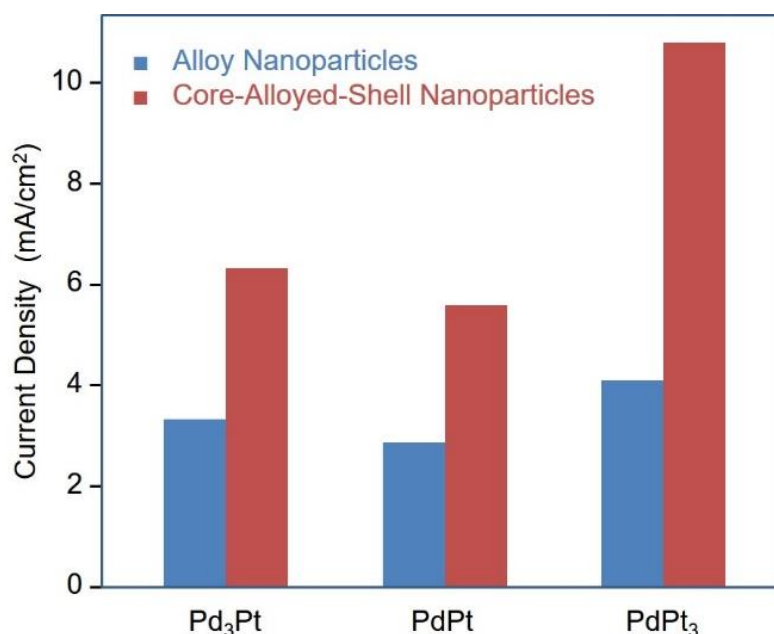

Figure 4.7 Current density of FOR on PdPt alloy and Au@PdPt core-alloyed shell octahedral nanoparticles with different Pd:Pt ratios but similar thicknesses.

4.5 The Effect of Lattice Strain on FOR Activity

The core-alloyed NPs with varied shell thickness were also tested for the FOR. CVs are shown in Figure 4.8. Conditions are the same as described above. The peak current density for

each shell thickness can be seen in Figure 4.9. The activity of pure Pd_1Pt_3 alloyed nanoparticles is included for comparison. In all cases, the Au core increases the current density of the cathodic scans; however, the increase from Pd_1Pt_3 to $Au@Pd_1Pt_3$ with a thick, 3.5 nm shell is negligible, rising only from 4.09 to 4.11 mA/cm^2. When that thickness is reduced to 2.3 nm, on the other hand, a large jump in current density, to 10.08 mA/cm^2, is seen. As mentioned earlier, we attribute this upturn to the effect of increased lattice strain on the surface that raises the d-band center. For the thin, 1.3 nm shell, though, the current density is decreased back to 5.65 mA/cm^2. We note that this need for optimized structure has been observed in many catalysis studies and indicates that the alloy surface is indeed sensitive to the fine structure of the nanoparticles.
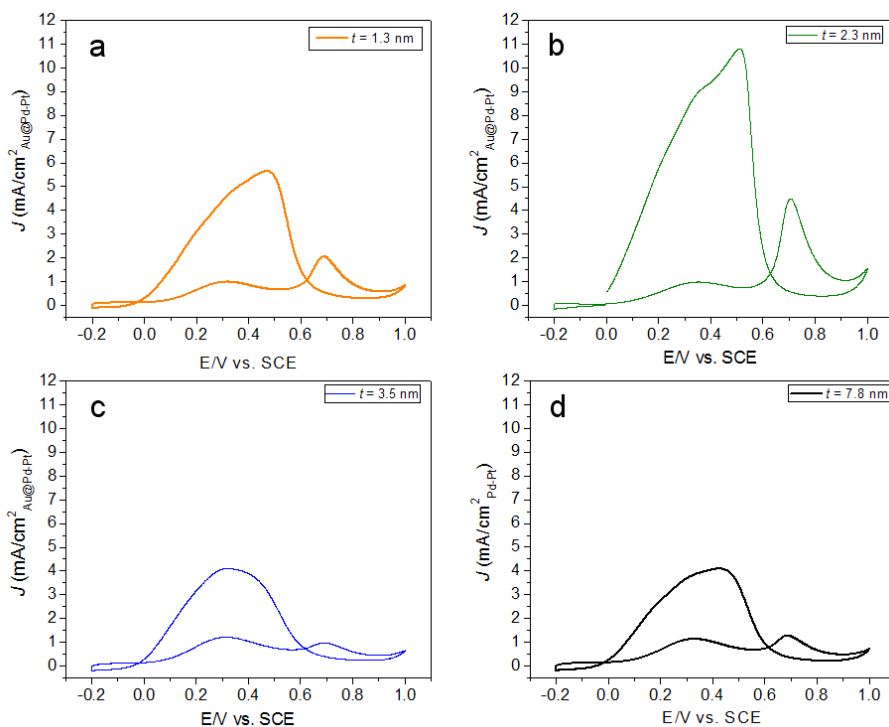

Figure 4.8 Polarization curves of formic acid oxidation on Au-Pd_1Pt_3 core-shell nanoparticles with thickness (a) 1.3 nm, (b) 2.3 nm, (c) 3.5 nm, and Pd_1Pt_3 alloy nanoparticles with size (d) 7.8 nm.
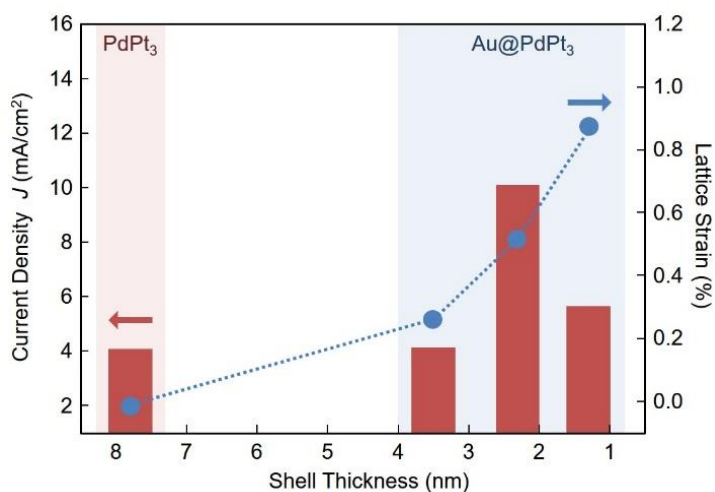
Figure 4.9 The relation of lattice strain, current density, and thickness of Pd_1Pt_3 alloy domains.

There are two potential reasons for this relationship. One possible reason is that when strain is too high, as in the case of the thin shell, the surface lattice strain is relaxed by the formation of surface defects, sapping its catalytic activity. Another explanation could be the influence of the ligand effect. The ligand effect is mainly caused by charge transfer as electron density is transferred from a metal with a higher Fermi level to a metal with a lower Fermi level.[9] This increased filling results in a lowering of the shell's d-band center and a decrease in FOR activity. Lattice strain imparted by Au, on the other hand, raises the d-band center, increasing FOR activity. In the thinnest shell's case, the ligand effect is strong, and charge transfers from the core to the shell, increasing the shell's d-band filling and offsetting the strain effect. When the Pd_1Pt_3 shell becomes sufficiently thick ($t = 2.3$ nm), the strain effect dominates over the ligand effect, resulting in high activity. When the shell is very thick ($t = 3.5$ nm), neither effect is strong and the particles show similar activity to the bimetallic alloy Pd_1Pt_3 with no core.

4.6 Conclusion

Overall, the catalytic studies presented in this chapter serve to identify the impact of several nanoscale phenomena on surface structure and the resulting impact on activity. In the Pd-(Ni-Pt)$_x$ system, metallic mixing induces the migration of Ni to the Pt surface, increasing activity for the MOR. Annealing of the layered structure represents a promising route to shaped IMC nanocatalysts, introducing atomic order that allows for tailoring catalytic sites and induces high activity in Pd-(Ni-Pt)$_2$ NPs annealed at a relatively mild 400 °C. For Au@PdPt, manipulation of the alloy shell thickness allows for isolation of the effect of lattice strain on the catalytic surface. The high activity of the shell of medium thickness suggests that the balance between strain and the ligand effect must be considered when designing multilayered nanocatalysts.

Methods

Electrochemical Measurements

Pd-Ni-Pt and Pd-(Ni-Pt)$_2$

The Pd-Ni-Pt and Pd-(Ni-Pt)$_2$ nanoparticle catalysts were loaded onto carbon black (Vulcan XC-72) by adding $\sim$ 3.25 mg directly to the nanoparticle ink solution, sonicated briefly and then dried overnight. The nanoparticle on carbon samples were then calcined at the appropriate temperature to be used for electrochemical measurements. For the as-synthesized samples, they were loaded on carbon and dried, then used. The carbon black with nanoparticle loading was added to a vial and diluted to $\sim$500 μL and 5 μL dropped directly onto a glassy carbon working electrode (CH Instruments) allowed to dry followed by a second 5 μL drop for cyclic voltammetry (CV). The CV was performed using a BioLogic VSP potentiostat in a typical three-electrode system; a saturated calomel electrode was used as the reference electrode and a platinum wire as the counter electrode

(both also obtained from CH Instruments). Blank scans were run in 0.1 M KOH which was purged with nitrogen. The CV cycle was scanned from –1.0 to 0.6 V at a scan rate of 50 mV/s until stabilization of the hydrogen sorption/desorption peak was reached, usually after ~20 cycles. The electrochemically active surface area was determined by the total charge collected from the hydrogen peak divided by the charge per area required to remove a layer of hydrogen from the Pt surface ($210 \mu C/cm^2$). For the alkaline electrooxidation of methanol, a 0.5M solution of methanol in 0.1M KOH was purged with nitrogen. This solution was cycled from –0.8 to 0.6 V at a scan rate of 50 mV/s until a decrease in activity was observed. Electrochemical measurements on the $PdNi_{1.5}Pt_{0.5}/C$ catalysts were performed in the same manner.

PdPt and Au@PdPt

A three-electrode cell system was utilized to measure the electrochemical properties. A glassy carbon electrode was used as the working electrode and first polished with 0.3 micron micropolish powder (CH Instruments, Inc.). A saturated calomel electrode (SCE) and a platinum wire were used as a reference and counter electrode, respectively. First, blank scans were performed in N_2-saturated fresh 0.5 M H_2SO_4 solution with the potential scanned in the range from -0.2 V to 1.0 V in order to clean the surface of the working electrode with catalyst. In a typical measurement, the blank scan without catalyst was continued through around 10-20 cycles. Then, the working electrode was taken out from the solution and dried. Next, 5μL of deionized water dispersion of purified nanoparticles was deposited on a glassy carbon electrode. The blank scan was carried out again to clean the surface of sample-deposited working electrode with the same scanning condition for around 200 cycles. For the electrooxidation of formic acid, the cyclic voltammogram was recorded at a sweep rate of 100 mV/s in N_2-saturated fresh 1 M H_2SO_4 + 1 M formic acid with the potential range from -0.2 V to 1.0 V. The current is normalized by the electrochemically active

surface area (ECSA) of catalysts in the electrode, which was estimated from the integrated reduction charge of surface palladium oxide by assuming a charge of 0.42 mC/cm^2 for the reduction of palladium oxide monolayer. For the CO stripping voltammetry measurements, CO gas was bubbled for 30 minutes through 0.1 M HClO$_4$ solution in which the electrode immersed. The electrode was moved to a fresh N$_2$-saturated 0.1 M HClO$_4$ solution and the CO stripping voltammetry was recorded at a sweep rate of 10 mV/s with the potential range from 0.2 V to 1.2 V.

References

1.   Liu, X.-J.; Cui, C.-H.; Gong, M.; Li, H.-H.; Xue, Y.; Fan, F.-J.; Yu, S.-H., Pt-Ni alloyed nanocrystals with controlled architectures for enhanced methanol oxidation. *Chem. Commun.* **2013,** *49*, 8704-8706.

2.   Qi, Z.; Xiao, C.; Liu, C.; Goh, T. W.; Zhou, L.; Maligal-Ganesh, R.; Pei, Y.; Li, X.; Curtiss, L. A.; Huang, W., Sub-4 nm PtZn Intermetallic Nanoparticles for Enhanced Mass and Specific Activities in Catalytic Electrooxidation Reaction. *J. Am. Chem. Soc.* **2017,** *139* (13), 4762-4768.

3.   Koper, M. T. M., Structure sensitivity and nanoscale effects in electrocatalysis. *Nanoscale* **2011,** *3* (5), 2054-2073.

4.   Brummer, S. B.; Makrides, A. C., Adsorption + Oxidation of Formic Acid on Smooth Platinum Electrodes In Perchloric Acid Solutions. *J. Phys. Chem.* **1964,** *68* (6), 1448-1459.

5.   Kang, Y. J.; Qi, L.; Li, M.; Diaz, R. E.; Su, D.; Adzic, R. R.; Stach, E.; Li, J.; Murray, C. B., Highly Active Pt$_3$Pb and Core-Shell Pt$_3$Pb-Pt Electrocatalysts for Formic Acid Oxidation. *ACS Nano* **2012,** *6* (3), 2818-2825.

6.   Chetty, R.; Scott, K., Characterisation of thermally deposited platinum and palladium catalysts for direct formic acid fuel cells. *J. New Mat. Elect. Syst.* **2007,** *10* (3), 135-142.

7.   Zhang, H.; Jin, M.; Xia, Y., Enhancing the catalytic and electrocatalytic properties of Pt-based catalysts by forming bimetallic nanocrystals with Pd. *Chem. Soc. Rev.* **2012,** *41* (24), 8035-8049.

8.   Stamenkovic, V. R.; Fowler, B.; Mun, B. S.; Wang, G. F.; Ross, P. N.; Lucas, C. A.; Markovic, N. M., Improved oxygen reduction activity on Pt$_3$Ni(111) via increased surface site availability. *Science* **2007,** *315* (5811), 493-497.

9.   Tang, W.; Henkelman, G., Charge redistribution in core-shell nanoparticles to promote oxygen reduction. *J. Chem. Phys.* **2009,** *130*, 194504.

Chapter 5

Conclusion

Tunability remains a double-edged sword in nanocatalysis. The wide variety of structures identified in the past few decades suggests that any given reaction can be matched by an effective nanocatalyst, but this variety also necessitates such an expansive need for fundamental understanding that their rational design remains limited. The picture is further complicated by the difficulty inherent in separating the interwoven structure-property relationships that define catalysis on the nanoscale. Isolating and understanding each is a daunting task, but it remains vital to future efforts to synthesize and supply industrially effective nanocatalysts. In this dissertation, multiple strategies were identified and platforms introduced that offer a chance to disentangle the underlying structures that define the catalytic surface.

Chapter 1 took stock of the current methods for synthesizing intermetallic nanoparticles, outlining the current synthetic techniques and their catalytic application. The defined fundamental understanding served as a scaffold to understand the experimental work outlined in Chapters 2 and 3. In Chapter 2, layered structures of Ni and Pt atop Pd cores served as a platform for studying the fundamentals of metallic mixing on the nanoscale, with detailed TEM analysis combining with theoretical investigation to identify the crucial role of strain in inducing low-temperature mixing that allowed for the formation of alloyed, ordered structures while maintaining overall NP morphology. Chapter 3 presented the synthesis of Au@PdPt core-alloyed shell NPs with thickness variable on the nanometer scale that allowed for the isolation and modulation of strain at the nanoparticle surface.

Chapter 4 applied the nanostructures of the preceding two chapters to small molecule oxidations, allowing for the detailed study of surface structure and its effect on catalytic activity. The activity of Pd-Ni-Pt and Pd-(Ni-Pt)$_2$ for methanol oxidation was found to be dependent on annealing temperature, which is to say on the degree of layer mixing and atomic order formation,

demonstrating that the multilayered core-shell platform is a promising route to shape-controlled, ordered alloy nanocatalysts. For Au@PdPt core-alloyed shell nanoparticles, an intermediate shell thickness was found to be ideal for formic acid oxidation, signifying that the interplay between ligand effects and strain must be considered to efficiently design effective nanocatalysts.

Fundamental understanding of the impact of nanoscale phenomena on catalysis has rapidly expanded over the past 20 years. The explosion of NP variety, however, has outpaced this expansion, with the result that the rational design of nanocatalysts lags behind their implementation. Platforms like those presented here are necessary for the intelligent and efficient tailoring of NP catalysts to realize a future of heterogeneous catalysts that are designed with atomic-level precision and custom-made for industrially important reactions.